Quantum Beam Analysis for Development of Polymer Electrolyte Fuel Cells

WATARU YOSHIMUNE

Doctor of Philosophy

The Graduate University for Advanced Studies, SOKENDAI
March 2024

Preface

This thesis marks the completion of my studies from 2016 to 2023 while I have been a researcher at Toyota Central R&D Labs., Inc. This thesis summarizes the research on the structural analysis of polymer electrolyte fuel cells focusing on the mass transport properties. The quantum beam experiments conducted in this study were measured at Japan Proton Accelerator Research Complex (J-PARC) Center, National Institute of Standards and Technology (NIST) Center for Neutron Research, and SPring-8. I would like to thank the many people involved. This thesis consists of nine chapters. Chapter 1 describes the general introduction to the current status and issues related to the polymer electrolyte fuel cells toward fuel cell electric vehicles, the principles of quantum beam analysis used in this thesis, and the purpose of this research. The challenges in recent years to achieve high fuel cell performance can be divided into two categories: Reduction of the oxygen transport barrier due to the dense ionomer adsorption layer on the platinum surface in the catalyst layer, and structural design of the gas diffusion layer for both oxygen and water transport. Therefore, this thesis is divided into two parts as follows:

Part 1 (Chapters 2–5) describes the ionomer adsorption behavior in catalyst inks and the ionomer interface in ionomer thin films using contrast-variation small-angle neutron scattering (Chapters 2–4) and neutron reflectometry (Chapter 5), respectively. The results show that various factors such as Pt loading (Chapter 2), ionomer content (Chapter 3), temperature (Chapter 4), and carbon surface (Chapter 5) alter the interfacial structure between carbon supported-platinum and ionomers. These findings provide insight into the material design of catalyst layers for polymer electrolyte fuel cells.

Part 2 (Chapters 6–8) presents the pore characterization of the gas diffusion layer by synchrotron radiation X-ray computed tomography with its oxygen transport properties. In Chapter 6, the multiscale pore morphologies of a compressed gas diffusion layers were studied to correlate the oxygen transport properties evaluated by an electrochemical approach. In Chapter 7, the effect of water distribution on the oxygen transport properties in a wet gas diffusion layer was elucidated to clarify the correlation between oxygen and water transport properties. In Chapter 8, inspired by the results of Chapters 6 and 7, I designed a multilayer pore structure of gas diffusion layers with a pore gradient distribution and proposed a new fabrication process for microporous layers to achieve a rational pore morphology within the gas diffusion layer for the mass transport properties.

Finally, Chapter 9 is devoted to a summary and outlook.

October 2023

Wataru Yoshimune

Contents

Contents

Part 2 Structures, Properties, and Formation of Gas Diffusion Layers

Chapter 1

General Introduction

1.1 Background and Motivation

Fuel cells are an electrochemical device that directly converts chemical energy into electrical energy and offers several attractive features, including high energy conversion efficiency, minimal chemical pollution, rapid refueling, compact size, and fast load response. The concept of fuel cells dates back to Humphry Davy's proposal in 1801, and the first fuel cell was invented by Sir William Robert Grove in 1839 [1]. However, practical interest in fuel cells began in 1960s when fuel cells were used for the Gemini and Apollo spacecraft. In 1990, Ballard Power Systems Inc. demonstrated a 5kW fuel stack, showcasing the potential for automotive applications [2]. Toyota Central R&D Labs., Inc. initiated research on polymer electrolyte fuel cells (PEFCs) in 1990. Toyota Motor Corporation launched a project for fuel cell electric vehicles (FCEVs) in 1992 and introduced the first commercial passenger in 2014. Based on the success, a new model for FCEVs was introduced in 2020, achieving a remarkable 50% increase in maximum power density compared to the preceding product [3].

In order to ensure the widespread use of FCEVs, several challenges need to be addressed, including the reduction of costs associated with the fuel cell stack [4]. The ultimate objective of the author's work is to enhance fuel cell performance by achieving low platinum loading. In the development of FCEVs, the focus is on optimizing operating conditions to achieve higher power densities at higher current densities. Under these operating conditions, mass transport properties play a critical role in fuel cell performance [5]. Therefore, understanding the oxygen and water transport properties has become of great importance in the design of fuel cell components. The primary motivation of this thesis is to gain insight into the structure and the associated transport phenomena within these structures. The author has conducted quantum beam analyses (small-angle neutron scattering, neutron reflectometry, and X-ray computed tomography) to investigate the multiscale structures of fuel cell components.

1.2 Polymer Electrolyte Fuel cells

Figure 1.1 shows the working principle of a fuel cell. Fuel is supplied to the anode and air to the cathode, which is common to all types of fuel cells. Fuel cells are classified based on the type of fuel or electrolyte used. Table 1.1 provides a categorization of fuel cell types [6]. The operating temperatures of molten carbonate fuel cells (MCFCs) and solid oxide fuel cells (SOFCs) are too high for vehicles that start and stop frequently. Direct methanol fuel cells (DMFCs) have lower performance than alkaline fuel cells (AFCs) and PEFCs, making them unsuitable for automotive applications. While AFCs provide sufficient power for vehicles, they require measures to prevent carbon dioxide contamination, which adds to the cost of automotive use. Therefore, PEFCs, with lower operating temperatures and higher efficiencies, are suitable fuel cell type for vehicles. Currently, commercially available FCEVs in the market are equipped with PEFC stacks. Phosphoric acid fuel cells (PAFCs) are used for large-scale industrial power generation systems. Recently, PAFCs have gained attention for potential use in heavy-duty trucks [7]. In heavy-duty applications, PAFCs may have higher efficiencies than PEFCs due to their ability to operate at higher temperatures. Since the focus of this thesis is on the development of passenger FCEVs, the author primarily emphasizes the presentation of PEFCs in the following sections.

Table 1.1 Different type of fuel cells.

Fuel cell type (Electrolyte)	Mobile ion	Operating temperature	Applications
Alkaline fuel cell (Alkaline aqueous solution)	OH^-	50 – 200 °C	Space vehicles
Polymer electrolyte fuel cell (proton exchange membrane)	H^+	30 – 100 °C	Passenger vehicles
Direct methanol fuel cell (proton exchange membrane)	H^+	20 – 90 °C	Portable electronic device
Phosphoric acid fuel cell (H_3PO_4 aqueous solution)	H^+	~ 200 °C	Stationary power generation
Molten carbonate fuel cell (Molten carbonate)	CO_3^{2-}	~ 650 °C	Stationary power generation
Solid oxide fuel cell (Solid oxide)	O^{2-}	500 – 1000 °C	Stationary power generation

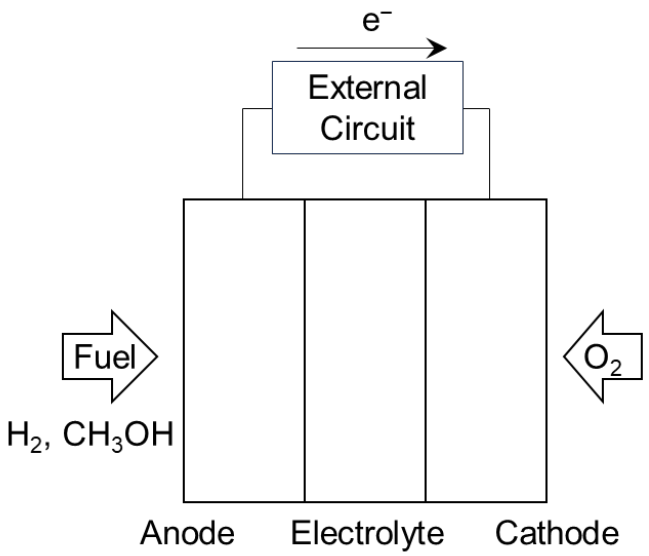

Figure 1.1 Working principle of a fuel cell.

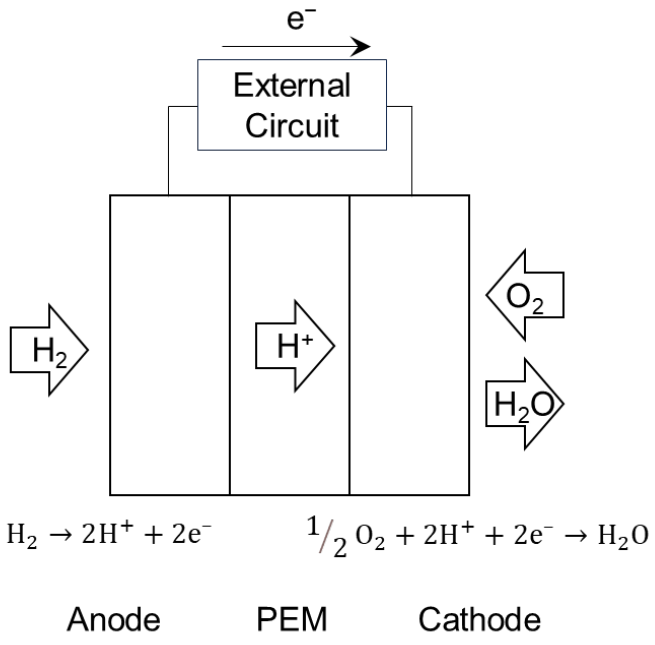

Figure 1.2 Working principle of a PEFC. A proton exchange membrane is abbreviated as PEM.

This thesis focuses on PEFCs, so a PEFC is used as an example to explain the principle of fuel cells [8]. A PEFC has a proton exchange membrane (PEM) to separate cathode and anode (Figure 1.2). On the anode side, the hydrogen oxidation reaction (HOR) takes place, which is described as follows: hydrogen (H_2) passes through the gas diffusion layer (GDL) and reaches the surface of the anode catalyst layer (CL), where it undergoes reduction into protons (H^+) and electrons (e^-). The protons then migrate through the PEM to the cathode side, while the electrons are transported to the cathode side via the external circuit. The HOR reaction has the standard hydrogen electrode (SHE) potential at 1.0 atm and 25 °C and it is expressed as:

$$H_2 \rightarrow 2H^+ + 2e^- . \tag{1.1}$$

On the cathode side, the oxygen reduction reaction (ORR) occurs in the following manner: oxygen (O_2) traverses through the GDL and reach the surface of the cathode CL. Then, oxygen (O_2) reacts with protons (H^+) and electrons (e^-), followed by the production of water (H_2O) and a certain amount of heat. The ORR reaction has the standard electrode potential (E = 1.23 V vs. SHE) at 1.0 atm and 25 °C and it is expressed as:

$$^1/_2\, O_2 + 2H^+ + 2e^- \rightarrow H_2O . \tag{1.2}$$

The overall reaction is described as:

$$H_2 + {}^1/_2\, O_2 \rightarrow H_2O . \tag{1.3}$$

The theoretical reversible cell voltage (E^0) is determined by the difference between the standard potentials of the cathode and anode reactions [8]. In practice, the open circuit voltage (OCV) signifies the voltage when no current is being extracted. According to the Nernst equation, the OCV (E_{OCV}) can be expressed as follows:

$$E_{OCV} = E^0 + \frac{RT}{2F} \ln \frac{P_{H_2}\sqrt{P_{O_2}}}{P_{H_2O}}, \tag{1.4}$$

where R is the gas constant, T is the cell temperature, F is the Faraday constant; and P_{H2}, P_{O2}, and P_{H2O} are the partial pressures of hydrogen, oxygen, and water, respectively. Equation 1.4 indicates that the cell temperature and the partial pressures can affect the OCV. The OCV measured at room temperature is typically about 1.0 V, which is considerably lower than the value calculated from the thermodynamic electrode voltage (1.23 V). This discrepancy can be explained by the current due to the H_2 crossover. The significant drop in the OCV indicates the large crossover current due to the micro-short circuit.

When we extract the current, the cell voltage decreases from the OCV due to different factors. In electrochemistry, the voltage difference between a thermodynamically determined voltage and the experimentally observed voltage is defined as the overpotential. The total overpotential is divided into three factors: activation overpotential, ohmic overpotential, and concentration overpotential. The practical cell voltage (E_{cell}) can be described as follows:

$$E_{\text{cell}} = E_{\text{OCV}} - \eta_{\text{act}} - \eta_{\text{ohm}} - \eta_{\text{con}} . \tag{1.5}$$

Electrochemical reactions cause activation overpotential. The Butler-Volmer (BV) equation represents the activation as follows:

$$i = i_0 \left\{ \exp\left[\frac{\alpha n F \eta_{\text{act}}}{RT}\right] - \exp\left[-\frac{(1-\alpha) n F \eta_{\text{act}}}{RT}\right] \right\}, \tag{1.6}$$

where i_0 is the exchange current density and α is the transfer coefficient, which is influenced by the symmetry of the activation barrier. The BV equation is a fundamental equation in electrochemistry that establishes a connection between the current to the overpotential and provide insight into the voltage drop associated with the electrochemical reactions in PEFCs. The BV equation also indicates that a lower exchange current density results in a greater voltage drop. In PEFCs, the ORR at the cathode is typically slower in comparison to the HOR at the anode. Consequently, the activation loss is usually described only for the ORR. In such cases, Equation 1.6 can be simplified to the Tafel equation, which is expressed as:

$$\eta_{\text{act}} = \frac{RT}{\alpha n F} \ln \frac{i}{i_0} . \tag{1.7}$$

The ohmic overpotential is attributed to the total resistance of the PEM, CLs, GDLs, and flow field, including the contact resistance of each component. The ohmic overpotential is defined as:

$$\eta_{\text{ohm}} = iR . \tag{1.8}$$

Among these components, the protonic resistance of the PEM is the dominant factor contributing to the total resistance. The PEM resistance depends on the water content in the cell. Therefore, the relative humidity (RH) conditions of the reactant gases are one of the key parameters in controlling the ohmic overpotential.

The concentration overpotential primarily arises due to the oxygen concentration gradient that affects the transport of reactants from the flow field plate to the cathode electrode surface. When the diffusion rate is less than the reaction rate, a significant concentration difference occurs between the electrode surface and the interior of the electrode. This difference leads to reactant depletion, often referred to as mass transport limitation. This effect becomes more pronounced at higher current densities because the reactant is consumed more rapidly. The mass transport overpotential can be quantified as follows:

$$\eta_{\text{con}} = \frac{RT}{nF} \ln\left(\frac{i_L - i}{i_L}\right), \tag{1.9}$$

where i and i_{L} are the current and the limited current densities. The value of i can be calculated using Fick's laws of diffusion:

$$i = \frac{nFD(C_{\text{P}} - C_{\text{S}})}{\delta}, \tag{1.10}$$

where D is the diffusion coefficient of oxygen in the electrode, δ is the diffusion length, and C_{P} and C_{S} represent the reactant concentrations near the PEM and at the electrode surface, respectively.

When the reactant is completely consumed at the electrode surface, i_L is expressed as:

$$i_L = \frac{nFDC_P}{\delta}. \tag{1.11}$$

A typical explanation for the concentration overpotential is described as above. In practical use, the oxygen transport process is complicated. Oxygen molecules diffuse from the flow field to the CL surface through the micropores within the GDL. Subsequently, these oxygen molecules move to the catalyst region adjacent to the PEM side by traveling through the nanopores within the CL. As a result, a concentration gradient with varying slopes in the through-plane direction is formed [9]. In addition, oxygen transport resistance arises at the catalyst surface covered with an ionomer layer. This resistance includes oxygen permeation resistance into the ionomer layer and oxygen transport resistance within the dense ionomer layer formed on the catalyst surface [10, 11]. Optimization of each transport process without bottlenecks is necessary to reduce the concentration overpotential.

Figure 1.3 displays a typical polarization curve showing the voltage output for a given current density load for a PEFC. At low current densities (e.g., below 0.1 A cm^{-2}), the activation overpotential is the primary factor contributing to the voltage drop. As the current density increases in the intermediate range, the voltage drop becomes linear due to the ohmic overpotential. As the current density continues to increase, the reactant consumption rate surpasses the supply rate, resulting in the concentration overpotential.

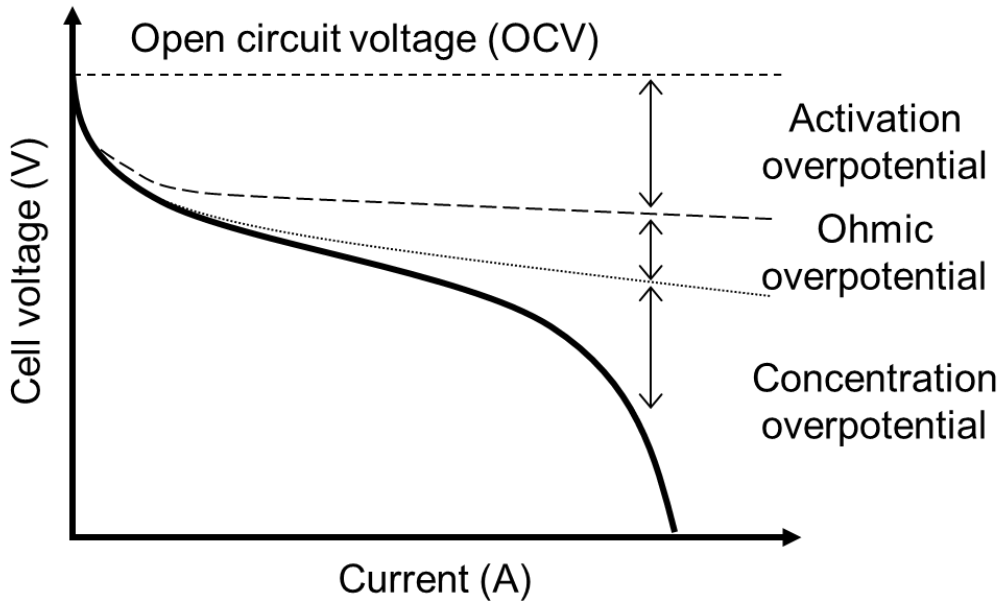

Figure 1.3 Typical polarization curve of a PEFC.

PEFCs consist of laminated structures assembled, as shown in Figure 1.4. Each cell component is briefly introduced in terms of its materials and basic functions.

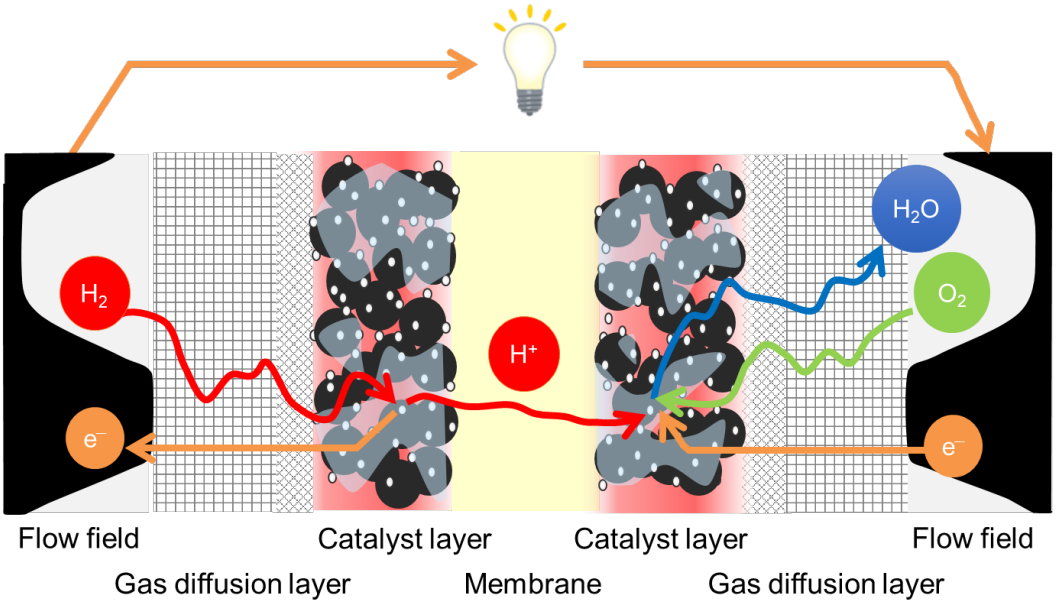

Figure 1.4 Schematic of PEFC structures with reactant pathways.

1) Membrane

The PEM serves as a proton conductor and separator for reactant gases in PEFCs. The most commonly used PEM in PEFCs is Nafion, a perfluorosulfonic acid (PFSA) ionomer. The PFSA membrane has the advantage of proton conductivity and chemical durability. One of the key challenges is to reduce the thickness of PEMs to decrease the ohmic overpotential in PEFCs. The thinner PEM provides higher proton conductivity, resulting in lower ohmic resistance. However, the thin PEMs are compromised in terms of mechanical durability and handling properties during manufacturing. Therefore, efforts are underway to develop reinforced PEMs [12,13].

2) CL

The CL is a crucial component in PEFCs as it facilitates both the anodic and cathodic electrochemical reactions. The CL typically consists of catalyst powder (Pt/C) and PFSA ionomer. The requirements for CLs include good proton conductivity, gas transport property, and water removal capability. Since the electrochemical reaction at the cathode is the rate-determining step in the overall reaction, the development of CLs generally focuses on cathode CLs [14].

3) GDL

The GDL plays multiple roles in mass transfer [5]. Multiscale pores in the GDL provide a route for reactant gases to reach the CL and allow excess water to be removed from the CL. The GDL also facilitates electron pathways between the CL and the flow field. Moreover, the GDL is moderately

compressed and acts as a damping material in the cell assembly. The GDL typically consists of a Janus structure comprising a carbon fiber substrate and a microporous layer (MPL). The substrate is typically treated with polytetrafluoroethylene (PTFE) to increase hydrophobicity for effective water removal.

4) Flow field

The flow field plates supply reactant gases, extract electrical energy, and discharge excess water generated by electrochemical reactions. Straight- or serpentine-type flow fields are commonly used in laboratory studies that typically use 1 cm^2 cells. In practical-sized PEFCs for FCEVs, which have a larger reactive area, the design of the flow field plate becomes critical as it distributes reactant gases and removes excess water. Therefore, the development of flow field plates is one of the most important aspects of FCEVs [3].

1.3. Structural Characterization using Quantum Beam Analysis

1.3.1 Contrast to X-rays and Neutrons in a Sample

X-rays are scattered by the interaction with electrons. The contrast to X-rays in a sample is the electron density defined as the number of electrons per unit volume (ρ_e).

$$\rho_e = \frac{dN_A \sum {n_e}^i}{M}, \tag{1.12}$$

where d is the density of the material, N_A is the Avogadro constant, M is the molecular weight, and $\Sigma {n_e}^i$ is the sum of electrons of all atoms (i) in the material component.

On the other hand, neutrons have no electric charge and are scattered by the inherent interaction with atomic nuclei. The interaction between neutrons and the sample depends on the kind of atom. The scattering length density (SLD) of a material (ρ_s), the contrast to neutrons in a sample, is determined by the scattering length (b^i) associated with each atom [15]:

$$\rho_s = \frac{dN_A \sum b^i}{M}, \tag{1.13}$$

where Σb^i is the sum of the scattering length of all atoms in the material component. The determination of atomic b^i is a non-trivial task, and these values are provided in tabular form [15]. The atomic b^i exhibits unsystematic variations with respect to the atomic number, depending on the nuclear spin direction, and drastic differences can be observed between two isotopes. The main example is between hydrogen and deuterium atoms ($b^H = -0.374\times10^{-12}$ cm and $b^D = 6.67\times10^{-12}$ cm). A negative b^i value indicates a 180° phase shift during scattering, which is a crucial factor for contrast-variation experiments. The principle of the contrast-variation method is to replace an atom with one of its isotopes to induce a significant change in the scattering length.

1.3.2 Small-Angle Scattering

In a small-angle scattering experiment, a scattering event occurs when a quantum beam interacts with a sample. By analyzing the distribution of the scattered beam at different scattering angles, we attempt to characterize the formal structure. Here, we consider the case where X-rays (neutrons) are incident on an isolated particle (Figure 1.5) [16–18]. The particle is uniformly packed with electrons (atomic nuclei) that scatter X-rays (neutrons), and outside the particle is a vacuum. X-rays (neutrons) striking the particle are scattered by each electron (atomic nuclei) in the particle. When the scattering intensity is observed at a certain scattering angle 2θ, this is a superposition of X-rays (neutrons) scattered at various positions in the particle. There is an optical path difference between X-rays (neutrons) passing through two points determined by the position vector $\boldsymbol{r}$, and the phase shift is given by $\boldsymbol{q}\cdot\boldsymbol{r}$, where $\boldsymbol{q}$ is the scattering vector defined as the difference between scattering wave vector $\boldsymbol{k}_s$ and incident wave vector $\boldsymbol{k}_i$. Therefore, the scattering amplitude of the particle $F(\boldsymbol{q})$ can be obtained by superposition of the scattered waves from all the electrons (atomic nuclei) in the particle per volume (V), considering this phase shift with the density $\rho(\boldsymbol{r})$ (electron density ρ_e for X-rays and scattering length density ρ_s for neutrons) as follows:

$$F(\boldsymbol{q}) = \int_V \rho(\boldsymbol{r})\exp(-i\boldsymbol{q}\cdot\boldsymbol{r})d\boldsymbol{r}\,. \tag{1.14}$$

The scattering amplitude varies for the type of particle shapes. The actually observed physical quantity is the scattering intensity $I(q)$. The scattering intensity per unit volume is given by

$$I(\boldsymbol{q}) = \frac{F(\boldsymbol{q})F^*(\boldsymbol{q})}{V}\,. \tag{1.15}$$

The obtained scattering curve $I(\boldsymbol{q})$ versus $\boldsymbol{q}$ that is specific to the size and shape of the particle.

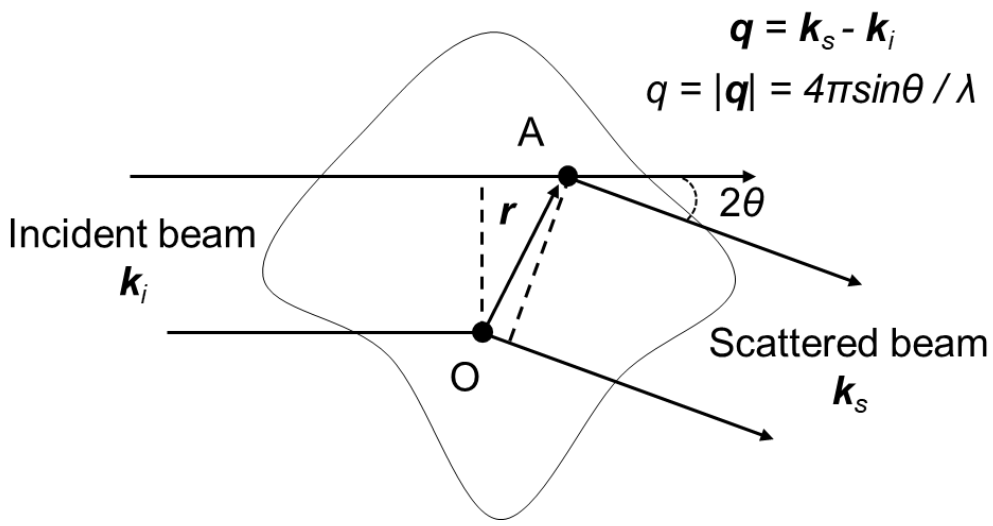

Figure 1.5 Small-angle scattering from a particle.

1.3.3 Reflectometry

The reflection of quantum beams is a useful phenomenon for the investigation of surface structures with buried interfaces. The reflection occurs at interfaces with different refractive indexes n (Figure 1.6). When quantum beams are incident on the specular surface of a thin film, they are divided into two beams. One is the transmitted beam, and the other is the reflected beam. The refractive index n can be expressed using the wavelength λ and density ρ (electron density ρ_e for X-rays and scattering length density ρ_s for neutrons) as follows [17]:

$$n = 1 - \frac{\lambda^2}{2\pi}\rho^2 . \tag{1.16}$$

Reflections of incident beams at equal angles are specular reflections, and the scattering vector q of the reflected beam projected in the z direction, q_z:

$$q_z = \frac{4\pi \sin\theta}{\lambda} . \tag{1.17}$$

According to the Snell law, the following relationship has the interface:

$$n_0 \cos\theta_0 = n_1 \cos\theta_1 . \tag{1.18}$$

If medium 0 is a vacuum and total reflection occurs at the interface between medium 0 and medium 1, then $\theta_1 = 0$ and the critical angle θ_c is written as follows:

$$\cos\theta_c = n_1 . \tag{1.19}$$

When the incident angle is smaller than the critical angle, the total reflection occurs. Beyond the critical angle, a part of the incident neutron beam enters the sample with refraction, and the rest is reflected. In the case, the reflectivity decreases rapidly with q_z. If the interface is perfectly uniform and smooth, the reflectivity decreases in proportion to q_z^{-4}. When a thin film exists on a substrate, there are two interfaces that cause reflection. Therefore, quantum beams reflected at each interface interfere with each other, and the reflectivity shows repeated maxima and minima. The fringe is called the Kissing fringe. The film thickness can be estimated from its position, and the roughness of the air-substrate interface can be estimated from the clarity of the fringe. When we consider a N-laminated structure, the reflectivity can be calculated from the Parratt's equation.

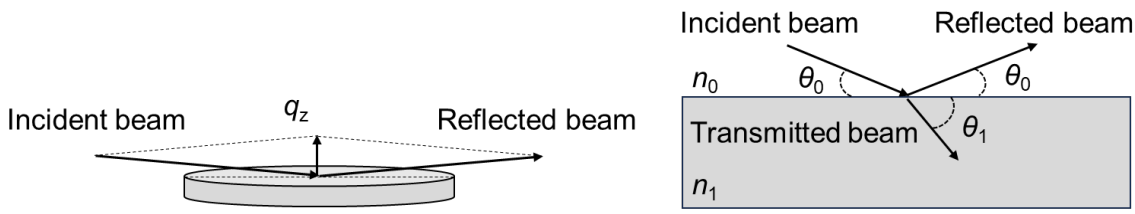

Figure 1.6 Reflection from a flat plate.

1.3.4 Computed Tomography

Quantum beams possess the ability to penetrate materials. Radiography is a technique that acquires images based on differences in their transmission through a sample. By taking projection images while rotating the sample, it is possible to reconstruct a 3D structure of the sample using a method known as computed tomography (CT). As an example, we consider the 2D reconstruction by X-ray absorption contrast method using a collimated X-ray beam (Figure 1.7). The transmitted intensity can be expressed as follows [19]:

$$I_0 = I_i \exp\left\{-\int f(x,y)ds\right\}, \tag{1.20}$$

where $f(x, y)$ is the distribution of X-ray absorption coefficients for a certain section of an object, I_i is the incident intensity of the X-ray beam, and I_0 is the transmitted intensity. Equation 1.20 can be rewritten using the projection data p,

$$\int f(x,y)ds = \ln\frac{I_i}{I_0} \equiv p\,. \tag{1.21}$$

In Figure 1.7, the r-s coordination is rotated by an angle θ from the x-y coordination. The projection data $p(r, \theta)$ is given by

$$p(r,\theta) = \int_{-\infty}^{\infty} f(r\cos\theta - s\sin\theta, r\sin\theta + s\cos\theta)ds\,. \tag{1.22}$$

The relationship between r-s coordination and x-y coordination is as follows:

$$\begin{cases} r = x\cos\theta + y\sin\theta \\ s = -x\sin\theta + y\cos\theta \end{cases}. \tag{1.23}$$

The integral transformation that maps the absorption coefficient distribution $f(x, y)$ to the projection data $p(r, \theta)$ is called the Radon transformation. The projection data $p(r, \theta)$ is imaged over the entire circumference of the object, and $f(x, y)$ is obtained from the image data. In other words, image reconstruction from the projection data is the problem of finding the absorption coefficient $f(x, y)$ by inverse transformation of the Radon transformation.

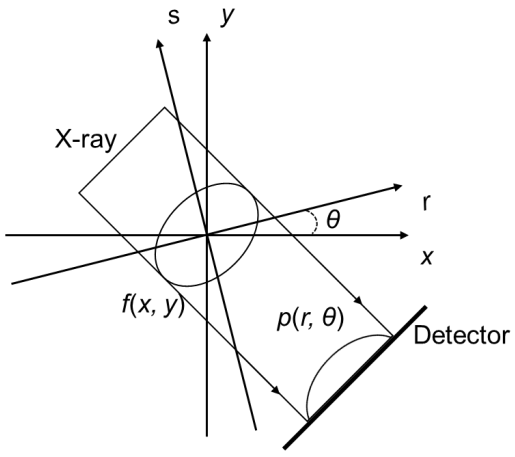

Figure 1.7 Computed tomography using a collimated X-ray beam for a 2D object.

1.4 Objective of This Thesis

One of the issues for FCEVs is the overcome of the mass transport limitations on PEFC performance at high current densities. This two-part thesis attempts to elucidate the fuel cell structure involved in the concentration overpotential:

In Part 1, the author deals with the ionomer interface between platinum and carbon surfaces in CLs. Ionomers with high O_2-permeability are developed to reduce the O_2-transport resistance [20]. The ionomer framework, which consists of a ring-structured backbone with an O_2-permeable glassy amorphous matrix, improves the fuel cell performance thanks to the coarsely packed ionomer layer on the Pt surface [21–23]. Although a clue to a solution in materials has been demonstrated, questions of cost and productivity remain. Therefore, the author focuses on the ionomer/catalyst interface in CLs to find a new solution.

In Part 2, the author focuses on the pore morphologies of GDLs, which are directly related to the oxygen transport resistance. As introduced in Part 1, recent advances in material development have concentrated on the use of ionomers with high oxygen permeability to reduce the local oxygen transport resistance in CLs. The successful development of materials for CLs has results in a higher percentage of oxygen transport resistance in the GDL as a percentage of the total. The oxygen transport resistance in GDLs arises from the curved pore structure and the accumulation of liquid water generated during power generation at the cathode electrode. The author examines GDL pore morphologies using X-ray CT to understand the oxygen transport properties in GDLs from pore morphologies.

References

01. U. Lucia, Overview on Fuel Cells, Renew. Sustain. Energy Rev. 30 (2014) 164–169.
02. K. B. Prater, Solid Polymer Fuel Cell Developments at Ballard, J. Power Sources 37 (1992) 181–188.
03. G. Zhang, Z. Qu, W. Q. Tao, X. Wang, L. Wu, S. Wu, X. Xie, C. Tongsh, W. Huo, Z. Bao, K. Jiao, Y. Wang, Porous Flow Field for Next-Generation Proton Exchange Membrane Fuel Cells: Materials, Characterization, Design, and Challenges, Chem. Rev. 123 (2023) 989–1039.
04. K. Kodama, T. Nagai, A. Kuwaki, R. Jinnouchi, Y. Morimoto, Challenges in Applying Highly Active Pt-Based Nanostructured Catalysts for Oxygen Reduction Reactions to Fuel Cell Vehicles, Nat. Nanotechnol. 16 (2021) 140–147.
05. P. Satjaritanun, S. Shimpalee, I. V. Zenyuk, Gas Diffusion Layers: Experimental and Modeling Approach for Morphological and Transport Properties, Acc. Mater. Res. 3 (2022) 416–425.
06. S. Mekhilef, R. Saidur, A. Safari, Comparative Study of Different Fuel Cell Technologies, Renew. Sustain. Energy Rev. 16 (2012) 981–989.
07. D. A. Cullen, K. C. Neyerlin, R. K. Ahluwalia, R. Mukundan, K. L. More, R. L. Borup, A. Z. Weber, D. J. Myers, A. Kusoglu, New Roads and Challenges for Fuel Cells in Heavy-Duty Transportation, Nat. Energy 6 (2021) 462–474.
08. O. Z. Sharaf, M. F. Orhan, An Overview of Fuel Cell Technology: Fundamentals and Applications, Renew. Sustain. Energy Rev. 32 (2014) 810–853.
09. T. Suzuki, K. Kudo, R. Jinnouchi, Y. Morimoto, Device Simulations in Fuel Cells. In Multiscale Simulations for Electrochemical Devices, Jenny Stanford Publishing, 2020, 303–322.
10. K. Kudo, R. Jinnouchi, Y. Morimoto, Humidity and Temperature Dependences of Oxygen Transport Resistance of Nafion Thin Film on Platinum Electrode, Electrochim. Acta 209 (2016) 682–690.
11. R. Jinnouchi, K. Kudo, N. Kitano, Y. Morimoto, Molecular Dynamics Simulations on O_2 Permeation through Nafion Ionomer on Platinum Surface, Electrochim. Acta 188 (2016) 767–776.
12. T. A. M. Suter, K. Smith, J. Hack, L. Rasha, Z. Rana, G. M. A. Angel, P. R. Shearing, T. S. Miller, D. J. L. Brett, Engineering Catalyst Layers for Next-Generation Polymer Electrolyte Fuel Cells: A Review of Design, Materials, and Methods, Adv. Energy Mater. 11 (2021) 2101025.
13. Mechanical Failure and Mitigation Strategies for the Membrane in a Proton Exchange Membrane Fuel Cell, Renew. Sustain. Energy Rev. 113 (2019) 109289.
14. L. Pan, S. Ott, F. Dionigi, P. Strasser, Current Challenges Related to the Deployment of Shape-Controlled Pt Alloy Oxygen Reduction Reaction Nanocatalysts into Low Pt-Loaded Cathode Layers of Proton Exchange Membrane Fuel Cells, Curr. Opin. Electrochem. 18 (2019) 61–71
15. E. M. Anitas, Small-Angle Scattering (Neutrons, X-rays, Light) from Complex Systems, Springer Briefs in Physics, Springer International Publishing: Cham, Switzerland, 2019.

16. I. Grillo, Small-Angle Neutron Scattering and Applications in Soft Condensed Matter. In Soft Matter Characterization, Springer Netherlands, 2008, 723–782.
17. A. J. Jackson, Introduction to Small-Angle Neutron Scattering and Neutron Reflectometry, NIST Center for Neutron Research, Gaithersburg, MD, 2008.
18. 松岡秀樹, 小角散乱の基礎 ~X 線・中性子の小角散乱から何がわかるか~, 日本結晶学会誌, 41 (1999) 213–216.
19. W. A. Kalender, X-Ray Computed Tomography. Phys. Med. Biol. 51 (2006) R29–R43.
20. T. Yoshizumi, H. Kubo, M. Okumura, Development of High-Performance FC Stack for the New MIRAI (No. 2021-01-0740), SAE Technical Paper Series 2021.
21. A. Rolfi, C. Oldani, L. Merlo, D. Facchi, R. Ruffo, New Perfluorinated Ionomer with Improved Oxygen Permeability for Application in Cathode Polymeric Electrolyte Membrane Fuel Cell, J. Power Sources 396 (2018) 95–101.
22. A. Katzenberg, A. Chowdhury, M. Fang, A. Z. Weber, Y. Okamoto, A. Kusoglu, M. Modestino, Highly Permeable Perfluorinated Sulfonic Acid Ionomers for Improved Electrochemical Devices: Insights into Structure-Property Relationships, J. Am. Chem. Soc. 142 (2020) 3742–3752.
23. R. Jinnouchi, K. Kudo, K. Kodama, N. Kitano, T. Suzuki, S. Minami, K. Shinozaki, N. Hasegawa, A. Shinohara, The Role of Oxygen-Permeable Ionomer for Polymer Electrolyte Fuel Cells, Nat. Commun. 12 (2021) 4956.

Part 1

Structures, Properties, and Formation of Catalyst Layers

Chapter 2

Ionomer Adsorption on Pt/C Surface in Catalyst Inks

2.1 Introduction

A CL for PEFCs is usually prepared by a wet coating process using a catalyst ink. Previous studies [1–4] have reported that the interfacial structure between Pt and ionomers in CLs is influenced by the ionomer distribution of catalyst inks, which affects the electrochemical performance. However, studies of the ionomer adsorption on a Pt surface have been limited to ideal flat interfaces [5], which differ significantly from real systems. In this chapter, the author presents the effect of Pt loading on the ionomer adsorption behavior in an actual catalyst ink using contrast-variation small-angle neutron scattering (CV-SANS).

2.2 Experimental

Pt/C particles, Nafion ionomer (D2020, Chemours), and a mixture of ultrapure water and ethanol were employed to prepare the catalyst ink samples. Commercial catalysts with different Pt loadings (28.4 wt% Pt/C; TEC10E30E, 37.3 wt% Pt/C; TEC10E40E, 46.0 wt% Pt/C; TEC10E50E, Tanaka Kikinzoku Kogyo) were used without any further modifications. The water-to-alcohol weight ratio in the mixture was 7:3, and the volume concentrations of carbon supports and ionomers were $\phi_C = 0.02$ and $\phi_P = 0.015$, respectively. The catalyst inks were prepared by mixing and sonicating the mixtures for 3 minutes. In addition, the author prepared a Nafion dispersion (5 wt%) with a water/alcohol weight ratio of 9:1 as the dispersion media for the contrast-matching method. For SANS measurements, the author conducted experiments at the 10mSANS instrument in the NIST Center for Neutron Research. The incident neutron beam had a wavelength λ of 10 Å, and the scattered neutrons were detected using a two-dimensional detector. Two sample-to-detector distances of 1.2 and 5.2 m were used to cover the momentum transfer range, $q = 4\pi\sin\theta/\lambda$, from 0.004 to 0.3 $Å^{-1}$, where 2θ is the scattering angle. The samples were loaded into a titanium cell with a 1 mm gap between two quartz windows. All measurements were conducted at 25 °C. The scattering data were processed using the direct-beam method to obtain an absolute scale using IGOR Pro macros [6]. Incoherent scattering was subtracted from each data set.

2.3 Analytical Methods

The SLD of Nafion ionomers was determined using the contrast-matching method. The scattering intensity in the dilute ionomer dispersion $I_{\mathrm{ionomer}}(q)$ is written as [7]:

$$I_{\mathrm{ionomer}}(q) = N(\rho_{\mathrm{P}} - \rho_{\mathrm{D}})^2 F(q) S(q), \tag{2.1}$$

where N is the ionomer number density, ρ_{P} is the SLD of ionomers, ρ_{D} is the SLD of dispersion media, $F(q)$ is the form factor, and $S(q)$ is the structure factor. Equation 2.1 indicates that the ρ_{D} with the lowest scattering intensity is the ρ_{S} when experiments are performed for several different ρ_{D}.

In the catalyst ink system consisting of carbon (C), polymer (P), and dispersion media (D), the scattering intensity $I(q)$ can be expressed as [7]:

$$I(q) = a_{\mathrm{CC}} S_{\mathrm{CC}}(q) + 2a_{\mathrm{CP}} S_{\mathrm{CP}}(q) + a_{\mathrm{PP}} S_{\mathrm{PP}}(q)\,, \tag{2.2}$$

where $S_{\mathrm{CC}}(q)$ and $S_{\mathrm{PP}}(q)$ are the self-correlation of each component, and $S_{\mathrm{CP}}(q)$ is the cross-correlation of carbon and polymer. In addition, a_{IJ} is defined as $(\rho_{\mathrm{I}}-\rho_{\mathrm{D}})(\rho_{\mathrm{J}}-\rho_{\mathrm{D}})$ using their SLD (ρ_{C}, ρ_{P}, and ρ_{D}) where I and J are C or P. In this thesis, ρ_{C} is used to be 6.0×10^{10} cm^2, which is the calculated value of the carbon density (2.2 g cm^{-3}). Since the accurate density of Nafion ionomer used in this thesis is unknown, ρ_{P} is evaluated by the contrast-matching method.

For CV-SANS measurements, the author changed the values of ρ_{D} as in the contrast-matching method:

$$\begin{pmatrix} I_1(q) \\ I_2(q) \\ \vdots \\ I_n(q) \end{pmatrix} = \begin{pmatrix} a_{\mathrm{CC}_1} & 2a_{\mathrm{CP}_1} & a_{\mathrm{PP}_1} \\ a_{\mathrm{CC}_2} & 2a_{\mathrm{CP}_2} & a_{\mathrm{PP}_2} \\ \vdots & \vdots & \vdots \\ a_{\mathrm{CC}_n} & 2a_{\mathrm{CP}_n} & a_{\mathrm{PP}_n} \end{pmatrix} \begin{pmatrix} S_{\mathrm{CC}}(q) \\ S_{\mathrm{CP}}(q) \\ S_{\mathrm{PP}}(q) \end{pmatrix}. \tag{2.3}$$

The set of partial scattering functions is evaluated via the singular value decomposition [7]. At least three sets of experiments are required to obtain the partial scattering functions. However, the raw data and the set values of the SLDs contain errors. Therefore, a large number of measurements is required to accurately determine the partial scattering functions.

In Part 1, the author analyzed the structure of catalyst inks assuming a core-shell model proposed by Shibayama et al [8]. In the case of a core-shell model with spherical radius r, the form factor $F(r, q)$ and the structure factor $S(r, q)$ are given by the following equations:

$$F(r,q) = \frac{4\pi r^3}{3} \frac{3\{\sin(qr) - (qr)\cos(qr)\}}{(qr)^3}, \tag{2.4}$$

$$S(r,q) = 1 + \frac{1}{(qr_{ave})^{D_{\mathrm{M}}}} \frac{D_{\mathrm{M}}\Gamma(D_{\mathrm{M}}-1)}{\{1+1/(q^2\xi^2)\}^{(D_{\mathrm{M}}-1)/2}} \sin\{(D_{\mathrm{M}}-1)\tan^{-1}(q\xi)\}. \tag{2.5}$$

Here, r_{ave}, D_{M}, ξ, and $\Gamma(x)$ are the average particle radius, the fractal dimension, the characteristic size of the mass fractal, and the gamma functions of x. In this study, D_{M} and ξ were set to be 1.43 and 1000 Å, respectively, based on the literature value [8]. The actual system for catalyst inks has a wide distribution of particle sizes. The fits presented in this thesis considered the polydispersity of core particles in core-shell spheres. In the fits, the author assumed a Shultz distribution $G(r)$ with a standard

deviation σ for the wide particle size distribution of Pt/C aggregates:

$$G(r) = \frac{r^Z}{\Gamma(Z+1)} \left(\frac{Z+1}{r_{ave}}\right)^{Z+1} \exp\left\{-\frac{r}{r_{ave}}(Z+1)\right\}, \tag{2.6}$$

where Z is the variable defined as $Z = r_{ave}^2\sigma^{-2}$. Three partial scattering functions are rewritten as follows:

$$S_{CC}(q) = NS(q) \int F^2(r,q)\, G(r) \mathrm{d}r\,, \tag{2.7}$$

$$S_{CP}(q) = NS(q) \int [F(r,q)\{(\phi_{shell} - \phi_{out})F(r+\Delta r, q) - \phi_{shell}F(r,q)\}]G(r) \mathrm{d}r\,, \tag{2.8}$$

$$S_{PP}(q) = NS(q) \int \{(\phi_{shell} - \phi_{out})F(r+\Delta r, q) - \phi_{shell}F(r,q)\}^2\, G(r) \mathrm{d}R\,, \tag{2.9}$$

where Δr, ϕ_{shell}, and ϕ_{out} are the thickness of the adsorbed ionomer layer, the volume fraction of the adsorbed ionomer layer, and the average volume fraction outside the core-shell particle.

2.4 Results and Discussion

2.4.1 SLDs of Components in Catalyst Inks

Figure 2.1a shows the SANS profiles of the Nafion dispersion at different SLDs of dispersion media, indicating that the peak intensity at q = 0.04 Å^{-1} is dependent on the SLD of the dispersion media. Figure 2.1b displays the plot of the peak intensities at around q = 0.04 Å^{-1} versus the SLDs of the dispersion media. Equation 2.1 indicates that the scattering intensity of the ionomer dispersion is a quadratic function of SLDs of the dispersion media and the minimum intensity represents the SLD of the ionomers. The SLD at the lowest intensity was 3.3 × 10^{10} cm^{-2}, so that this value was used as the SLD of the ionomers. The SLDs of the Pt/C (TEC10E30E, TEC10E40E, and TEC10E50E) and the dispersion media were calculated from their average compositions and density. The SLDs of the Pt/C with different Pt loadings were within 1% error. A deuterium substitution varies the SLD of the dispersion media, ranging from –0.5 to 5.3 × 10^{10} cm^{-2}. Four sets of samples were prepared by using deuterium-substituted dispersion media to carry out CV-SANS. The SLDs of the different components in the catalyst inks are summarized in Figure 2.2.

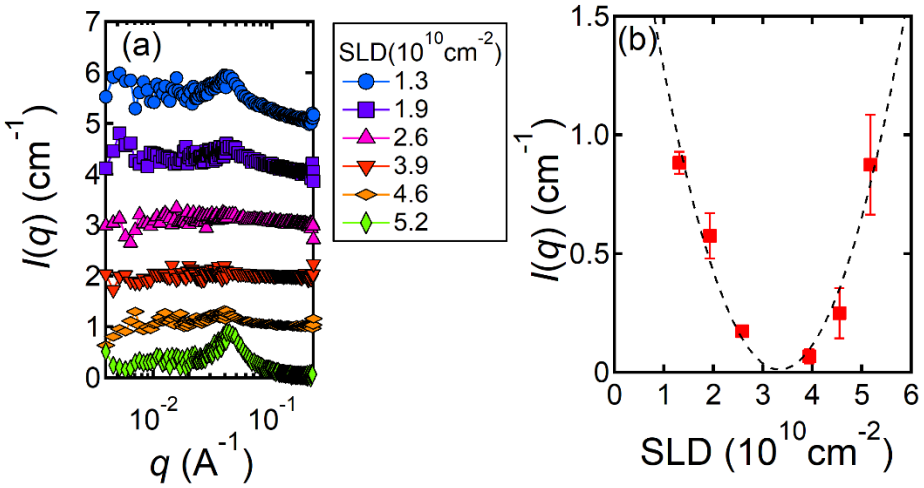

Figure 2.1 (a) SANS profiles of Nafion dispersions. (b) The peak intensities are plotted against SLDs of the dispersion media. The SANS profiles are vertically offset (+1, +2, +3, +4, and +5 for 5.2, 4.6, 3.9, 2.6, 1.9, and 1.3×10^{10} cm^{-2}, respectively) to aid visualization.

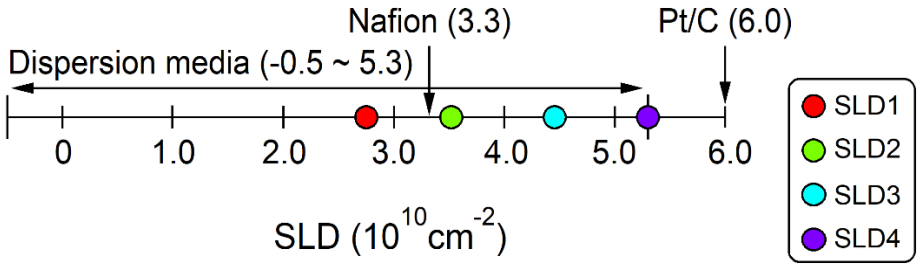

Figure 2.2 SLDs of components in the catalyst ink. Copyright 2019, The Chemical Society of Japan.

2.4.2 SANS Profiles of Catalyst Inks

Figure 2.3 shows SANS profiles of four samples with three different Pt loadings. The intensity in the low-q regions decreases as the SLDs of the dispersion media increase. A singular value decomposition method was applied to obtain partial scattering data from the SANS profiles, resulting in three partial structure factors: $S_{CC}(q)$, $S_{PP}(q)$, and $S_{CP}(q)$. In Figure 2.4, $S_{CC}(q)$ and $S_{PP}(q)$ are plotted on a logarithmic scale and shifted vertically to avoid overlap, while $S_{CP}(q)$ is plotted on a linear scale. The power law slopes of $S_{CC}(q)$ at low q-region represent the surface fractal scattering of the aggregated carbon particles, indicating the fractal nature of particle aggregates [9]. The change in slope at high-q regions is attributed to the hollow structure of the aggregates composed of primary particles [10]. $S_{PP}(q)$ corresponds to the scattering from isolated ionomer micelles in the dispersion media and the ionomer layer adsorbed on the carbon agglomerates [11]. No significant differences were observed between samples in $S_{CC}(q)$ and $S_{PP}(q)$, suggesting similar carbon particle aggregation characteristics. $S_{CP}(q)$, which represents the correlations between Pt/C and ionomer, decreases with increasing Pt loading. It indicates that the shell ionomer layer adsorbed on the Pt/C surface changes the structures with increasing Pt loading. To quantitatively compare this system, the decomposed partial structure factors were fitted with functions based on the core-shell model, as shown by the dashed lines in Figure 2.4. The fitting parameters obtained from the analysis are summarized in Table 2.1. Figure 2.5 shows the volume fraction and thickness of the shell ionomer layer adsorbed on a Pt/C surface with the illustration of the surface in catalyst inks. As the Pt loading increases (i.e., the Pt surface area increases), the volume fraction of the shell ionomer layer decreases while the thickness of the shell ionomer layer increases.

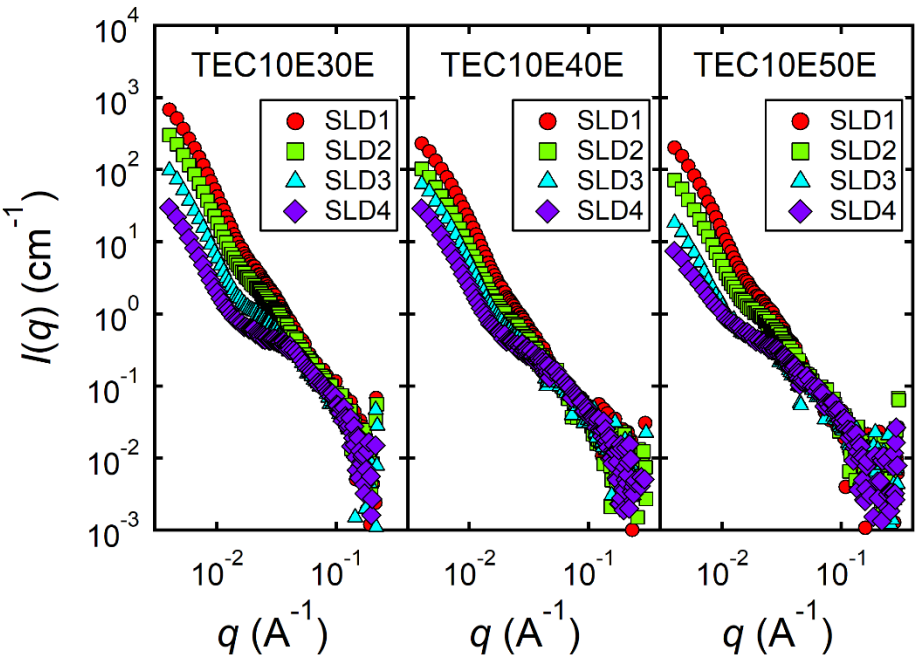

Figure 2.3 SANS profiles of TEC10E30E (left), TEC10E40E (middle), and TEC10E50E (right), respectively. Four data sets with different SLDs of the dispersion media were plotted. Copyright 2019, The Chemical Society of Japan.

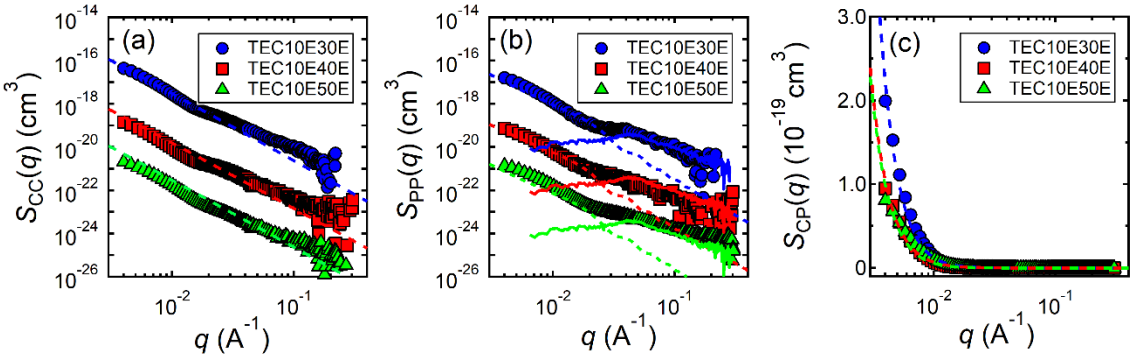

Figure 2.4 Decomposed partial structure factors: (a) $S_{CC}(q)$, (b) $S_{PP}(q)$, and (c) $S_{CP}(q)$. Dashed lines are fit results. Solid lines for $S_{PP}(q)$ are SANS profiles of Nafion dispersion. $S_{CC}(q)$ and $S_{PP}(q)$ sre shifted by multiplying with 100 for TEC10E30E and 0.01 for TEC10E50E to aid the visualization. Copyright 2019, The Chemical Society of Japan.

Table 2.1 Summary of fitting results.

parameters	TEC10E30E	TEC10E40E	TEC10E50E
R (Å)	2075.3 ± 72.5	1783.0 ± 36.8	1758.0 ± 19.7
σ (Å)	5828.8 ± 85.3	7824.1 ± 14.1	7700.1 ± 69.1
ΔR (Å)	111.6 ± 8.5	138.7 ± 6.2	133.0 ± 9.4
ϕ_{shell} (–)	0.442 ± 0.002	0.424 ± 0.014	0.390 ± 0.019

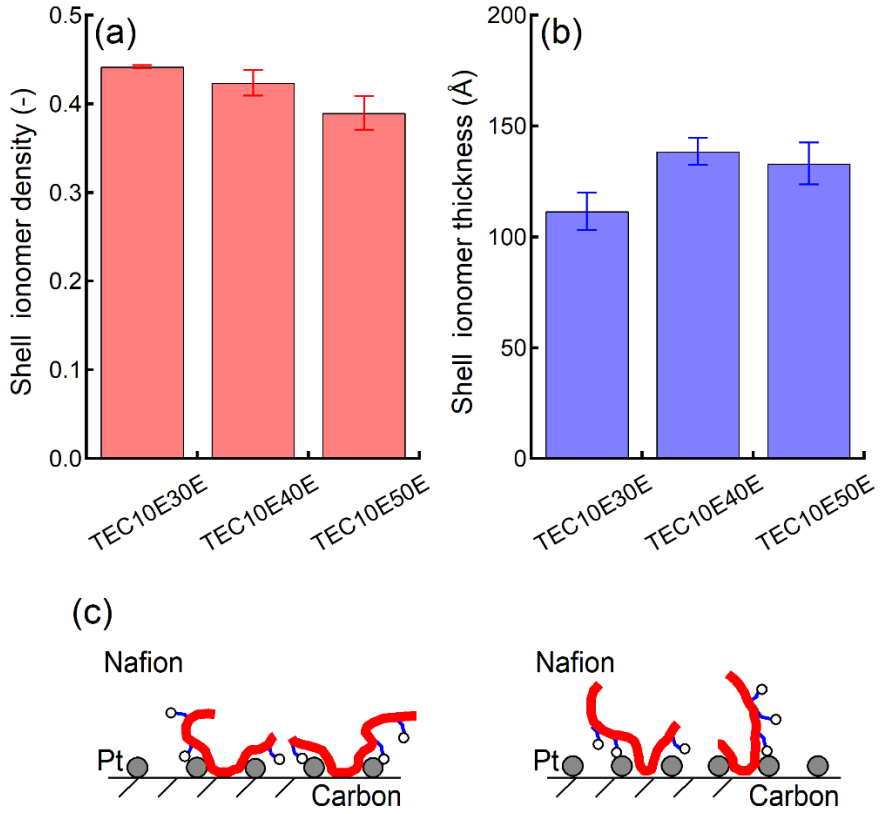

Figure 2.5 The (a) volume fraction and (b) thickness of the shell ionomer layer in catalyst inks, shown as vertical bar charts, and (c) illustration of Nafion molecules adsorbed on a Pt/C particle in the catalyst ink: (left) TEC10E30E and (right) TEC10E50E. Nafion is represented by the backbone (bold red lines), side chains (blue lines), and the terminal sulfonate group (open circles). Copyright 2019, The Chemical Society of Japan.

2.4.3 The Origin of Ionomer Adsorption on the Carbon Surface

In this section, the author interprets the observed interactions between the ionomer and Pt/C surface in a catalyst ink. From the intensity of $S_{CP}(q)$ and the model fitting, the ionomer adsorption was suppressed as the Pt loading increased. The results indicate that the ionomer adsorption is more promoted when the carbon surface is exposed. Mashio et al. used molecular dynamics simulations to demonstrate that ionomer molecules are predominantly adsorbed on a graphite sheet via the perfluoro-carbon backbone, with the hydrophilic side chains pointing away from the graphite sheet [12]. In a previous study, the adsorption equilibrium constants for carbon black without Pt and with 66.3 wt% Pt were determined using ^{19}F nuclear magnetic resonance spectroscopy of a catalyst ink [13]. The previous studies indicated that the hydrophobic interaction is stronger than the interaction between the sulfonate groups and the Pt surface, supporting the current research findings. Here, the author discusses the dependence of the Pt-Pt distance on the ionomer adsorption behavior. In the case of TEC10E30E with a small amount of Pt loading, there is a large Pt-Pt distance, which facilitates the ionomer adsorption on the carbon surface. However, the Pt-Pt distance decreases for TEC10E50E with a larger amount of Pt loading, inhibiting ionomer adsorption. From the amount of Pt loading deposited on the ideal carbon sphere, the average Pt-Pt distances were estimated to be 6.8 nm and 4.6 nm for TEC10E30E and TEC10E50E, respectively. This difference in Pt-Pt distance can significantly affect the adsorption behavior of ionomers with a length of about 30 nm [14]. The increase in Pt loading has a narrower exposed carbon area, leading to a decrease in the volume fraction of the ionomer adsorption layer. However, the increasing area of the Pt surface helps retain the ionomer molecules in the vicinity of the catalyst particle through the side-chain interaction. This interpretation was later verified by other groups using experiments [15] and simulations [16].

2.5 Conclusion

In this chapter, the author employed the CV-SANS technique to investigate the effect of Pt surface area on ionomer adsorption in an actual catalyst ink system. The results revealed that as the Pt loading (i.e., Pt surface area) increased, the ionomer layer at the ionomer/Pt interface became sparser. This observation suggests that the hydrophobic interaction between the ionomer backbone and the carbon surface is stronger than the interaction between the terminal sulfonate groups on the ionomer side chains and the Pt surface. The competition between these attractions was examined for the first time using actual catalyst inks, providing valuable insight into the underlying mechanisms of ionomer adsorption.

References

01. T. T. Ngo, T. L. Yu, H. L. Lin, Influence of the Composition of Isopropyl Alcohol/Water Mixture Solvents in Catalyst Ink Solutions on Proton Exchange Membrane Fuel Cell Performance, J. Power Sources 225 (2013) 293–303.
02. S. Takahashi, T. Mashio, N. Horibe, K. Akizuki, A. Ohma, Analysis of the Microstructure Formation Process and Its Influence on the Performance of Polymer Electrolyte Fuel-Cell Catalyst Layers, ChemElectroChem 2 (2015) 1560–1567.
03. A. Orfanidi, P. J. Rheinländer, N. Schulte, H. A. Gasteiger, Ink Solvent Dependence of the Ionomer Distribution in the Catalyst Layer of a PEMFC, J. Electrochem. Soc. 11 (2018) F1254–F1263.
04. T. V. Van Cleve, S. Khandavalli, A. Chowdhury, S. Medina, S. Pylypenko, M. Wang, K. L. More, N. Kariuki, D. J. Myers, A. Z. Weber, S. A. Mauger, M. Ulsh, K. C. Neyerlin, Dictating Pt-Based Electrocatalyst Performance in Polymer Electrolyte Fuel Cells, from Formulation to Application, ACS Appl. Mater. Interfaces 11 (2019) 46953–46964.
05. M. Harada, K. Kudo, N. L. Yamada, Compositional Segregation in a Cross Section of Wet Nafion Thin Film on a Platinum Surface, Chem. Lett. 48 (2019) 51–54.
06. S.R. Kline, Reduction and Analysis of SANS and USANS Data Using IGOR Pro, J. Appl. Crystallogr. 39 (2006) 895–900.
07. S. Miyazaki, H. Endo, T. Karino, K. Haraguchi, M. Shibayama, Gelation Mechanism of Poly(N-isopropylacrylamide)−Clay Nanocomposite Gels, Macromolecules 40 (2007) 4287–4295.
08. M. Shibayama, T. Matsunaga, T. Kusano, K. Amemiya, N. Kobayashi, T. Yoshida, SANS Studies on Catalyst Ink of Fuel Cell, J. Appl. Polym. Sci. 131 (2014) 39842.
09. G. Ferraro, E. Fratini, R. Rausa, P. Fiaschi, P. Baglioni, Multiscale Characterization of Some Commercial Carbon Blacks and Diesel Engine Soot, Energy Fuels 30 (2016) 9859–9866.
10. J. J. Richards, J. B. Hipp, J. K. Riley, N. J. Wagner, P. D. Butler, Clustering and Percolation in Suspensions of Carbon Black, Langmuir 33 (2017) 12260–12266.
11. M. Shibayama, T. Matsunaga, T. Kusano, K. Amemiya, N. Kobayashi, T. Yoshida, SANS studies on catalyst ink of fuel cell, J. Appl. Polym. Sci. 2014, 131, 39842.
12. T. Mashio, A. Ohma, T. Tokumasu, Molecular Dynamics Study of Ionomer Adsorption at a Carbon Surface in Catalyst Ink, Electrochim. Acta 202 (2016) 14–23.
13. S. Ma, Q. Chen, F. H. Jøgensen, P. C. Stein, E. M. Skou, ^{19}F NMR Studies of Nafion™ Ionomer Adsorption on PEMFC Catalysts and Supporting Carbons, Solid State Ion. 178 (2007) 1568–1575.
14. T. Mima, T. Kinjo, S. Yamakawa, R. Asahi, Study of the Conformation of Polyelectrolyte Aggregates Using Coarse-Grained Molecular Dynamics Simulations, Soft Matter 13 (2017) 5991–5999.
15. S. A. Berlinger, A. Chowdhury, T. V. Cleve, A. He, N. Dagan, K. C. Neyerlin, B. D. McCloskey, C. J. Radke, A. Z. Weber, Impact of Platinum Primary Particle Loading on Fuel Cell Performance: Insights from Catalyst/Ionomer Ink Interactions, ACS Appl. Mater. Interfaces 14 (2022) 36731–36740.

16. Y. Guo, T. Mabuchi, G. Li, T. Tokumasu, Morphology Evolution and Adsorption Behavior of Ionomers from Solution to Pt/C Substrates, Macromolecules 55 (2022) 4245–4255.

Chapter 3

Effect of Ionomer Content on Ionomer Adsorption in Catalyst Inks

3.1 Introduction

A CL in PEFCs exhibits inhomogeneous coverage of ionomer layers with thicknesses of ca. 10 nm and ionomer segregation in certain regions [1]. These agglomerated ionomers in cathode CLs deteriorate gas transport properties and the ORR activity [2–4]. Additionally, nonadsorbed ionomers in catalyst inks are prone to self-aggregation during the drying process, and the segregated ionomers lead to stress concentrations and the formation of cracks in CLs [5]. CV-SANS analysis revealed that catalyst inks with weak interactions between the ionomer and the Pt/C surface induce the formation of cracks in the CL [6]. In this chapter, the author proposes a method to evaluate the nonadsorbed ionomer in catalyst inks using both CV-SANS and a laboratory-based technique. This method allows for assessing nonadsorbed ionomer in catalyst inks and provides insight into the origin of ionomer segregation in CLs.

3.2 Experimental

3.2.1 Sample Preparation

Catalyst inks were prepared using Pt/C particles (TEC10V30E, Tanaka Kikinzoku Kogyo) and Nafion dispersion (D2020, Chemours). These starting materials were dispersed in a water/alcohol mixture as a dispersion medium (DM) and then sonicated for 3 min. The ionomer/carbon weight ratio (I/C) was 0.25, 0.50, 0.75, and 1.00. Tables 3.1 and 3.2 summarize the volume fraction of each component. Changing the I/C also caused the change in the ratio of ethanol to 1-propanol (Table 3.2). However, this difference could be ignored as long as the water/alcohol ratio remained the same. As for the evidence, the differences in the relative dielectric constants [7] and surface tension [8] of water/alcohol mixtures are negligible (Table 3.3). For contrast variation, the SLD (SLD1–4 = 2.0, 3.3, 4.0, and 4.8×10^{10} cm^{-2}) was tuned by varying the H/D ratio using D_2O and C_2D_5OD. Furthermore, we prepared a 2.0 vol% Nafion ionomer dispersion with the same water/alcohol ratio in the dispersion media for the catalyst ink.

Table 3.1 The volume fraction of components in catalyst inks.

I/C	Pt/C (vol%)	Ionomer (vol%)	DM (vol%)
0.25	2.2	0.6	97.2
0.50	2.2	1.3	96.6
0.75	2.2	2.0	95.8
1.00	2.2	2.9	95.0

Table 3.2 The volume fraction of components for the dispersion media.

I/C	Water (vol%)	Ethanol (vol%)	1-Propanol (vol%)
0.25	65	32	3
0.50	65	28	7
0.75	65	25	10
1.00	65	21	14

Table 3.3 Physical properties of water-alcohol mixtures at 20 °C.

DM (vol%)	Dielectric Constant (–)	Surface Tension (mN m^{-1})
Water (100)	80	73
Water/Ethanol (65/35)	66	34
Water/1-Propanol (65/35)	59	27

3.2.2 SANS Measurements

The SANS measurements were conducted using the 10m SANS instrument in the NIST Center for Neutron Research. The wavelength of the incident neutron beam was 10 Å, and the scattered neutrons were collected using a two-dimensional detector. Two sample-to-detector distances of 1.2 and 5.2 m were used to cover a range of momentum transfers from 0.004 to 0.3 $Å^{-1}$. The samples were loaded into a titanium cell with a 1mm gap between the two quartz windows. The SANS experiments were carried out at 25 °C. The scattering data were reduced using IGOR Pro macros to obtain an absolute scale [9]. Incoherent scattering was subtracted from each data set. The obtained scattering functions were decomposed into three partial scattering functions: $S_{CC}(q)$, $S_{PP}(q)$, and $S_{CP}(q)$.

3.2.3 Characterization by Filtration Methods

In the characterization of ionomer-covered Pt/C particles in a catalyst ink, a filtration method was used (Figure 3.1). The particles were removed from the ink using a syringe filter, and the residual solution was transferred into a weighing bottle and subjected to overnight heating at 80 °C. The bottle was weighed before and after the heat treatment. The volume fraction of nonadsorbed ionomer ϕ_{Filter} is calculated by the following equation:

$$\phi_{\mathrm{Filter}} = \frac{nM_{\mathrm{I}}{}^{-1}}{\{(N-n)M_{\mathrm{DM}}{}^{-1} + nM_{\mathrm{I}}{}^{-1}\}}. \tag{3.1}$$

Here, N represents the weight of the residual solution, n denotes the solid content, and M_{I} and M_{DM} are the densities of ionomer (2.0 g cm^{-3}) and DM (0.85 g cm^{-3}), respectively. M_{DM} was calculated based on the composition of the DM.

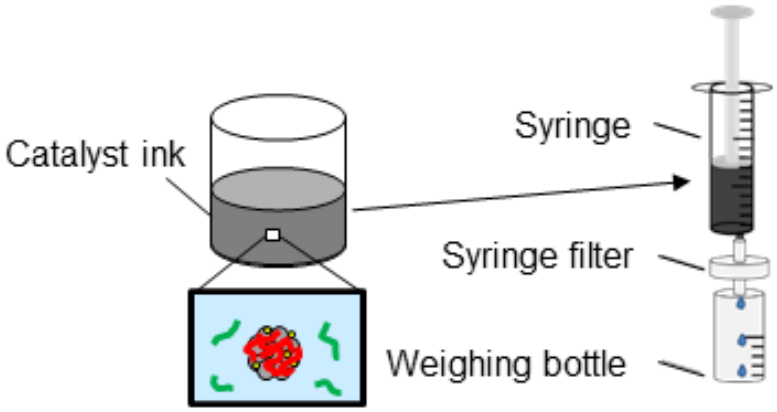

Figure 3.1 Schematic illustration of the filtration method. Copyright 2020, The Chemical Society of Japan.

3.3 Results and Discussion

3.3.1 SANS Profiles of Catalyst Inks

Figure 3.2 shows SANS profiles of each catalyst ink sample at various SLDs (SLD1–4). From these profiles, three partial scattering functions were obtained (Figure 3.3). The scattering intensities of $S_{CC}(q)$ and $S_{CP}(q)$ decrease monotonically, while the profiles of $S_{PP}(q)$ exhibit a peak around q = 0.04 Å^{-1}. In the following paragraph, the author discusses these partial structure functions individually. The $S_{CC}(Q)$ functions for all catalyst inks overlap, indicating that the size of carbon aggregates is independent of the ionomer content (Figure 3.3a). This trend agrees with the previous report based on dynamic light scattering [10]. In contrast, $S_{CP}(q)$ and $S_{PP}(q)$ show sensitivity to I/C (Figure 3.3b,c). The intensities of $S_{CP}(q)$ and $S_{PP}(q)$ in the low q-region (q < 0.03 Å^{-1}) increased from 0.25 I/C to 0.50 I/C and then remain relatively constant up to 1.00 I/C. In order to discuss the volume fraction and thickness of adsorbed ionomer layer, the author applied a core-shell model to fit the three partial scattering functions. As the I/C ratio increases, the volume fraction of the ionomer layer increases from 0.12 at 0.25 I/C to 0.21 at 1.00 I/C, while the thickness remains nearly constant for all I/C ratios. Regarding $S_{PP}(q)$, an upturn is observed in the high q-region (q > 0.03 Å^{-1}) (Figure 3.3b), indicating an increase in nonadsorbed ionomer in the catalyst ink with higher I/C ratios. This observation aligns with the expected limitation of ionomer adsorption on the Pt/C particles. Notably, the $S_{PP}(q)$ exhibits a shoulder near q = 0.04 Å^{-1}, referred to as the "ionomer peak", which is characteristic of ionomers [11–13]. The SANS profile for the 2 vol% ionomer dispersion (Figure 3.4) has a scattering maximum within the same q-range as the catalyst inks. Furthermore, the q-dependence of the ionomer dispersion profile changed from q^{-2} to the q^{-4}. The q^{-2} dependence originates from the fractal dimension of the bending bundle-like aggregates [14], while the crossover point indicates the upper limit of the bundle diameter. In the high q-region above 0.10 Å^{-1}, the q^{-4} dependence can be described by Porod's law, where the scattering intensity depends on the specific surface defined as the total surface area of the interface over the total volume ratio [15]. For bundles, the specific surface equals $2\phi/r$, where ϕ and r represent the volume fraction and the radius of bundles. The scattering intensity in the Porod region depends on the ionomer volume fraction if the radius of ionomer bundles is independent of the volume fraction. SANS experiments have confirmed the validity of the assumption for Nafion ionomer dispersion [16]. Therefore, the volume fraction of nonadsorbed ionomer can be evaluated in the Prodo region as follows:

$$S_{\mathrm{PP}}(q) = \frac{\phi_{\mathrm{out}}}{\phi_{\mathrm{ionomer}}} I_{\mathrm{ionomer}}(q)\,, \tag{3.2}$$

where $I_{\mathrm{ionomer}}(q)$ denotes the scattering function of the ionomer dispersion with a 2 vol% ionomers (ϕ_{ionomer} = 0.020) and ϕ_{out} is the volume fraction of the nonadsorbed ionomer.

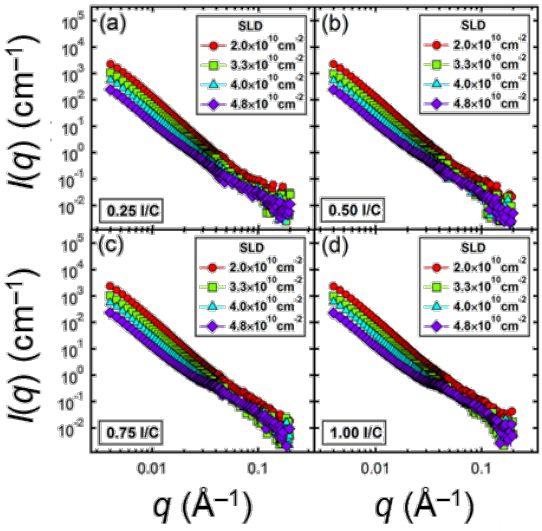

Figure 3.2 SANS profiles of each catalyst ink at various SLDs (SLD1–4). Copyright 2020, The Chemical Society of Japan.

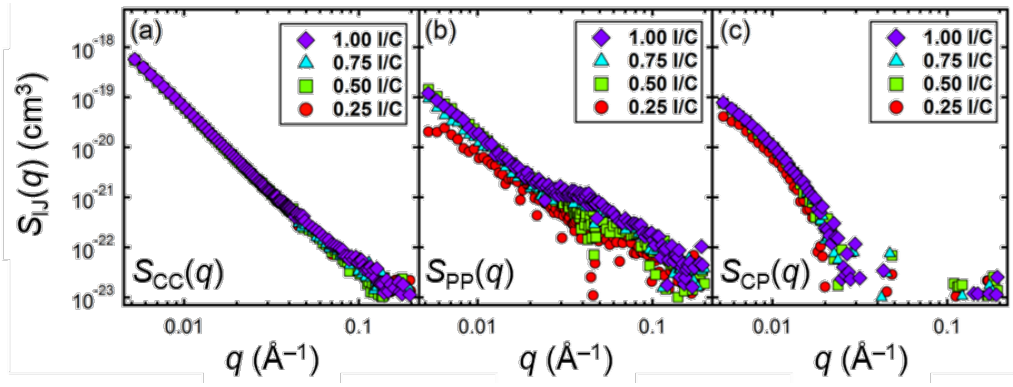

Figure 3.3 Partial structure functions for each catalyst ink. Copyright 2020, The Chemical Society of Japan.

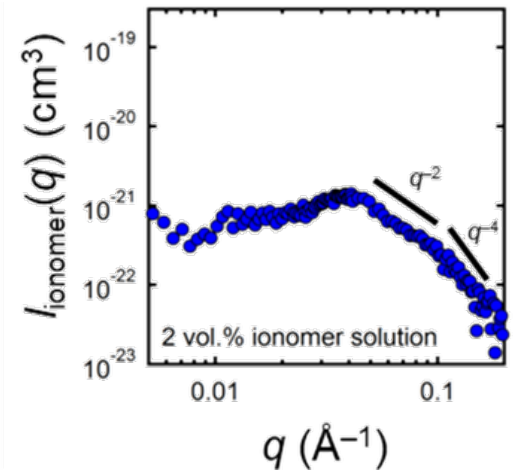

Figure 3.4 SANS profile of a2.0 vol% ionomer dispersion. Copyright 2020, The Chemical Society of Japan.

3.3.2 Mechanism of Ionomer Adsorption in Catalyst Inks

Figure 3.5 provides the volume fraction of nonadsorbed ionomer and the total ionomer volume fraction (ϕ_I). Although ϕ_{out} increased at higher I/C values, ϕ_{out} and ϕ_I were not equal across the I/C range. This deviation indicates the presence of adsorbed ionomer in the catalyst ink. Earlier studies have reported that ionomer adsorption follows the Langmuir isotherm, with a maximum surface coverage of primary adsorption estimated to be 4.62×10^{-4} g m^{-2} in a catalyst ink [17]. By comparing the obtained fitting parameters, the author found that the surface coverage of the catalyst ink at 1.0 I/C is 3.0×10^{-4} g m^{-2}. It suggests that ionomer adsorption in the evaluated range of I/C ratio follows the Langmuir isotherm. Figure 3.6 provides a possible illustration of the catalyst ink based on these findings.

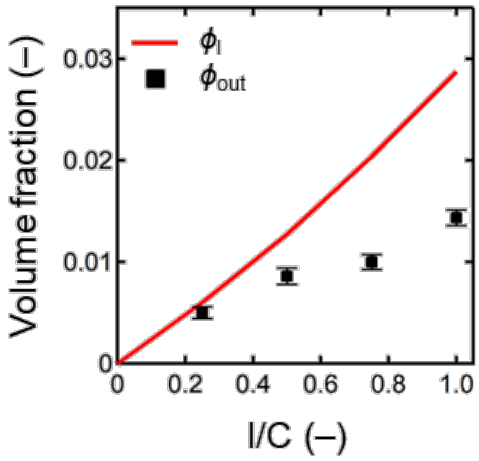

Figure 3.5 Volume fraction of ionomer as a function of I/C ratio in a catalyst ink. ϕ_I and ϕ_{out} are the volume fraction of the total ionomer and nonadsorbed ionomer obtained from CV-SANS measurements. Copyright 2020, The Chemical Society of Japan.

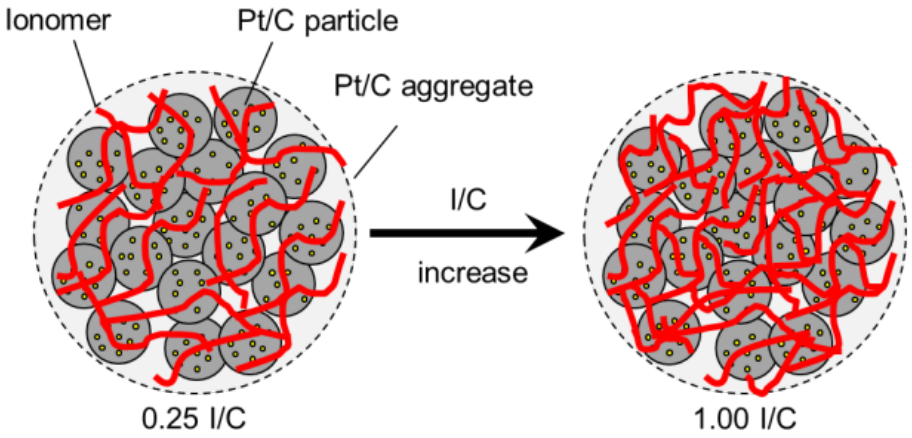

Figure 3.6 Structural evolution of adsorbed ionomer on a Pt/C aggregate in catalyst inks. Copyright 2020, The Chemical Society of Japan.

3.3.3 Comparison between CV-SANS and Filtration Methods

Table 3.4 summarizes the volume fractions of nonadsorbed ionomer obtained through the filtration method, along with ϕ_I and ϕ_{out}. Both ϕ_{Filter} and ϕ_{out} show the same qualitative trend, increasing monotonically with I/C increases. However, the ϕ_{Filter} values are consistently larger than the ϕ_{out} values across the entire range of I/C ratios. The SANS measurements are conducted under stationary conditions, whereas the filtration method involves the application of high shear ($>10^5$ s^{-1}) when passing through the syringe filter. The driving force for ionomer adsorption onto a Pt/C particle is physical adsorption via forces such as van der Waals and hydrophobic interaction [18]. These interactions may be insufficient to maintain the original state of ionomers during the filtration process. Neutron reflectometry studies have observed a sudden desorption of polymer chains adsorbed from a substrate above a certain critical shear rate of approximately 10^4 s^{-1} [19]. Therefore, it is possible that the filtration method may overestimates the amount of nonadsorbed ionomer in catalyst inks.

Table 3.4 The volume fractions of total and nonadsorbed ionomer for each catalyst ink.

I/C	ϕ_I (–)	ϕ_{out} (–)	ϕ_{Filter} (–)
0.25	0.006	0.005	0.004
0.50	0.013	0.007	0.010
0.75	0.020	0.012	0.015
1.00	0.029	0.014	0.022

3.4 Conclusion

In this chapter, the author evaluates the nonadsorbed ionomer in catalyst inks for polymer electrolyte fuel cells (PEFCs). The author employs CV-SANS measurements to quantify the nonadsorbed ionomer. In addition to the CV-SANS method, the author also introduces a laboratory-based technique using the filtration method to assess the volume fraction of nonadsorbed ionomer in catalyst inks. By comparing the results obtained from the filtration method with those from the CV-SANS measurements, the author confirms that the filtration method provides a reliable qualitative trend of nonadsorbed ionomers in catalyst inks. This accessible laboratory method can be used as a practical tool for evaluating nonadsorbed ionomers, enabling researchers to accelerate the rational material design of CLs for PEFCs.

References

01. M. Lopez-Haro, L. Guétaz, T. Printemps, A. Morin, S. Escribano, P. H. Jouneau, P. Bayle-Guillemaud, F. Chandezon, G. Gebel, Three-Dimensional Analysis of Nafion Layers in Fuel Cell electrodes, Nat. Commun. 5 (2014) 5229.
02. S. Takahashi, T. Mashio, N. Horibe, K. Akizuki, A. Ohma, Analysis of the Microstructure Formation Process and Its Influence on the Performance of Polymer Electrolyte Fuel-Cell Catalyst Layers, ChemElectroChem 2 (2015) 1560.
03. T. T. Ngo, T. L. Yu, H.-L. Lin, Influence of the Composition of Isopropyl Alcohol/Water Mixture Solvents in Catalyst Ink Solutions on Proton Exchange Membrane Fuel Cell Performance, J. Power Sources 225 (2013) 293–303.
04. S.-J. Shin, J.-K. Lee, H.-Y. Ha, S.-A. Hong, H.-S. Chun, I.-H. Oh, Effect of the Catalytic Ink Preparation Method on the Performance of Polymer Electrolyte Membrane Fuel Cells, J. Power Sources 106 (2002) 146–152.
05. N. Kumano, K. Kudo, A. Suda, Y. Akimoto, M. Ishii, H. Nakamura, Controlling Cracking Formation in Fuel Cell Catalyst Layers, J. Power Sources 419 (2019) 219–228.
06. T. Kusano, T. Hiroi, K. Amemiya, M. Ando, T. Takahashi, M. Shibayama, Structural Evolution of a Catalyst Ink for Fuel Cells During the Drying Process Investigated by CV-SANS, Polym. J. 47 (2015) 546–555.
07. G. Akerlof, Dielectric Constants of Some Organic Solvent-Water Mixtures at Various Temperatures, J. Am. Chem. Soc. 54 (1932) 4125–4139.
08. G. Vazquez, E. Alvarez, J. M. Navaza, Surface Tension of Alcohol Water + Water from 20 to 50 °C, J. Chem. Eng. Data 40 (1995) 611–614.
09. S. R. Kline, Reduction and Analysis of SANS and USANS Data Using IGOR Pro, J. Appl. Crystallogr. 39 (2006) 895–900.
10. S. Shukla, S. Bhattacharjee, A. Z. Weber, M. Secanell, Experimental and Theoretical Analysis of Ink Dispersion Stability for Polymer Electrolyte Fuel Cell Applications, J. Electrochem. Soc. 164 (2017) F600–F609.
11. A. Kusoglu, A. Z. Weber, New Insights into Perfluorinated Sulfonic-Acid Ionomers, Chem. Rev. 117 (2017) 987–1104.
12. N. Ise, T. Okubo, K. Yamamoto, H. Kawai, T. Hashimoto, M. Fujimura, Y. Hiragi, Ordered Structure in Dilute Solutions of Ionic Biopolymers. 2. Small-Angle X-Ray Scattering Study of Sodium Polyacrylate Solution, J. Am. Chem. Soc. 102 (1980) 7901–7906.
13. C. Welch, A. Labouriau, R. Hjelm, B. Orler, C. Johnston, Y. S. Kim, Nafion in Dilute Solvent Systems: Dispersion or Solution?, ACS Macro Lett. 1 (2012) 1403–1407.
14. T. Mima, T. Kinjo, S. Yamakawa, R. Asahi, Study of the Conformation of Polyelectrolyte Aggregates Using Coarse-Grained Molecular Dynamics Simulations, Soft Matter 13 (2017) 5991–5999.

15. G. Porod, O. Glatter, O. Kratky, Small Angle X-Ray Scattering, ed. by O. Glatter and O. Kratky, Academic Press, London 1982, 17.
16. B. Loppinet, G. Gebel, C. E. Williams, Small-Angle Scattering Study of Perfluorosulfonated Ionomer Solutions, J. Phys. Chem. B 101 (1997) 1884–1892.
17. S. Ma, Q. Chen, F. H. Jøgensen, P. C. Stein, E. M. Skou, ^{19}F NMR Studies of Nafion™ Ionomer Adsorption on PEMFC Catalysts and Supporting Carbons, Solid State Ion. 178 (2007) 1568–1575.
18. J.-H. Lee, U. Paik, J.-Y. Choi, K. K. Kim, S.-M. Yoon, J. Lee, B.-K. Kim, J. M. Kim, M. H. Park, C. W. Yang, K. H. An, Y. H. Lee, Dispersion Stability of Single-Walled Carbon Nanotubes Using Nafion in Bisolvent, J. Phys. Chem. C 111 (2007) 2477–2483.
19. D. L. Anastassopoulos, N. Spiliopoulos, A. A. Vradis, C. Toprakcioglu, S. M. Baker, A. Menelle, Shear-Induced Desorption in Polymer Brushes, Macromolecules 39 (2006) 8901–8904.

Chapter 4

Effect of Temperature on Ionomer Adsorption in Catalyst Inks

4.1 Introduction

A catalyst coated membrane (CCM) for PEFCs was manufactured by transferring the CLs from decal sheets onto both sides of the PEM. The CLs is typically fabricated by wet coating processes [1,2]. The viscosity of catalyst inks can be controlled by optimizing the component materials to achieve shear-thinning behavior in the intermittently coated systems. The rheological properties of catalyst inks are influenced by their nanoscale structures. In catalyst inks, the ionomer spontaneously adsorbs onto the carbon surface [3]. The adsorbed ionomer enhances ink dispersibility and stability by providing repulsive forces between the carbon supports, as explained by the Derjaguin–Landau–Verwey–Overbeek (DLVO) theory [4, 5]. Khandavalli et al. have suggested that the ionomer-to-carbon support mass ratio affects the agglomerated structures and interparticle interactions [6]. Furthermore, it is widely accepted that the structures within catalyst inks influence the microstructures [7–10] and macrostructures [11] of the catalyst layers. Cleve et al. have observed that low-water-content inks result in low ionomer coverage due to weak ionomer-particle interactions [10]. They have correlated this finding with the formation of large ionomer aggregates in the catalyst layers. The ability to control ionomer-particle interactions in a catalyst ink could enable the design of optimal catalyst layers that enhance fuel cell performance.

Temperature plays a significant role in the adsorption of ionomers in catalyst inks. Thoma et al. conducted isothermal titration calorimetry studies and found that ionomer adsorption on a carbon surface is both entropically and enthalpically favored [12]. A positive adsorption entropy ΔS indicates that ionomer adsorption progresses at elevated temperatures. However, the catalyst ink is maintained at low temperatures during ultrasonication process, which is commonly used to crush large carbon agglomerates [13]. Shinozaki et al. demonstrated that using low sonication power and an ice bath is crucial for maximizing catalyst activity [14]. Wang et al. showed that ultrasonication in an ice bath prevents the formation of unfavorable high-temperature environments [15]. Although adsorbing ionomers at elevated temperatures can facilitate the dispersion of carbon supports, the established dispersion process of catalyst inks in an ice bath positively impacts the quality of the CLs. The influence of temperature on catalyst inks is still unclear, and the evolution of the structure with respect to ionomer adsorption needs to be elucidated using CV-SANS. In this chapter, the author reports the temperature dependence of nanostructures in catalyst inks.

4.2 Experimental

4.2.1 Sample Preparation

Ink samples were prepared by mixing carbon supports (Vulcan XC-72R, Cabot) with a Nafion ionomer dispersion (D2020, Chemours) and a water–ethanol mixture. Prior to mixing, the carbon supports were treated with 1 M HNO_3 at 70 °C for 1 h to provide a hydrophilic surface with carboxylic and hydroxyl groups [16]. Since the deposition of platinum nanoparticles renders the catalyst supports hydrophilic [17], the surface properties were modified through nitric acid treatment. The mildly oxidized carbon supports were washed with excess deionized water and then dried in a vacuum furnace. The water–alcohol weight ratio in the dispersion media for the inks was 7:3. The volume fractions of the carbon support ϕ_C and ionomer ϕ_P in the inks were 0.022 and 0.015, corresponding to an I/C ratio of 0.75. After mixing the raw materials, the mixtures were sonicated in an ice bath for 3 min.

4.2.2 SANS Measurements

SANS data were collected using the 10 m SANS instrument in the NIST Center for Neutron Research. The inks were loaded into a titanium cell with a 1 mm gap between the two quartz windows. All SANS measurements were performed at discrete temperatures (T_M) of 25, 40, 55, and 70 °C. The wavelength of the incident neutron beam λ was 10 Å, and the scattered neutrons were gathered using a two-dimensional detector. Two sample-to-detector distances of 1.2 and 5.2 m used for covering the wide range of momentum transfer q (0.004–0.3 $Å^{-1}$; $q = 4\pi\sin\theta/\lambda$, where 2θ is the scattering angle). The scattering data were reduced to obtain an absolute scale using IGOR Pro macros [18]. Additionally, the incoherent scattering originating from the samples was subtracted from each dataset. In this study, a series of SANS measurements were performed for five sample sets with different deuterium contents of the dispersion media (SLD_{DM}): 0.97×10^{10}, 1.94×10^{10}, 3.16×10^{10}, 3.89×10^{10}, and 5.23×10^{10} cm^{-2}. For the decomposition of the SANS scattering functions into partial scattering functions, the SLDs of the carbon and the ionomer was 6.3×10^{10} and 3.3×10^{10} cm^{-2}. To validate the decomposition, the obtained scattering terms were used to reconstruct the SANS scattering functions, which were then compared to the observed SANS functions.

4.3. Results and Discussion

4.3.1. SANS Profiles of Catalyst Inks

Figure 4.1a shows the SANS functions of the catalyst ink at T_M. The intensity of SANS functions at low q monotonically increases as T_M increases. This change indicates a structural evolution of the catalyst ink with temperature. It is important to note that the total scattering functions does not provide insight into the structure of individual components. Figures 4.1b–e display SANS functions for ink samples with a specific SLD_{DM} at each T_M. All SANS functions were used for decomposition. The reconstructed SANS functions (solid lines in Figures 4.1b–e) calculated from the partial scattering functions (Figures 4.2a–c) successfully replicate the observed SANS functions.

The invariance of intensity and slope in $S_{CC}(q)$ across T_M suggests that the carbon aggregate size remains unaffected by temperature changes. Notably, differences in $S_{PP}(q)$ are not observed throughout the entire q range, indicating that liquid–liquid phase separation and a consistent volume fraction of the floating ionomer in the dispersion media. In contrast, a monotonic decrease in $S_{CP}(q)$ intensity is observed with T_M increases, indicating a weak carbon–ionomer interaction with elevated temperatures [19]. Figure 4.2d presents fitting curves that closely match the data. The volume fraction of shell ionomer ϕ_{shell} and thickness ΔR at 25 °C were 0.46 ± 0.01 and 86.4 ± 4.5 Å, respectively, which are consistent in Chapters 2 and 3. All fitting parameters for each T_M are listed in Table 4.1.

Figure 4.3 presents the volume fraction and thickness of the shell ionomer layer in the catalyst ink as a function of T_M. At elevated temperatures, the volume fraction decreased while the shell thickness increased. This trend arises due to the enhanced chain mobility. The CV-SANS analysis revealed that the volume fraction of floating ionomer in the dispersion media was approximately 0.006 at all T_M values. Considering the total ionomer volume fraction of 0.015, the nonadsorbed ionomer fraction was approximately 40%. Importantly, the nonadsorbed ionomer fraction aligns with the volume fraction and thickness of the shell ionomer layer. Although ionomer adsorption is an entropically favored process, the substantial adsorption enthalpy ensures almost complete ionomer adsorption, even at T_M = 25 °C [12].

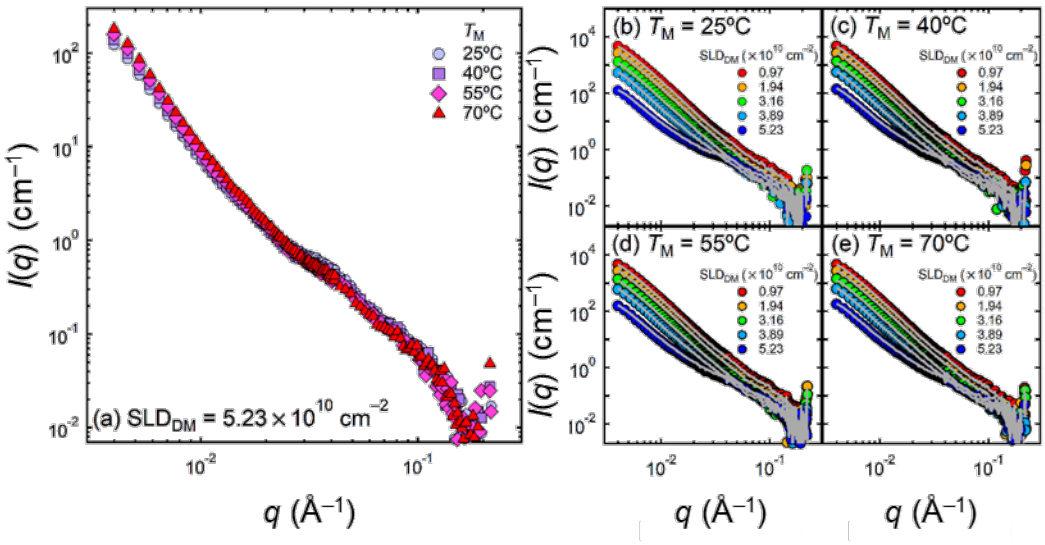

Figure 4.1 (a) SANS functions for catalyst inks at different discrete temperatures T_M (25, 40, 55, and 70 °C). (b–e) Observed (closed circles) and reconstructed (solid lines) SANS functions for catalyst inks at T_M. Copyright 2021, Elsevier.

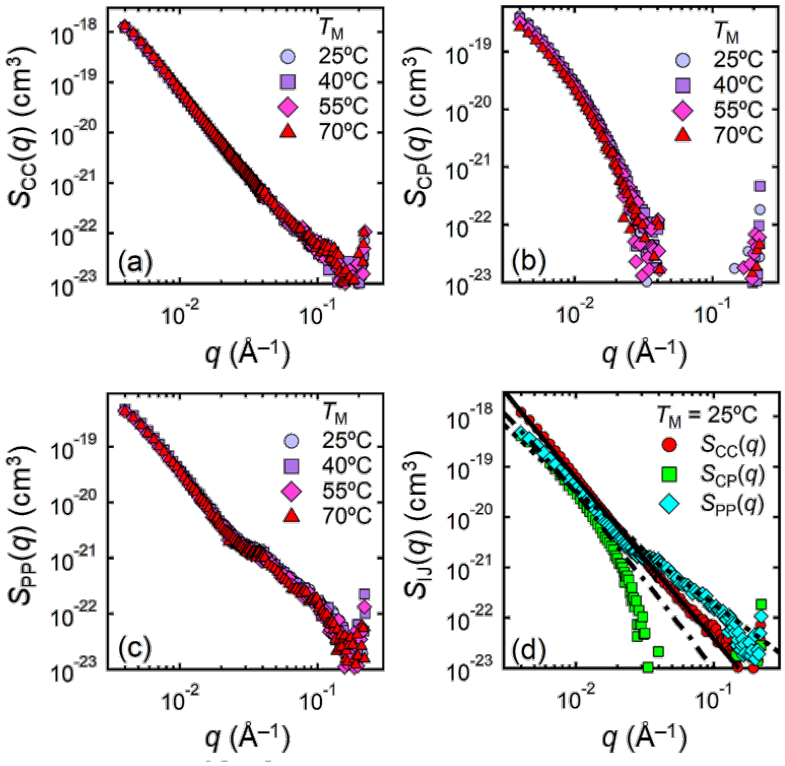

Figure 4.2 Partial scattering functions at T_M (25, 40, 55, and 70 ◦C): (a) $S_{CC}(q)$, (b) $S_{CP}(q)$, and (c) $S_{PP}(q)$. (d) Partial scattering functions at T_M = 25 °C. The solid, dot–dash, and dotted lines represent the fitting results of $S_{CC}(q)$, $S_{CP}(q)$, and $S_{PP}(q)$, respectively. Copyright 2021, Elsevier.

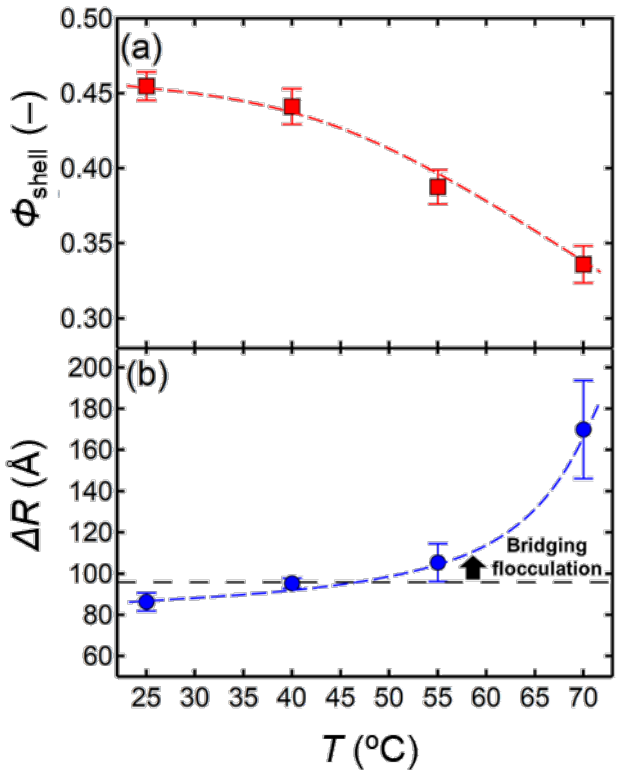

Figure 4.3 Structural evolution of the shell ionomer layer in a catalyst ink as a function of temperature. (a) ϕ_S and (b) ΔR denote the ionomer volume fraction and thickness at the surface of the carbon supports, respectively. The dashed black line in (b) represents the boundary of the appearance of bridging flocculation. Copyright 2021, Elsevier.

Table 4.1 Summary of fitting results.

Parameter	25 °C	40 °C	55 °C	70 °C
R (Å[a])	570.5	570.5	570.5	570.5
σ (Å[b])	523.6 ± 15.7	523.6 ± 15.7	523.6 ± 15.7	523.6 ± 15.7
ΔR (Å)	86.4 ± 4.5	95.3 ± 2.4	105.4 ± 9.1	169.9 ± 23.9
ϕ_{shell} (–)	0.455 ± 0.010	0.441 ± 0.011	0.388 ± 0.012	0.336 ± 0.012
ϕ_{out} (–)	0.006 ± 0.001	0.006 ± 0.001	0.006 ± 0.001	0.006 ± 0.001

a These parameters were fixed using literature values [20]. Parameter *b* was obtained by the fitting results at 25 °C and fixed at 40, 55, and 70 °C.

4.3.2. The Origin of Ionomer Adsorption Behavior

In the case of carbon dispersion without ionomer, the presence of a rigid carbon network structure at elevated temperatures can be explained by the typical DLVO theory, considering van der Waals attraction and electrostatic repulsion. Despite the continued forces of van der Waals attraction remains strong at elevated temperatures, the electrostatic repulsion becomes effective at closer particle distances as temperature increases. In the case of water–ethanol mixtures (w/w = 7/3), the dielectric constant, governing the electrostatic repulsion, decreases from 61.0 to 48.4 with the increase of the temperature from 25 to 70 °C, respectively [21]. Therefore, a rigid carbon network structure in the carbon dispersion is observed at elevated temperatures.

In the presence of the ionomer in catalyst inks, carbon particles covered with the ionomer exhibit a negative zeta potential (~50 mV) [10]. The surface charge is sufficient to prevent the formation of a carbon network structure. The CV-SANS analysis confirms the steady ionomer adsorption state at elevated temperatures. The investigation of ink properties shows a shear-thinning behavior at elevated temperatures (data not shown). In the subsequent discussion, the origin of the shear-thinning behavior in catalyst inks at elevated temperatures is explored, taking into account factors such as electrostatic repulsion, depletion [22,23] and bridging attraction [24,25].

The osmotic effect induced by the non-adsorbed polymer in the dispersion medium, often referred to as depletion flocculation, is unlikely to be responsible for the shear-thinning behavior since the fraction of nonadsorbed ionomer remains constant with temperature. Another form of bridging flocculation occurs when the free end of adsorbed polymer chains physically binds to another particle surface. This type of attraction arises when the particle surfaces have relatively low polymer coverage or when the polymer's coil size is larger than the particles [24]. However, as there is no decrease in the rate of polymer adsorption with increasing temperature, this form of bridging flocculation is not considered to be occurring.

An alternative type of bridging flocculation arises from hydrophobic interactions between the free ends of adsorbed polymer chains. The compression of polymer chains as the polymer-coated particles approaches each other generally leads to a repulsive force known as steric repulsion. Based on a theoretical model [25], the particle thickness and the adsorbed polymer chain thickness determine whether the polymer adsorption results in steric repulsion ($R > 2\Delta R$) or bridging attraction ($R < 2\Delta R$). Using the hard-sphere structure factor [26] with a volume fraction ϕ_C (0.022) and particle radius R (570 Å), the critical transition thickness of particle radius is 192 Å. Thus, the critical transition thickness of the shell ionomer is 96 Å (dotted line in Figure 4.4b). The CV-SANS analysis suggests the occurrence of bridging attraction between 40 and 55 °C. Figure 4.4 provides an illustration of the structural changes observed in the catalyst inks.

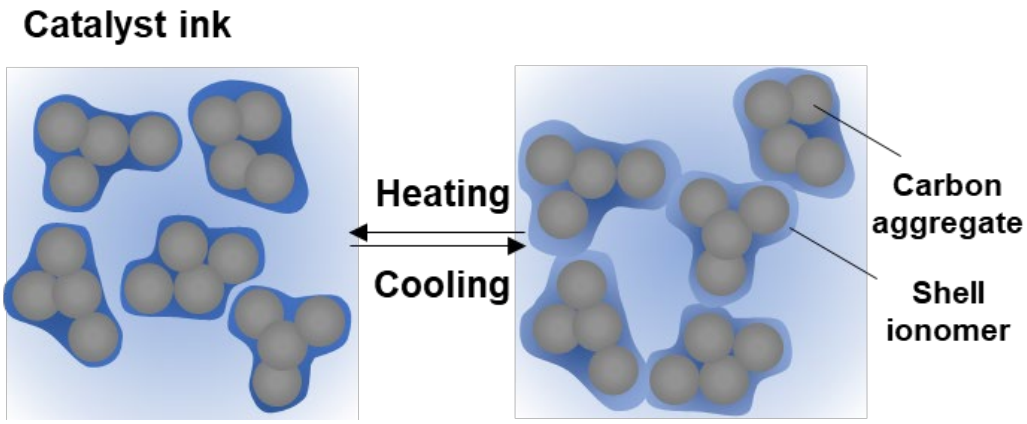

Figure 4.4 Schematic illustration of the structural evolution of a catalyst ink. Copyright 2021, Elsevier.

4.4 Conclusion

In this chapter, the author focused on the structural evolution of catalyst inks with varying temperatures using CV-SANS. The analysis revealed that the thickness of the shell ionomer layer was more than double at 70 °C was more than double that at 25 °C. This increase in thickness resulted in a reduction of electrostatic repulsion and the emergence of bridging attraction between particles. The examination of ink properties shows a shear-thinning behavior at elevated temperatures. These findings highlight that the significance of temperature as a crucial parameter in influencing the viscosities of catalyst inks through the modulation of adsorbed ionomers on carbon supports.

References

01. K. B. Hatzell, M. B. Dixit, S. A. Berlinger, A. Z. Weber, Understanding Inks for Porous-Electrode Formation, J. Mater. Chem. A 5 (2017) 20527–20533.
02. T. Suzuki, Fuel Cell Stack Technology of Toyota, ECS Trans. 75 (2016) 423–434.
03. H. Mizukawa, M. Kawaguchi, Effects of Perfluorosulfonic Acid Adsorption on the Stability of Carbon Black Suspensions, Langmuir 25 (2009) 11984–11991.
04. S. Shukla, S. Bhattacharjee, A. Z. Weber, M. Secanell, Experimental and Theoretical Analysis of Ink Dispersion Stability for Polymer Electrolyte Fuel Cell Applications, J. Electrochem. Soc. 164 (2017) F600–F609.
05. M. B. Dixit, B. A. Harkey, F. Shen, K. B. Hatzell, Catalyst Layer Ink Interactions That Affect Coatability, J. Electrochem. Soc. 165 (2018) F264–F271.
06. S. Khandavalli, J. H. Park, N. N. Kariuki, D. J. Myers, J. J. Stickel, K. Hurst, K. C. Neyerlin, M. Ulsh, S. A. Mauger, Rheological Investigation on the Microstructure of Fuel Cell Catalyst Inks, ACS Appl. Mater. Interfaces 10 (2018) 43610–43622.
07. T. T. Ngo, T. L. Yu, H. L. Lin, Influence of the Composition of Isopropyl Alcohol/Water Mixture Solvents in Catalyst Ink Solutions on Proton Exchange Membrane Fuel Cell Performance, J. Power Sources 225 (2013) 293–303.
08. S. Takahashi, T. Mashio, N. Horibe, K. Akizuki, A. Ohma, Analysis of the Microstructure Formation Process and Its Influence on the Performance of Polymer Electrolyte Fuel-Cell Catalyst Layers, ChemElectroChem 2 (2015) 1560–1567.
09. A. Orfanidi, P. J. Rheinländer, N. Schulte, H. A. Gasteiger, Ink Solvent Dependence of the Ionomer Distribution in the Catalyst Layer of a PEMFC, J. Electrochem. Soc. 11 (2018) F1254–F1263.
10. T. V. Van Cleve, S. Khandavalli, A. Chowdhury, S. Medina, S. Pylypenko, M. Wang, K. L. More, N. Kariuki, D. J. Myers, A. Z. Weber, S. A. Mauger, M. Ulsh, K. C. Neyerlin, Dictating Pt-Based Electrocatalyst Performance in Polymer Electrolyte Fuel Cells, from Formulation to Application, ACS Appl. Mater. Interfaces 11 (2019) 46953–46964.
11. N. Kumano, K. Kudo, A. Suda, Y. Akimoto, M. Ishii, H. Nakamura, Controlling Cracking Formation in Fuel Cell Catalyst Layers, J. Power Sources 419 (2019) 219–228.
12. M. Thoma, W. Lin, E. Hoffmann, M. M. Sattes, D. Segets, C. Damm, W. Peukert, Simple and Reliable Method for Studying the Adsorption Behavior of Aquivion Ionomers on Carbon Black Surfaces, Langmuir 34 (2018) 12324–12334.
13. B. G. Pollet, J. T. E. Goh, The Importance of Ultrasonic Parameters in the Preparation of Fuel Cell Catalyst Inks, Electrochim. Acta 128 (2014) 292–303.
14. K. Shinozaki, J. W. Zack, S. Pylypenko, B. S. Pivovar, S. S. Kocha, Oxygen Reduction Reaction Measurements on Platinum Electrocatalysts Utilizing Rotating Disk Electrode Technique: II. Influence of Ink Formulation, Catalyst Layer Uniformity and Thickness, J. Electrochem. Soc. 162 (2015) F1384–F1396.

15. M. Wang, J. H. Park, S. Kabir, K. C. Neyerlin, N. N. Kariuki, H. Lv, V. R. Stamenkovic, D. J. Myers, M. Ulsh, S. A. Mauger, Impact of Catalyst Ink Dispersing Methodology on Fuel Cell Performance Using in-Situ X-ray Scattering, ACS Appl. Energy Mater. 2 (2019) 6417–6427.
16. A. Orfanidi, P. Madkikar, H. A. El-Sayed, G. S. Harzer, T. Kratky, H. A. Gasteiger, The Key to High Performance Low Pt Loaded Electrodes, J. Electrochem. Soc. 164 (2017) F418–F426.
17. K. Malek, T. Mashio, M. Eikerling, Microstructure of Catalyst Layers in PEM Fuel Cells Redefined: A Computational Approach, Electrocatalysis 2 (2011) 141–157.
18. S. R. Kline, Reduction and Analysis of SANS and USANS Data Using IGOR Pro, J. Appl. Crystallogr. 39 (2006) 895–900.
19. T. Kusano, T. Hiroi, K. Amemiya, M. Ando, T. Takahashi, M. Shibayama, Structural Evolution of a Catalyst Ink for Fuel Cells During the Drying Process Investigated by CV-SANS, Polym. J. 47 (2015) 546–555.
20. G. Akerlof, Dielectric Constants of Some Organic Solvent-Water Mixtures at Various Temperatures, J. Am. Chem. Soc. 54 (1932) 4125–4139.
21. S. Asakura, F. Oosawa, On Interaction between Two Bodies Immersed in a Solution of Macromolecules, J. Chem. Phys. 22 (1954) 1255–1256.
22. M. Shibayama, T. Matsunaga, M. Nagao, Evaluation of Incoherent Scattering Intensity by Transmission and Sample Thickness, J. Appl. Cryst. 42 (2009) 621–628.
23. S. Asakura, F. Oosawa, Interaction between Particles Suspended in Solutions of Macromolecules, J. Polym. Sci. 33 (1958) 183–192.
24. J. Zhang, H. Zeng, Intermolecular and Surface Interactions in Engineering Processes, Eng. 7 (2021) 63–83.
25. V. Runkana, P. Somasundaran, P. C. Kapur, A Population Balance Model for Flocculation of Colloidal Suspensions by Polymer Bridging, Chem. Eng. Sci. 61 (2006) 182–191.
26. J. K. Percus, G. J. Yevick, Analysis of Classical Statistical Mechanics by Means of Collective Coordinates, Phys. Rev. 110 (1958) 1–13.

Chapter 5

Ionomer Adsorption on Carbon Surfaces

5.1 Introduction

In order to meet the demand for more affordable FCEVs, it is crucial to reduce the Pt loading in the CLs while enhancing the Pt mass activity for the ORR. Orfanidi et al. [1] proposed a method involving NH_3 treatment to modify carbon supports. They demonstrated that the modification achieved a uniform ionomer distribution via the Coulombic interaction with the negatively charged ionomer side chains (SO_3^-) and reduced mass transport resistance. Ott et al. [2] introduced balanced quantities of pyridinic/pyrrolic/graphitic nitrogen (N) functional groups on carbon supports, which interacted with ionomer chains and facilitated their homogeneous spatial distribution. Matsutori et al. [3] showed that pyrrolic N functional groups could be selectively and directly introduced to carbon supports using a grafting method initiated by the thermal decomposition of azo compounds. Various electrochemical evaluations of N-modified carbon supports synthesized through different routes have supported the effectiveness of chemically modified carbon supports [1–8]. However, the interfacial structure between N-modified carbon and ionomers has not been experimentally studied, and thus, the effects of this interface remain uncertain. Therefore, this chapter aims to reveal the interfacial ionomer structure on N-modified carbon surfaces and discuss the influence of surface properties.

5.2 Experimental

5.2.1 Sample Preparation

The deposition of approximately 50-nm-thick carbon thin films onto 3-mm-thick Si wafers was carried out using magnetron sputtering. These carbon thin films were fabricated by Kyodo International, Inc. and underwent surface modification using a previously reported method [2]. The carbon films were first treated with concentrated HNO_3 (FUJIFILM Wako Pure Chemical) at 70 °C for 2 h, followed by rinsing with ultrapure water three times to supply carboxylic and hydroxyl groups. The carbon films were subsequently heated in a tube furnace for 2 h with a mixture of NH_3 and Ar gases at flow rates of 0.5 and 0.2 L/min, respectively. To ensure a homogeneous chemical reaction occurred upstream and downstream, the author synthesized $TiO_{2-x}N_x$ from TiO_2 and examined the color distribution. The fabrication procedure and the sample notations are summarized in Figure 5.1a. On the top of the carbon films, approximately 30-nm-thick ionomer thin films were prepared by spin-coating a Nafion ionomer dispersion at 2000 rpm for 30 s [9]. Nafion ionomer dispersion (20 wt %; D2020, Chemours) was diluted to 1 wt % using 1- propanol (FUJIFILM Wako Pure Chemical) and used as the dispersion. The resulting thin films were annealed at 120 °C for 1 h in a vacuum oven.

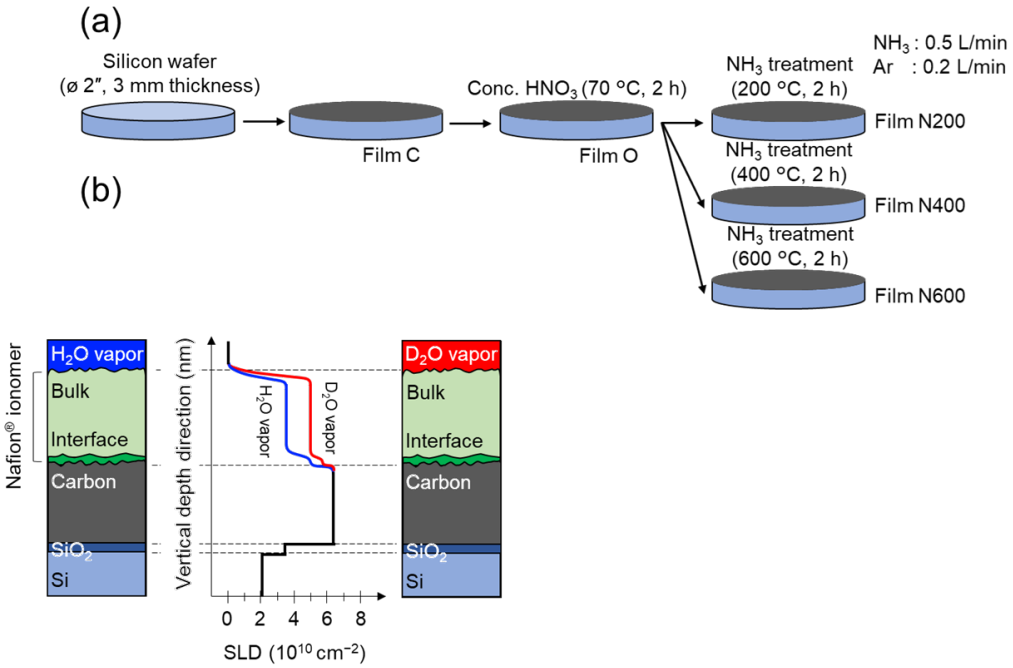

Figure 5.1 (a) Fabrication of surface-modified carbon thin films. (b) Schematic illustration of the vertical scattering length density (SLD) profiles. Copyright 2022, American Chemical Society.

5.2.2 Characterization of Carbon Thin Films

The surface morphologies of the carbon thin films were examined by field emission scanning electron microscope (FE-SEM; Regulus SU8230, Hitachi High Technologies) in secondary electron mode at an accelerated voltage of 2 kV. The surface roughness of the carbon thin films was studied using an atomic force microscope (AFM) (AVH-1000, Bruker) with high-resolution silicon AFM probes (Budget Sensors SHR75) with a spring constant of 3 N/m. For chemical composition analysis, X-ray Photoelectron Spectroscopy (XPS; Quantera SXM, ULVAC PHI) was performed using monochromatic Al Kα X-rays (1486.6 eV). A detector diameter and take-off angle of –200 μm and 45°, respectively, were used. All XPS profiles were charge-corrected based on the C 1s main peak with a binding energy of 284.5 eV. The carbon films were stored in a vacuum desiccator prior to being analyzed by XPS. The XPS analysis was completed within 3 days of sample fabrication. The thickness and density of carbon thin films were determined using an X-ray diffractometer (XRD) with Cu Kα radiation (SmartLab, Rigaku) in the mode of X-ray reflectivity (XRR) measurements. Raman spectra were collected using a laser Raman spectrometer (NRS-3300, Jasco) with 532 nm excitation light. The wettability of carbon thin films was assessed using a contact angle meter (PCA-11, KYOWA).

5.2.3 Characterization of Ionomer Layer on Carbon Surfaces

NR measurements were performed at BL17 SHARAKU in J-PARC Center. Neutron pulses of 25 Hz were generated with a wavelength band of 2.0 Å < λ < 8.8 Å. Reflectometry profiles were obtained at reflection angles of 0.3, 0.7, 1.6, and 3.5°, covering a q-range of 0.007–0.3 Å $^{-1}$. The magnitude of the scattering vector q was defined as $4\pi\sin\theta/\lambda$, where θ is the incident angle. All measurements were performed for approximately 1.5 h to obtain sufficient counting statistics. The collected data were analyzed using the Motofit macro package [10]. NR experiments were conducted with two scattering contrasts on the same system using H_2O and D_2O for double-contrast measurements. The NR measurements were performed at room temperature (22 °C) and under controlled RH conditions. The RH conditions included H_2O vapor, dry N_2 at 4% RH, D_2O vapor, and dry N_2 at 4% RH. A saturated KCl in H_2O/D_2O was added to a homemade aluminum cell to maintain wet conditions (85% RH), while dry conditions were achieved by supplying N_2 gas at a flow rate of 0.1 L/min. The temperature and humidity inside the cells were monitored, and an equilibration time of at least 1 h was used before performing the reflectivity measurements.

The fitting of NR profiles reveals the SLD profile along the vertical direction of thin films. The double-contrast method uses H_2O and D_2O to evaluate the water distribution of thin films. Assuming that the exchange of H_2O and D_2O does not affect the water and material distribution of thin films, the difference in the SLD profiles fitted by NR profiles with H_2O and D_2O exposures is attributed to the water distribution of thin films. In the case of ionomer thin films on carbon surfaces with H_2O and D_2O exposure, the thin film layer consists mainly of ionomer and water, with a few voids and carbon (roughness effects) as follows:

$$\mathrm{SLD}_{\mathrm{film}}^{\mathrm{H_2O}} = \phi_{\mathrm{w}}\mathrm{SLD}_{\mathrm{H_2O}} + \phi_{\mathrm{N}}\mathrm{SLD}_{\mathrm{N}} + \phi_{\mathrm{C}}\mathrm{SLD}_{\mathrm{C}} + \phi_{\mathrm{A}}\mathrm{SLD}_{\mathrm{A}}\,, \tag{5.1}$$

$$\mathrm{SLD}_{\mathrm{film}}^{\mathrm{D_2O}} = \phi_{\mathrm{w}}\mathrm{SLD}_{\mathrm{D_2O}} + \phi_{\mathrm{N}}\mathrm{SLD}_{\mathrm{N}} + \phi_{\mathrm{C}}\mathrm{SLD}_{\mathrm{C}} + \phi_{\mathrm{A}}\mathrm{SLD}_{\mathrm{A}}\,, \tag{5.2}$$

$$\phi_{\mathrm{w}} + \phi_{\mathrm{N}} + \phi_{\mathrm{C}} + \phi_{\mathrm{A}} = 1\,, \tag{5.3}$$

where $\mathrm{SLD}_{\mathrm{film}}^{\mathrm{H_2O}}$, $\mathrm{SLD}_{\mathrm{film}}^{\mathrm{D_2O}}$, $\mathrm{SLD_N}$, $\mathrm{SLD_C}$, and $\mathrm{SLD_A}$ (= 0 $\mathrm{cm^{-2}}$) are the SLDs of a film under H_2O vapor, the thin film under D_2O vapor, the ionomer, the carbon layer, and the air/voids in the film, respectively. Moreover, ϕ_{W}, ϕ_{N}, ϕ_{C}, and ϕ_{A} denote the volume fractions of water, the ionomer, the carbon, and the air/voids, respectively. When performing double-contrast NR measurements, the equation as follows becomes applicable, considering the increase in SLDs of ionomer layers due to the substitution of H_2O with D_2O:

$$\mathrm{SLD}_{\mathrm{film}}^{\mathrm{D_2O}} - \mathrm{SLD}_{\mathrm{film}}^{\mathrm{H_2O}} = \varphi_{\mathrm{w}}(\mathrm{SLD}_{\mathrm{D_2O}} - \mathrm{SLD}_{\mathrm{H_2O}})\,. \tag{5.4}$$

The ϕ_{W} values of the ionomer layers can be definitively determined using the double-contrast method because the subtraction eliminates the two to four terms in Equations 5.1 and 5.2 without any assumptions. However, certain assumptions are necessary to evaluate both $\mathrm{SLD_N}$ and ϕ_{N}. The volume fraction of the ionomer in the films was evaluated based on the following assumptions: (i) considering the volume fraction of carbon in the carbon–ionomer interface that originating from roughness [9,11]; (ii) assuming that the volume fractions of carbon and voids in the ionomer layers are zero; (iii) allowing for frustrations in $\mathrm{SLD_N}$ to satisfy Equations 5.1–3; and (iv) determining the volume fraction of air in the ionomer–air interface to satisfy Equations 5.1–3. Assumption (iii) accounts for the variation in ionomer volume.

The author analyzed the obtained NR profiles with the MOTOFIT analysis package based on the Parratt formula [10]. For this analysis, the four multilayer models (SiO_2, Carbon, interfacial ionomer, and bulk ionomer layers) were assumed to exist on the Si substrate, and all profiles were fitted to minimize χ^2 using the Levenberg–Marquardt algorithm. The intensity of NR decreases with q^{-4}. Hence, any deviations between measured and simulated data at larger values of q are too small and have a minimal impact on the χ^2 value used for fitting. Therefore, the author fitted $I(\mathrm{q})\times q^4$ data to reduce the bias. After the pre-fitting with the genetic algorithm, the global minimum of χ^2 is searched in the nine multidimensional parameter space under the following constraints: 1) the SLD of Si is fixed at 2.07×10^{10} $\mathrm{cm^{-2}}$ [12]; 2) the fixed parameters for the SLD (3.47×10^{10} $\mathrm{cm^{-2}}$) [12], thickness (4 nm), and roughness (1 nm) of the native SiO_2 layer are shared among all NR profiles. The thickness and roughness of the SiO_2 layer were the best-fit parameters for the NR profiles at the carbon thin film. The NR curves of the thin films acquired under H_2O vapor were first analyzed to determine the structural parameters of the carbon and ionomer layers, including their thickness, SLD, and interfacial roughness. For the NR data acquired under D_2O vapor, the fitting process focuses only on determining the SLDs of the ionomer thin films. The remaining parameters obtained from fitting the NR curves collected under H_2O vapor

were used. In the case of the NR data obtained under dry nitrogen gas, the fitting procedure included the determination of the thickness, roughness, and SLD of the ionomer thin films. However, the parameters related to the carbon layers were obtained by fitting the NR curves collected under H_2O vapor.

Earlier reports demonstrated that the multilamellar structure model provides good fitting results for NR data [12]. Therefore, the author tested 11 multilayer models (SiO_2, Carbon, interfacial ionomer, bulk ionomer including six-lamellae structures on the interfacial ionomer, and skin layers at the ionomer/air interface). The fitting results using NR data under H_2O vapor improved to $\chi^2 \approx 6$. However, in the present study, which evaluates the ionomer adsorption layer structure on the carbon surface, the author adopted four multilayer models to focus the discussion on the purpose. Since χ^2 improves as the number of fitting parameters increases, it is necessary to define a figure of merit to quantitatively determine the number of layers in the multilayer models.

5.3 Results and Discussion

5.3.1 Morphological and Chemical Characterization of Carbon Thin Films

Figures 5.2a and 5.2b present SEM images of Films C and N600, respectively, revealing crack-free surfaces. The images show carbon particles with diameters of several nanometers, which are consistent with the primary particle size of carbon black commonly used as a carbon support in catalyst layers [1–8]. Surface AFM images in Figures 5.2c and 5.2d indicate a slight increase in surface roughness from Film C to Film N600, suggesting that the NH_3 treatment caused damage to the carbon surface (as summarized in Table 5.1). Water contact angle measurements (Figure 5.3) demonstrate that Film C exhibited a hydrophobic nature, which transformed into a hydrophilic nature after NH_3 treatments. The chemical compositions of the carbon thin films are summarized in Table 5.2, indicating that they primarily consisted of carbon, oxygen, and nitrogen. The carbon concentration in the thin films ranged from 86% to 89% atomic%. Film O exhibited a higher oxygen concentration compared to Film C, attributed to the surface functionalization induced by the HNO_3 treatment, which introduced carboxylic, hydroxyl, and NO_x groups. Additionally, the oxygen concentration decreased, and the nitrogen concentration increased with increasing NH_3 treatment temperature for Films N200–N600. These results suggest that the NH_3 treatment replaced O functional groups with N functional groups.

Table 5.1 Summary of the analysis parameters in AFM of Film C and Film N600

Sample film	R_a (nm)	R_q (nm)	R_{max} (nm)
C	0.816	0.650	6.29
N600	0.914	0.724	6.84

Table 5.2 XPS-based compositional analysis of surface-modified carbon thin films

Sample film	Composition (atomic%)[a]		
	C 1s	O 1s	N 1s
C	87.8	10.7	1.4
O	86.2	11.9	1.3
N200	88.5	7.6	3.8
N400	88.0	5.1	6.8
N600	86.7	3.3	9.8

[a]The quantitative accuracy is two to three significant digits.

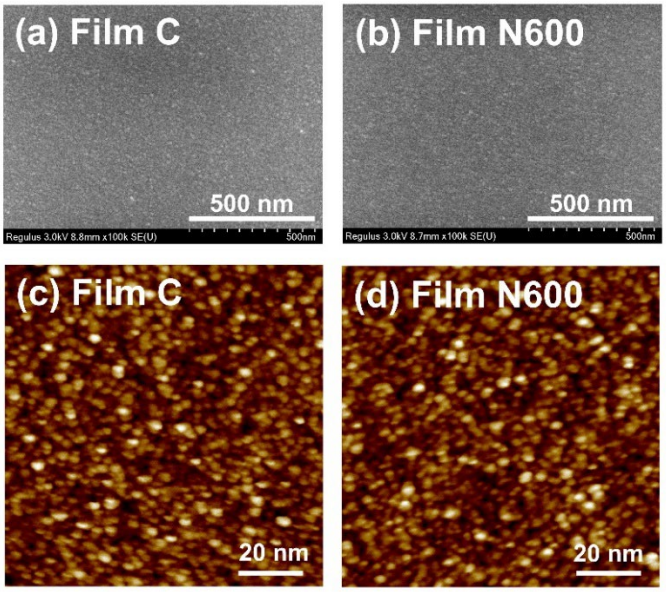

Figure 5.2 (a, b) Surface SEM images captured by the secondary electron mode and (c, d) tapping-mode AFM images of carbon thin films. Copyright 2022, American Chemical Society.

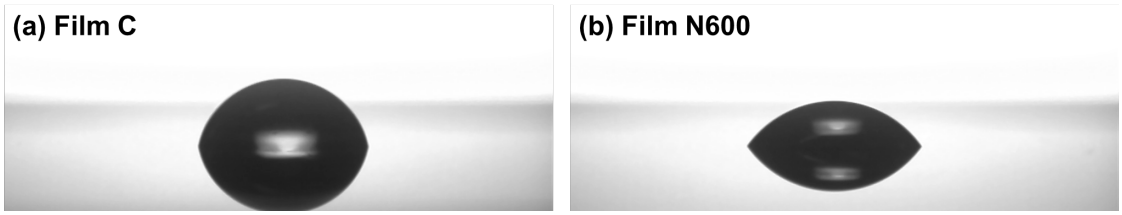

Figure 5.3 Static water contact angle measurements for carbon thin films: (a) Film C and (b) Film N600.

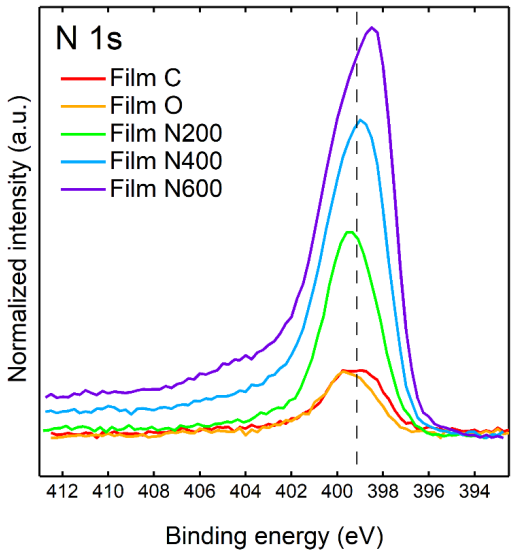

Figure 5.4 N 1s XPS profiles of carbon thin films. The dotted line indicates the peak corresponding to Film C and highlights the peak shifts with increasing NH_3-treatment temperature. Copyright 2022, American Chemical Society.

The N 1s XPS profiles (Figure 5.4) show that as the NH_3 treatment temperature increased, the peak position shifted towards lower binding energies, indicating a change in the composition of the N functional groups. The N 1s XPS profiles were further analyzed to categorize the nitrogen concentration into six N functional groups (Figure 5.6a): graphitic, quaternary, pyrrolic, pyridinic, $–NO_2$, and $–NO_3$, following the study conducted by Ott et al. [2]. The decomposition of the N 1s XPS profiles (Figure 5.5) and the proportion of each N functional group (Figure 5.6b, Table 5.3) demonstrated that at lower NH_3 treatment temperatures, the majority of the N functional groups were pyrrolic, while at higher treatment temperatures, the proportions of pyridinic and quaternary groups increased. These findings align with the results reported by Ott et al. [2].

Raman analysis (Figure 5.7) showed distinct peaks in the spectra originating from the Si wafer at 520 and 960 cm^{-1}, along with a broad peak in the range of 1100–1800 cm^{-1}, attributed to the carbon structure. The G band at 1500 cm^{-1} represents in-plane vibrations in graphene, while the D band at 1300 cm^{-1} indicates disorders in sp^2 carbon clusters induced by the NH_3 treatment above 400 °C. It is important to note that carbon thin films have different physicochemical properties compared to amorphous carbon black commonly used in fuel cells. The D/G ratio, which compares the relative areas of the D and G bands, is a parameter used to estimate the degree of lattice defects in graphene-like planes. The D/G ratios of Films C, O, N200, N400, and N600 were 0.42 ± 0.01, 0.41 ± 0.01, 0.37 ± 0.01, 0.28 ± 0.01, and 0.28 ± 0.01, respectively. The significant decrease in the D/G ratio indicated that NH_3 treatment at elevated temperatures (>400 °C) introduced several tens of percent of defects in the framework of a graphene-like plane.

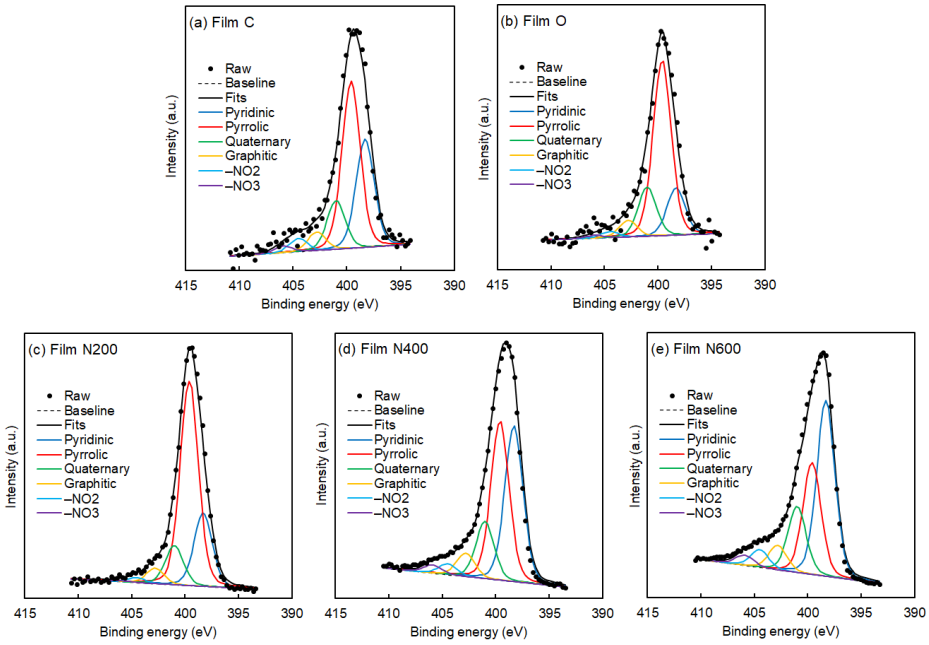

Figure 5.5 N 1s XPS profiles of carbon thin films. The spectra were deconvoluted with respect to six different N species, which are illustrated in Figure 5.6a. Table 5.3 lists the binding energies of all these species.

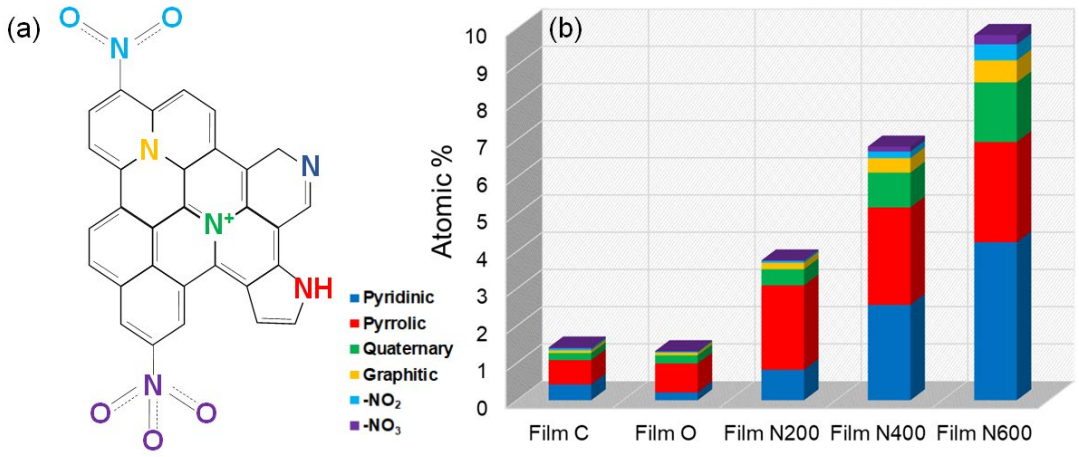

Figure 5.6 (a) Illustration of various N functional groups in a graphene-like plane. (b) Proportions of N functional groups in carbon thin films; the colors correspond to those in Figure 5.6a. Copyright 2022, American Chemical Society.

Table 5.3 Binding energies of N species for deconvoluting N 1s XPS profiles

N species	Pyridinic	Pyrrolic	Quaternary	Graphitic	$–NO_2$	$–NO_3$
Binding energy (eV)	398.3	399.6	401.0	402.8	404.5	405.9

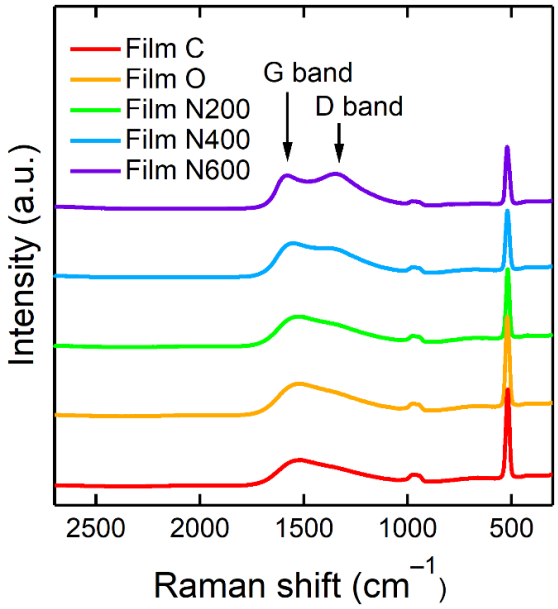

Figure 5.7 Raman spectra of the carbon thin films. The high-wavelength broad peak originates from the Si wafer and carbon thin film, respectively. Copyright 2022, American Chemical Society.

5.3.2 Interfacial Distribution of Ionomer Thin Films on Carbon Surface

Figure 5.8 displays NR curves of the Nafion ionomer thin films obtained at 85% RH. The observed fringes in the NR curves arise from the interference of reflections at the interfaces within the thin films. The shape of the fringes at q = 0.055 Å^{-1} exhibited variations among Films C, O, and N200–N600, indicating changes in the interfacial structures related to the ionomer on the N-modified carbon surfaces. To quantitatively analyze the data, the experimental NR curves were fitted using a structural model described in Figure 5.1b with the least-square method. First, the NR curves of the thin films obtained under H_2O vapor were analyzed to determine the structural parameters of the carbon and Nafion ionomer layers, including thickness, SLD, and interfacial roughness. Subsequently, the NR curves collected under D_2O vapor were fitted using the parameters determined from the H_2O vapor fits, focusing solely on the SLDs of the ionomer thin films.

In accordance with existing literature [9, 11–19], an "interfacial layer" (Figure 5.1b) was introduced on the carbon side of the bulk Nafion ionomer layer. Initially, a water-rich layer on the carbon surface was considered based on previous reports on SiO_2–Nafion and Pt–Nafion interfaces [12, 13, 15–19]. However, this assumption failed to reproduce the NR curves satisfactorily. Therefore, a highly dense Nafion ionomer layer [9, 11] was considered, leading to an improved goodness of fit (Table 5.4).

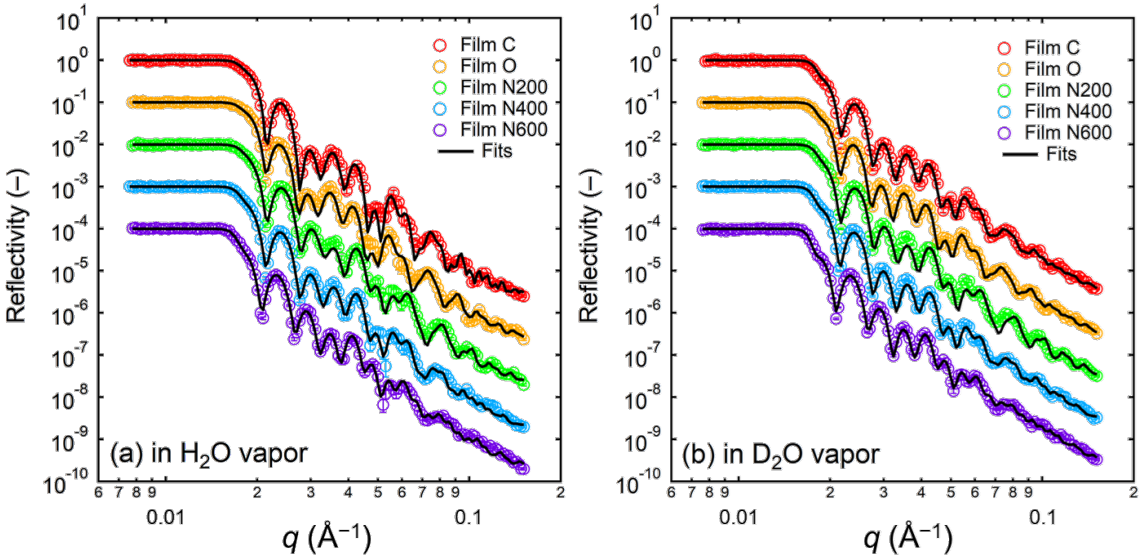

Figure 5.8 Experimental NR data and the corresponding fits (solid lines) of Nafion ionomer thin films obtained under (a) H_2O and (b) D_2O vapors. The NR curves have been vertically offset ($\times10^{-1}$, $\times10^{-2}$, $\times10^{-3}$, and $\times10^{-4}$ for Films O, N200, N400, and N600, respectively) to aid visualization. Copyright 2022, American Chemical Society.

Table 5.4 Summary of fitting parameters.

Film	Condition	Carbon layer		roughness (nm)	Interfacial layer		roughness (nm)	Bulk layer		roughness (nm)	χ^2
		SLD ($\times10^{-4}$nm^{-2})	Thickness (nm)		SLD ($\times10^{10}$cm^{-2})	Thickness (nm)		SLD ($\times10^{10}$cm^{-2})	Thickness (nm)		
C	In H_2O vapor	6.36±0.05	53.3±0.5	1.0±0.3	4.51±0.02	2.8±0.2	0.6±0.1	3.78±0.02	31.3±0.2	1.2±0.1	14.6
	In dry gas	6.36	53.3	1.0	4.33±0.02	2.9±0.1	0.4±0.2	3.62±0.02	28.3±0.2	0.4±0.1	24.8
	In D_2O vapor	6.36	53.3	1.0	5.07±0.01	2.8	0.6	4.34±0.01	31.3	1.2	21.0
O	In H_2O vapor	6.36±0.04	54.2±0.5	0.9±0.3	4.50±0.01	2.8±0.2	0.4±0.2	3.77±0.01	32.4±0.2	1.1±0.1	10.2
	In dry gas	6.36	54.2	0.9	4.49±0.02	2.9±0.1	0.4±0.2	3.62±0.01	29.5±0.2	0.4±0.1	15.2
	In D_2O vapor	6.36	54.2	0.9	5.03±0.01	2.8	0.4	4.36±0.01	32.4	1.1	12.3
N200	In H_2O vapor	6.37±0.01	54.5±0.5	0.9±0.3	4.42±0.01	2.8±0.2	0.5±0.1	3.67±0.01	29.1±0.3	1.2±0.1	8.5
	In dry gas	6.37	54.5	0.8	5.09±0.02	3±2	0.5±0.2	3.37±0.01	26±2	0.3±0.1	15.7
	In D_2O vapor	6.37	54.5	0.8	4.43±0.01	2.8	0.5	4.09±0.01	29.1	1.2	12.9
N400	In H_2O vapor	6.08±0.01	53.0±0.5	1.3±0.3	4.55±0.01	3.1±0.2	0.7±0.1	3.79±0.02	30.1±0.3	1.1±0.1	8.5
	In dry gas	6.08	53.0	1.3	4.08±0.01	2.2±0.5	0.4±0.1	3.65±0.01	28.3±0.3	0.4±0.2	21.2
	In D_2O vapor	6.08	53.0	1.3	4.61±0.01	3.1	0.7	4.16±0.01	30.1	1.1	15.1
N600	In H_2O vapor	5.68±0.05	55.4±0.5	1.4±0.4	4.56±0.01	3.4±0.3	0.6±0.1	3.73±0.01	30.0±0.3	1.1±0.1	8.0
	In dry gas	5.68	55.4	1.4	4.62±0.03	3.4±0.3	0.5±0.2	3.84±0.01	28.1±0.3	0.3±0.1	20.9
	In D_2O vapor	5.68	55.4	1.4	4.61±0.01	3.4	0.6	4.13±0.01	30.0	1.1	12.8

Items without fitting error notations mean that the variables were fixed in the fitting.

The NR analysis provided SLD profiles for Films C and N600, obtained from the optimal fitting results (Figure 5.9). These profiles demonstrated a dependence on the vertical distance from the Si surface, indicating fluctuations in the density and/or composition of the thin films.

At the origin of the vertical axis, the SLD value (2.07×10^{10} cm^{-2}) corresponded to Si, indicating the presence of a Si layer. Additionally, a few nanometers of native SiO_2 layer were observed on the surface of the Si layer, with an SLD value of 3.47×10^{10} cm^{-2}. It was assumed that the structural parameters of Si and its native oxide layer were identical for all samples. The SLD of the carbon film in Film C, used as a fitting parameter, matched that of bulk carbon ($SLD_C = 6.36 \times 10^{10}$ cm^{-2}). However, upon NH_3 treatment, the SLD of the carbon layer in Film N600 decreased to 5.68×10^{10} cm^{-2}. This indicates a change in the density or composition of the carbon film as a result of the NH_3 treatment.

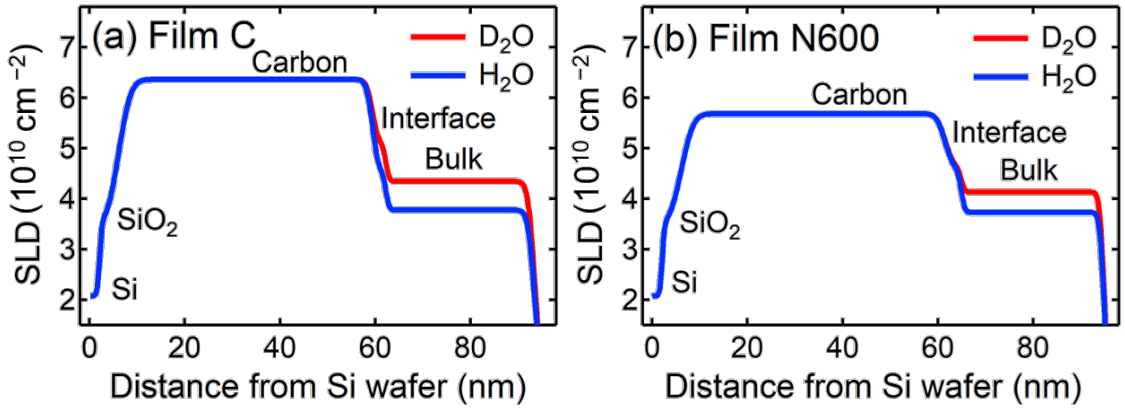

Figure 5.9 SLD profiles of the Nafion ionomer thin films on (a) Film C and (b) Film N600 acquired under H_2O (blue) and D_2O vapors (red). Copyright 2022, American Chemical Society.

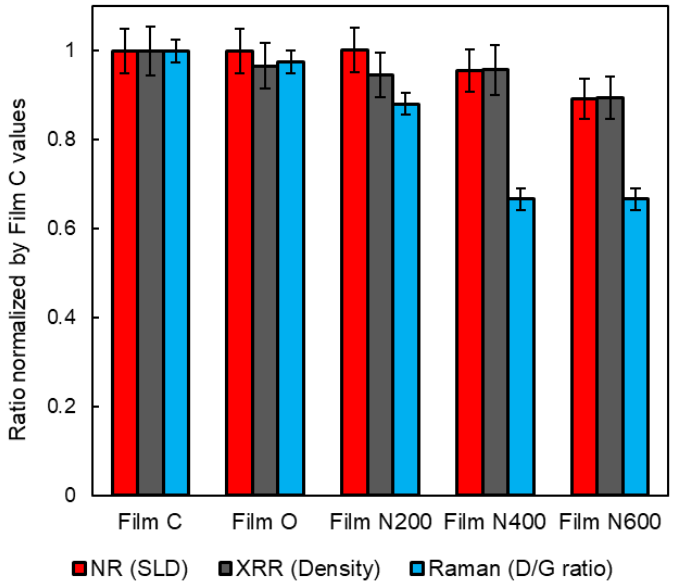

Figure 5.10 Comparison of density variation in carbon film samples.

To validate the reduction in the SLD of the carbon layers after NH_3 treatment, the author performed XRR measurements to determine the density and thickness of the carbon thin films. The XRR data analysis (Figure 5.10) confirmed the decrease in SLD of Film N600, indicating a change in the density or composition of the carbon film. When nitrogen atoms are incorporated into a carbon film, the SLD typically increases due to the larger scattering length of nitrogen compared to carbon. However, in the case of Film N600, the decrease in SLD suggests the introduction of voids ($SLD_V = 0$ cm^{-2}) in the carbon thin films. This corresponds to the formation of approximately 10% voids by volume fraction. The presence of these voids can explain the decrease in SLDs. The SEM and AFM observations (Figure 5.2) confirmed the absence of cracks on the carbon surface, indicating that the voids were not caused by cracks. The degree of lattice defects estimated using Raman spectroscopy was roughly consistent with the decrease in density revealed by XRR and NR analysis (Figure 5.10). Therefore, the decrease in SLD of the carbon layer in Film N600 can be attributed to the presence of lattice defects in the graphene-like plane of the carbon layer. The water contact angle measurements (Figure 5.3) showed a transition from hydrophobic to hydrophilic nature after the NH_3 treatment. This change indicates the presence of open hydrophilic pores on the carbon surface, which can be filled with water driven by capillary forces. However, there were no significant changes in the critical angle of NR profiles, suggesting that the SLD of the carbon layers was not affected by water filling into the hydrophilic voids. The lattice defects, such as point defects, edge defects, and structural distortions, identified by Raman spectroscopy are likely to be too small to be filled with water, further supporting the explanation for the decrease in SLD.

To examine the water distribution in the thin films, the volume fraction of water ϕ_W was determined using the double-contrast method. By substituting D_2O for H_2O, the SLDs of the ionomer layers increased due to the difference in SLDs between the water incorporated by the layers. Figure 5.11 displays the SLD profiles and volume fractions of the Nafion ionomer thin films as a function of vertical distance from the carbon surface, and Table 5.5 summarizes the corresponding parameters. For all samples, the SLD_N ranged from 3.95×10^{10} to 4.17×10^{10} cm^{-2}, which was within ±5% of the molecular volume (0.79 nm^3) in Nafion ionomer. The volume fraction of carbon near the carbon surface decreased over several nanometers of vertical distance due to surface roughness, and this decay became slightly more pronounced from Films C to N600 as a result of damage caused by the NH_3 treatment. At the carbon-ionomer interface, an "ionomer adsorption layer" appeared with an increased ϕ_N compared to the bulk ionomer layer (visible as red profiles at the interface in Figures 5.11f–j). The hydrophobic carbon surface (Film C) had a thin (~1 nm) ionomer adsorption layer, while the hydrophilic carbon surface (Film O) showed a significantly reduced adsorption layer. This difference can be attributed to the adsorption of the ionomer backbone, which exists as rod-shaped aggregates in the bulk, onto the hydrophobic carbon surface following the rupture of the aggregates by hydrophobic interactions. Furthermore, the thickness and volume fraction of the ionomer in the adsorption layer increased after the NH_3 treatment (Films N200–N600) compared to Films C and O. However, instead of a dense ~3 nm ionomer layer observed in Films N200–N600, a decrease in ϕ_W at the interface was observed compared to Films C and O (Table 5.5). The carbon-ionomer interface visually confirmed the loss of water (Figure

5.11c–e), indicating a decrease in water content not only at the interface but also throughout the films. In order to compare the findings with the data presented in specific review articles [20, 21], the ϕ_W at the bulk and interfacial layers was converted to water uptake using a parameter known as λ_W, which represents the number of water molecules per sulfonic group of the ionomer. The swelling ratio ($\Delta L/L_0$) was calculated by considering the total thickness of the bulk and interfacial layers in the dry/wet ionomer films, which was estimated based on the fitted NR profiles. The physicochemical properties are summarized in Table 5.5. Compared to the λ_W value of a bulk Nafion membrane [20] (typically 10–15 at 22 °C), Nafion films with a thickness less than 100 nm exhibit lower λ_W values due to the presence of a "thin-film effect." Previous studies have reported λ_W values ranging from 1.8 to 3.2 at 20–25 °C and 75% RH for ionomer thin films with a thickness of 30 nm [22]. Additionally, the thin-film effect has been observed in terms of swelling thickness, and the results obtained in this study align reasonably well with those reported in previous research [20]. The NR measurements indicate that the water uptake properties deteriorated after NH_3 treatment, particularly in the interfacial layer (as shown in Table 5.5). This observation suggests that the use of N-modified carbon in the cathode catalyst layers may lead to a reduction in fuel cell performance under low-humidity conditions due to the decreased water uptake.

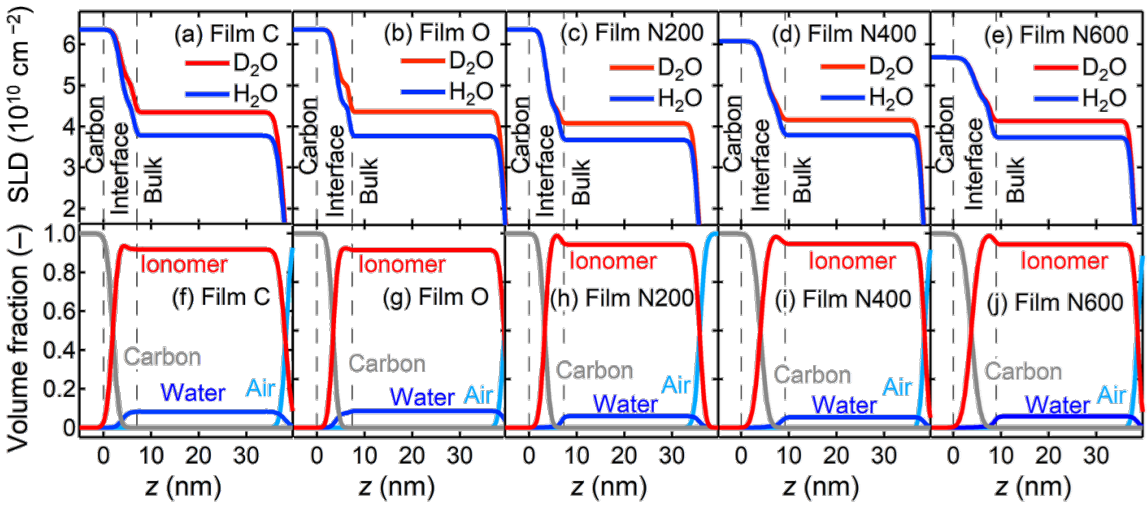

Figure 5.11 (a–e) SLD profiles of Nafion ionomer thin films as a function of vertical distance from the carbon surface z obtained under H_2O (blue) and D_2O vapors (red). (f–j) Volume fractions of the components of the Nafion ionomer thin films. Gray, red, blue, and light blue lines represent carbon, the Nafion ionomer, water, and air, respectively. Copyright 2022, American Chemical Society.

Table 5.5 Physicochemical properties of Nafion ionomer thin films on carbon surfaces.

Film	Layer	ϕ_W (–)[a]	λ_W (–)[a]	$\Delta L/L_0$ (%)[a]
C	Bulk	0.08 ± 0.02	2.3 ± 0.1	9.6 ± 0.1
	Interface	0.08 ± 0.02	2.3 ± 0.1	
O	Bulk	0.09 ± 0.02	2.5 ± 0.1	9.0 ± 0.1
	Interface	0.08 ± 0.02	2.2 ± 0.1	
N200	Bulk	0.06 ± 0.02	1.7 ± 0.1	6.6 ± 0.7
	Interface	0.001 ± 0.001	0.04 ± 0.02	
N400	Bulk	0.05 ± 0.02	1.5 ± 0.1	8.4 ± 0.2
	Interface	0.009 ± 0.002	0.23 ± 0.01	
N600	Bulk	0.06 ± 0.01	1.6 ± 0.1	7.1 ± 0.2
	Interface	0.006 ± 0.002	0.17 ± 0.01	

[a]The ± is defined as the error propagation calculated to account for errors in the parameters determined by the fitting of NR profiles. ϕ_W, λ_W, and $\Delta L/L_0$ represent the volume fraction of water, water uptake, and swelling ratio, respectively.

5.3.3 The Origin of Interactions Between Ionomer and Carbon

The wettability of the carbon surface plays a crucial role in determining the morphology of the ionomer adsorption layer, and N-modified carbon surfaces exhibit hydrophilic characteristics [22, 23]. In wet ionomer thin films, a water-rich layer is observed near the hydrophilic carbon surface treated with ultraviolet irradiation [9]. It is important to note that previous studies have predicted and measured the densification of ionomer at the Pt-Nafion interface [10, 24, 25]. Yang et al. [26] reported variations in the ζ-potential of carbon black, ranging from –1.28 to +74.2 mV, when N functional groups were introduced to the carbon support. The positive charge resulting from the ionization of the quaternary N group is sufficient to attract the negatively charged SO^{3-} groups in the side chains of the Nafion ionomers. This Coulombic interaction enables the positively ionized surface to attract the negatively charged SO^{3-} groups. On as-deposited carbon surfaces, the main chain of the Nafion ionomer adsorbs onto the hydrophobic carbon surface through hydrophobic interactions [22, 27, 28], resulting in the formation of a thin ionomer adsorption layer. However, in the case of N-modified carbon surfaces, the SO^{3-} groups in the side chains of the Nafion ionomers bind to the positively charged surface created by the N functional groups via the Coulombic interaction. As a result, a thick and dense ionomer adsorption layer form at the carbon surface due to the long-range Coulombic interaction.

5.4 Conclusion

The chapter describes a study conducted on carbon surfaces modified with nitrogen through NH_3 treatment. The aim of the study was to investigate the distribution of ionomer on these modified surfaces using NR with the double-contrast method. The results supported the idea that introducing nitrogen to the carbon supports can promote to the formation of a dense ionomer layer at the interface with carbon surfaces. Specifically, a Nafion ionomer adsorption layer, approximately 3 nm thick, was observed on the N-modified carbon surface. This layer exhibited a higher density compared to the bulk layer. The strong interaction between carbon and ionomers may contribute to the suppression of ionomer poisoning on the Pt surface and the reduction of the concentration overpotential.

References

01. Orfanidi, P. Madkikar, H. A. El-Sayed, G. S. Harzer, T. Kratky, H. A. Gasteiger, The Key to High Performance Low Pt Loaded Electrodes, J. Electrochem. Soc. 164 (2017) F418–F426.
02. S. Ott, A. Orfanidi, H. Schmies, B. Anke, H. N. Nong, J. Hübner, U. Gernert, M. Gliech, M. Lerch, P. Strasser, Ionomer Distribution Control in Porous Carbon-Supported Catalyst Layers for High-Power and Low Pt-Loaded Proton Exchange Membrane Fuel Cells, Nat. Mater. 19 (2020) 77–85.
03. K. Matsutori, P. Y. Olu, M. Matsuoka, T. Nakazawa, T. Kinumoto, Carbon Black Functionalized by Grafting of Azo-Generated-Radicals as Electrocatalyst Support for the Oxygen Reduction Reaction, Electrochem. Sci. Adv. 1 (2021) e2100014.
04. G. S. Harzer, A. Orfanidi, H. El-Sayed, P. Madkikar, H. A. Gasteiger, Tailoring Catalyst Morphology towards High Performance for Low Pt Loaded PEMFC Cathodes, J. Electrochem. Soc. 165 (2018) F770–F779.
05. Z. Fang, M. S. Lee, J. Y. Kim, J. H. Kim, T. F. Fuller, The Effect of Carbon Support Surface Functionalization on PEM Fuel Cell Performance, Durability, and Ionomer Coverage in the Catalyst Layer, J. Electrochem. Soc. 167 (2020) 064506.
06. S. Ott, F. Du, M. L. Luna, T. A. Dao, S. Selve, B. R. Cuenya, A. Orfanidi, P. Strasser, Property-Reactivity Relations of N-doped PEM Fuel Cell Cathode Catalyst Supports, Appl. Catal. B 306 (2022)121118.
07. E. Hornberger, T. Merzdorf, H. Schmies, J. Hübner, M. Klingenhof, U. Gernert, M. Kroschel, B. Anke, M. Lerch, J. Schmidt, A. Thomas, R. Chattot, I. Martens, J. Drnec, P. Strasser, Impact of Carbon N-Doping and Pyridinic-N Content on the Fuel Cell Performance and Durability of Carbon-Supported Pt Nanoparticle Catalysts, ACS Appl. Mater. Interfaces 14 (2022) 18420–18430.
08. M. N. Islam, A. B. M. Basha, V. O. Kollath, A. P. Soleymani, J. Jankovic, K. Karan, Designing Fuel Cell Catalyst Support for Superior Catalytic Activity and Low Mass-Transport Resistance, Nat. Commun. 13 (2022) 6157.
09. K. Ito, M. Harada, N. L. Yamada, K. Kudo, H. Aoki, T. Kanaya, Water Distribution in Nafion Thin Films on Hydrophilic and Hydrophobic Carbon Substrates, Langmuir 36 (2020) 12830–12837.
10. A. Nelson, Co-Refinement of Multiple-Contrast Neutron/X-ray Reflectivity Data Using MOTFIT, J. Appl. Crystallogr. 39 (2006) 273–276.
11. Harada, M.; Kudo, K.; Yamada, N. L. Compositional Segregation in a Cross Section of Wet Nafion Thin Film on a Platinum Surface, Chem. Lett. 48 (2019) 51–54.
12. S. C. DeCaluwe, P. A. Kienzle, P. Bhargava, A. M. Baker, J. A. Dura, Phase Segregation of Sulfonate Groups in Nafion Interface Lamellae, Quantified via Neutron Reflectometry Fitting Techniques for Multi-Layered Structures, Soft Matter 10 (2014) 5763–5776.
13. J. A. Dura, V. S. Murthi, M. Hartman, S. K. Satija, C. F. Majkrzak, Multilamellar Interface Structures in Nafion, Macromolecules 42 (2009) 4769–4774.
14. S. A. Eastman, S. Kim, K. A. Page, B. W. Rowe, S. Kang, S. C. DeCaluwe, J. A. Dura, C. L. Soles, K. G. Yager, Effect of Confinement on Structure, Water Solubility, and Water Transport in Nafion

Thin Films, Macromolecules 45 (2012) 7920–7930.

15. T. Kawamoto, M. Aoki, T. Kimura, P. Chinapang, T. Mizusawa, N. L. Yamada, F. Nemoto, T. Watanabe, H. Tanida, M. Matsumoto, H. Imai, J. Miyake, K. Miyatake, J. Inukai, Sublayered Structures of Hydrated Nafion Thin Film Formed by Casting on Pt Substrate Analyzed by X-Ray Absorption Spectroscopy under Ambient Conditions and Neutron Reflectometry at Temperature of 80 °C and Relative Humidity of 30–80%, Electrochemistry 87 (2019) 270–275.
16. T. Kawamoto, M. Aoki, T. Kimura, T. Mizusawa, N. L. Yamada, J. Miyake, K. Miyatake, J. Inukai, In-Plane Distribution of Water inside Nafion Thin Film Analyzed by Neutron Reflectivity at Temperature of 80 °C and Relative Humidity of 30%–80% Based on 4-Layered Structural Model, Jpn. J. Appl. Phys. 58 (2019) SIID01.
17. S. Kim, J. A. Dura, K. A. Page, B. W. Rowe, K. G. Yager, H.-J. Lee, C. L. Soles, Surface-Induced Nanostructure and Water Transport of Thin Proton-Conducting Polymer Films, Macromolecules 46 (2013) 5630–5637.
18. U. N. Shrivastava, H. Fritzsche, K. Karan, Interfacial and Bulk Water in Ultrathin Films of Nafion, 3M PFSA, and 3M PFIA Ionomers on a Polycrystalline Platinum Surface, Macromolecules 51 (2018) 9839–9849.
19. U. N. Shrivastava, K. Suetsugu, S. Nagano, H. Fritzsche, Y. Nagao, K. Karan, Cross-Correlated Humidity-Dependent Structural Evolution of Nafion Thin Films Confined on a Platinum Substrate, Soft Matter 16 (2020) 1190–1200.
20. A. Kusoglu, S. Savagatrup, K. T. Clark, A. Z. Weber, Role of Mechanical Factors in Controlling the Structure−Function Relationship of PFSA Ionomers, Macromolecules (45) 2012 7467–7476.
21. K. Karan, Interesting Facets of Surface, Interfacial, and Bulk Characteristics of Perfluorinated Ionomer Films, Langmuir 35 (2019) 13489–13520.
22. T. Mashio, K. Malek, M. Eikerling, A. Ohma, H. Kanesaka, K. Shinohara, Molecular Dynamics Study of Ionomer and Water Adsorption at Carbon Support Materials, J. Phys. Chem. C 114 (2010) 13739–13745.
23. T. Mabuchi, S. F. Huang, T. Tokumasu, Influence of Ionomer Loading and Substrate Wettability on the Morphology of Ionomer Thin Films Using Coarse-Grained Solvent Evaporation Simulations, Macromolecules 54 (2021) 115–125.
24. K. Kudo, R. Jinnouchi, Y. Morimoto, Humidity and Temperature Dependences of Oxygen Transport Resistance of Nafion Thin Film on Platinum Electrode, Electrochim. Acta 209 (2016) 682–690.
25. R. Jinnouchi, K. Kudo, N. Kitano, Y. Morimoto, Molecular Dynamics Simulations on O_2 Permeation through Nafion Ionomer on Platinum Surface, Electrochim. Acta 188 (2016) 767–776.
26. F. Yang, L. Xin, A. Uzunoglu, Y. Qiu, L. Stanciu, J. Ilavsky, W. Li, J. Xie, Investigation of the Interaction between Nafion Ionomer and Surface Functionalized Carbon Black Using Both Ultrasmall Angle X-ray Scattering and Cryo-TEM. ACS Appl. Mater. Interfaces 9 (2017) 6530–6538.

27. W. Yoshimune, M. Harada, Effect of Pt Loading on the Adsorption of Perfluoro-sulfonic Acid Ionomer in Catalyst Ink for Polymer Electrolyte Fuel Cells. Chem. Lett. 48 (2019) 487–490.
28. Y. Guo, T. Mabuchi, G. Li, T. Tokumasu, Morphology Evolution and Adsorption Behavior of Ionomers from Solution to Pt/C Substrates. Macromolecules 55 (2022) 4245–4255.

Part 2

Structures, Properties, and Formation of Gas Diffusion Layers

Chapter 6

Effect of Compression on Structures and Properties of GDLs

6.1 Introduction

The primary functions of GDLs are to enhance high electron and thermal conductivity, deliver reactant gases from the flow field to the catalyst-coated membrane, and remove water from the PEFC. Determining the appropriate compression pressure during cell assembly is crucial for achieving optimal cell performance [1–3]. Compression pressure plays a role in balancing the ohmic and concentration overpotentials. Higher compression pressure increases the conductive pathways at the interface, thereby promoting electron transfer [4–6]. However, increasing compression pressure decreases GDL porosity and mass transport efficiency [1, 2]. Typically, compression pressures of 0.5–2 MPa are applied to the cell assembly, resulting in 10–40% compression based on the initial thickness. Under these compression conditions, the bulk porosity of GDL substrates is 50–70%. In the case of MPLs, compression pressure causes thickness reduction [7]. However, the pore morphologies of MPLs have not been adequately evaluated using X-ray micro-CT (X-μCT) due to its limited spatial resolution (1 μm) in analyzing micropores within MPLs (~100 nm). Analytical techniques such as X-ray nano-CT (X-nCT) with a nanoscale spatial resolution [8, 9] and focused ion beam scanning electron microscopy (FIB-SEM) [8] are suitable for analyzing these micropores but have been limited to uncompressed MPLs. To overcome this limitation, this chapter presents a method for analyzing the pore size distribution of compressed GDLs using mercury intrusion porosimetry with a compression device. It is stated that the combination of X-μCT with mercury intrusion porosimetry provides insight into the multiscale pore morphologies of compressed GDLs.

6.2 Experimental

6.2.1 Materials

This study used a commercial GDL (Sigracet 29BC, SGL Carbon) with a thickness of 235 ± 20 μm and containing 5 wt% PTFE. The catalyst-coated membrane (CCM) was prepared using commercial Pt nanoparticles supported on carbon black (TEC10E50E, Tanaka Kikinzoku Kogyo), Nafion dispersion (D2020, Chemours), and Nafion electrolyte membrane (NR211, Chemours). A catalyst ink consisting of a catalyst, Nafion dispersion, and a mixture of ethanol and deionized water was applied onto a decal sheet using an applicator. The CL was then dried and hot-pressed at 145 °C for 10 minutes on both sides of the membrane. The weight ratio of Nafion to the carbon support was 0.75, and the Pt loading of the CL was 0.3 mg cm^{-2}.

6.2.2 Fuel Cell Tests

For the fuel cell setup, a single cell (1 cm^2) with straight channels was used, where the channel width

and rib width were 0.4 mm and 0.2 mm, respectively. The anode and cathode flow fields were configured in a cross-flow arrangement. The compression of the GDL was adjusted by controlling the gasket thickness (Figure 6.1a). The compression level *C* was calculated:

$$C = \frac{(d_{\mathrm{GDL\_ini}} - d_{\mathrm{gasket}})}{d_{\mathrm{GDL\_ini}}}, \tag{6.1}$$

where d_{gasket} is the thickness of the gasket and $d_{\mathrm{GDL\text{-}ini}}$ is the initial thickness of GDLs.

The break-in and polarization tests were performed using a constant flow of air/H_2 (2000/500 sccm) under a backpressure of 50 kPa for both the cathode and anode. The break-in test involved sweeping the cell voltage between 0 and 1.0 V at a scan rate of 10 mV s^{-1}, repeated 50 times at 80 °C with 100% RH. The oxygen transport resistance was evaluated using the limiting current method. The limiting current was measured with diluted O_2 in N_2 gas and excess H_2 at 60 °C and 80% RH. The gases were introduced into the cell at flow rates of 500 sccm for H_2 and 200 sccm for 1% O_2 under back pressures of 50, 100, 150, and 200 kPa on both the cathode and anode. The polarization curves were measured by sweeping the cell voltage between 0.08 and 1.0 V at a scan rate of 10 mV s^{-1}. The largest current in the polarization curve was assigned to the limiting current density. The oxygen transport resistance R_{exp} was calculated using the equation:

$$R_{\mathrm{exp}} = \frac{4FP_{\mathrm{O_2}}}{I_{\mathrm{lim}}RT}, \tag{6.2}$$

where I_{lim} is the limiting current density, P_{O2} is the oxygen partial pressure, *F* is Faraday's constant, *R* is the gas constant, and *T* is the cell temperature. In the context of oxygen transport resistance, the equation that describes the components of R_{exp} is given as follows:

$$R_{\mathrm{exp}} = P_{\mathrm{abs}}R_{\mathrm{mole}} + R_{\mathrm{other}}, \tag{6.3}$$

where *P* represents the total backpressure, R_{mol} corresponds to the pressure-dependent resistance caused by molecular diffusion, and R_{other} represents the pressure-independent resistance resulting from Knudsen diffusion within the CL.

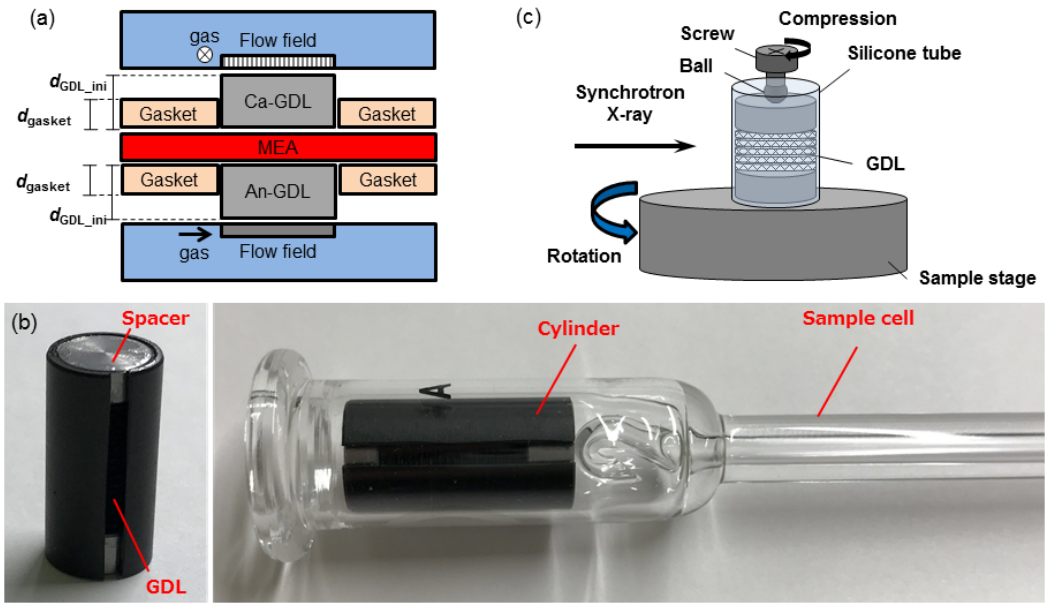

Figure 6.1 (a) Configuration for 1 cm^2 single cell. (b) Photograph of a compression device for mercury intrusion porosimetry measurements. (c) Setup for X-μCT measurements. Copyright 2020, Elsevier.

6.2.3 Pore Characterization

The total porosity of uncompressed GDLs was determined by filling the pores of a pre-weighed GDL with a hard-to-evaporate liquid (Silwick, PMI) and measuring the weight change. The total porosity ε_{GDL_ini} was calculated using the formula:

$$\varepsilon_{GDL\_ini} = \frac{(M - m)}{\rho V}, \tag{6.4}$$

where ρ is the density of the immersed liquid, V is the volume of the pre-weighed GDL, m is the weight of the pre-weighed GDL, and M is the weight of the immersed GDL, respectively. A piece of GDLs (3 × 3 cm^2) was used for the measurements, and replicate measurements were performed three times.

The pore size distribution analysis of compressed GDLs was conducted using mercury intrusion porosimetry (PoreMaster 60GT, Quantachrome Instruments). GDL samples with a diameter of 7 mm were punched out using a compression device (Figure 6.1b) and placed in the sample chamber for analysis. The compression device consisted of a cylinder and spacers, with the GDL samples sandwiched between the spacers and fixed inside the cylinder using an adhesive. The cylinder had a 2 mm wide slit through which mercury was introduced. The compression levels tested were 0%, 8.6%, 23.6%, and 38.6%, which were achieved by adjusting the length of the spacers.

X-μCT experiments were carried out at the Toyota Beamline (BL33XU) at SPring-8. A total of eight stacked GDL samples with a diameter of 4 mm were placed in an acrylic pipe on a stage (Figure 6.1c). A compression cell equipped with a screw and spacers was utilized to compress the sample, and the compression level was adjusted by tightening the screw. A stainless ball was placed between the screw and the spacer. X-μCT images were acquired at compression levels of 0%, 9.8%, 17.3%, 25.4%, and

35.8%. A total of 1800 projections were measured using an X-ray energy of 14 keV, and the field of view was fixed at 4.8 × 2.6 mm². Tomographic reconstruction was performed using software provided by JASRI [10], and the segmented CT image was analyzed using Fiji software (ImageJ) [11]. The pore size distribution and effective diffusivity were evaluated using the SatuDict and DiffuDict modules in Geodict software [12].

6.3 Results and Discussion

6.3.1 Fuel Cell Performance with Varied GDL Compression

Figure 6.2a illustrates the polarization curves obtained at different compression conditions (17.4%, 31.1%, and 40.4%) at 60 °C and 80% RH. It was observed that the cell performances remained unaffected at lower current densities, maintaining a voltage of 0.85 V within the compression range. However, as the compression increased, there was a significant decline in cell performance at higher current densities. The R_{exp} increased from 57.8 to 66.4 s m^{-1} across the compression range (Figure 6.2b). This observation is consistent with a previous study [3], which suggests that alterations in the pore structures of the GDL are responsible for this trend. The subsequent section provides a detailed discussion of these morphological changes.

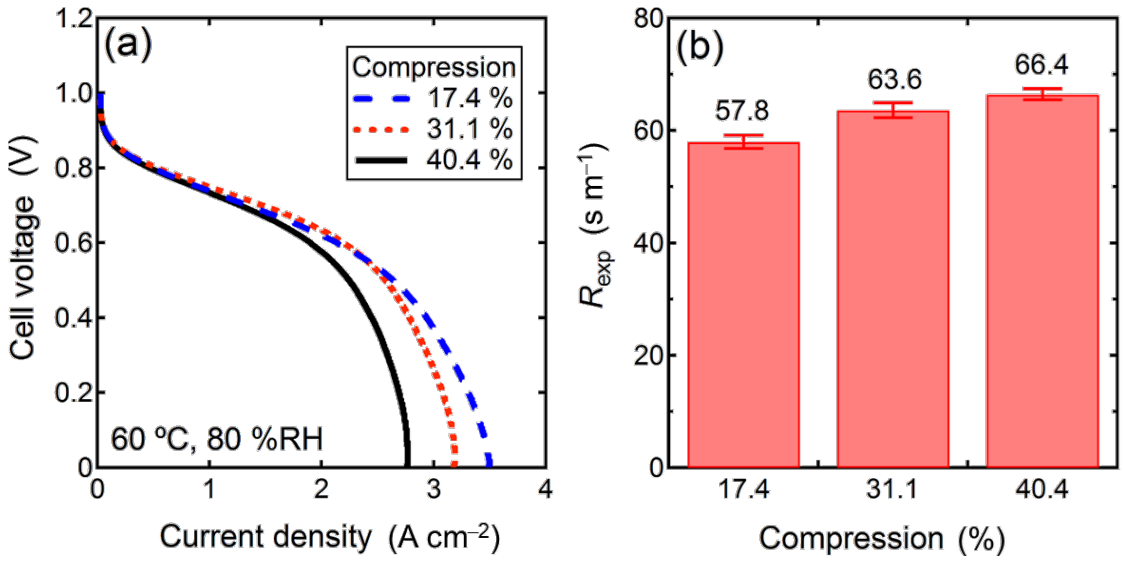

Figure 6.2 (a) Polarization curves for three compressed conditions (17.4, 31.1, and 40.4%). The fuel cell test was operating at 60 °C and 80% RH. (b) The oxygen transport resistance R_{exp} under each compression condition. Copyright 2020, Elsevier.

6.3.2 Pore Characterization of Compressed GDLs

The pore size distribution of compressed GDLs was analyzed using mercury intrusion porosimetry with a designed compression device. The presence of voids in the device, as shown in Figure 6.3, did not affect the evaluation of pore distribution in the GDLs, as these voids were larger than the pores in the GDLs. Figure 6.4a displays the pore size distribution of compressed GDLs at different compression levels. At zero compression, discrete ranges of pores were observed in both the fibrous substrate (29.2 μm) and the MPL (90 nm). As the compression increased, the peak corresponding to macropores in the substrate shifted to the left, indicating a reduction in the average pore diameter from 29.2 μm (0%) to 2.7 μm (38.6%). The average pore diameter of the micropores within the MPL remained unchanged with compression. It is worth noting that the measurements were reproducible, and there was no structural deformation caused by mercury intrusion, as confirmed in Figure 6.5. Figure 6.4b presents the pore size distribution of the compressed GDL obtained from reconstructed three-dimensional X-μCT images. The low spatial resolution (1.3 μm) limited the study of micropores within MPLs. As compression was applied, the average pore diameter of macropores in the substrate decreased from 40.3 μm (0%) to 9.1 μm (35.8%). These values are consistent with a previous study (0%: 34.9 μm, 34%: 11.4 μm, and 41%: 9.67 μm) [7] and align with the results of mercury intrusion porosimetry. Figure 6.4c shows the volume of the total and individual components (total/void/MPL/substrate). The volume of the substrate remained almost constant, indicating its rigid nature. However, the volume of the void decreased monotonically across the compression range. Additionally, the volume of the MPL remained constant until 17.3% compression and then decreased further to 25.4%. The reduction in MPL volume can be attributed to the compression of invisible voids within the MPL under applied pressure, which is supported by the results of mercury intrusion porosimetry measurements (Figure 6.4a).

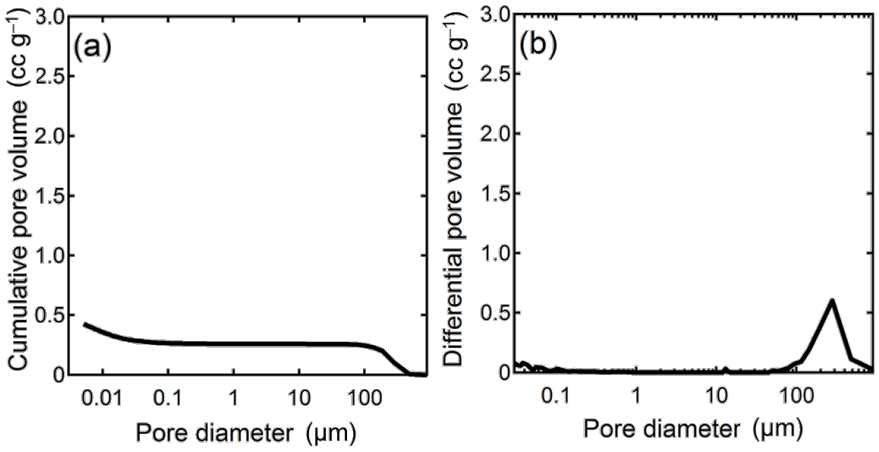

Figure 6.3 Pore size distribution of an empty cell with a compression device measured by mercury intrusion porosimetry.

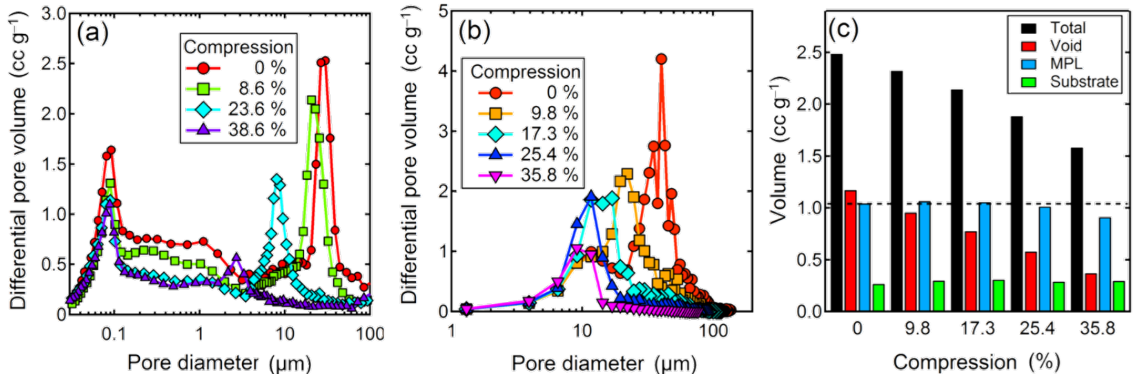

Figure 6.4 Pore size distribution of a GDL with various compression levels measured by (a) mercury intrusion porosimetry and (b) X-μCT. (c) The volume of total, void, MPL, and substrate is summarized at discrete compression. Each volume was calculated from the data obtained by X-μCT experiments. Copyright 2020, Elsevier.

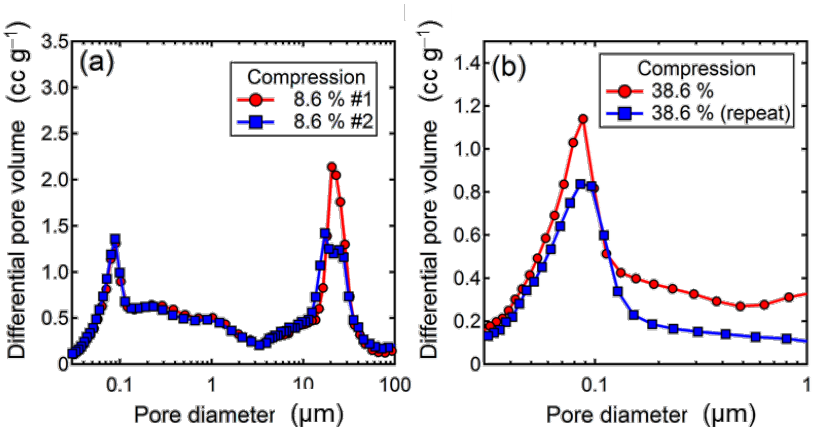

Figure 6.5 Pore size distribution of a compressed GDL with a compression device measured by mercury intrusion porosimetry: (a) Twice measurements (#1, #2) in different cells and (b) continuous measurements in the same sample.

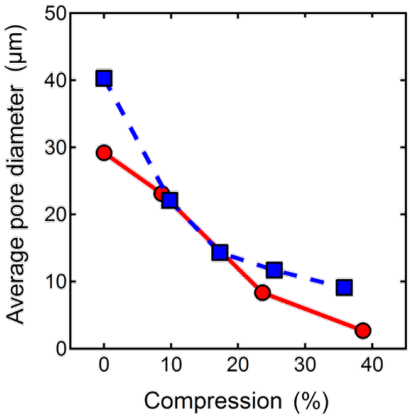

Figure 6.6 The average pore diameters of the macro-pores within the fibrous substrate as a function of compression. Red circles and blue squares is the results of mercury intrusion porosimetry and X-μCT, respectively.

6.3.3 Effective Diffusivity and Its Effect on Fuel Cell Performance

The local effective diffusion coefficient of oxygen in each component of GDLs ($D_{\mathrm{eff}}(x)$ is 0, D_{M}, and $D_{\mathrm{eff\_MPL}}$ at x = substrate, void, and MPL, respectively). Here, D_{M} represents the oxygen molar diffusion coefficient in nitrogen. The value of D_{M} at 60 °C and 1.5 atm was 1.68×10^{-5} m^2 s^{-1} using the Chapman-Enskog equation [13]. $D_{\mathrm{eff\_MPL}}$ can be approximated using the Bosanquet equation [14]:

$$D_{\mathrm{eff\_MPL}} = \left({D_{\mathrm{M}}}^{-1} + {D_{\mathrm{Kn}}}^{-1}\right)^{-1} \frac{\varepsilon_{\mathrm{MPL}}}{\tau_{\mathrm{MPL}}}. \tag{6.5}$$

Here, $\varepsilon_{\mathrm{MPL}}$ and τ_{MPL} represent the tortuosity and porosity of MPLs, and D_{Kn} corresponds to the Knudsen diffusion coefficient:

$$D_{\mathrm{Kn}} = \frac{dv}{3}, \tag{6.6}$$

where d and v denote the pore diameter of MPLs and the average oxygen velocity. In this study, the value of v was 470 m s^{-1}, and d was fixed at 9.0×10^{-8} m, derived from mercury intrusion porosimetry experiments (Figure 6.4a). By applying the Bruggeman relationship [15], $D_{\mathrm{eff\_MPL}}$ can be rewritten as

$$D_{\mathrm{eff\_MPL}} = \left({D_{\mathrm{M}}}^{-1} + {D_{\mathrm{Kn}}}^{-1}\right)^{-1} {\varepsilon_{\mathrm{MPL}}}^{1.5}. \tag{6.7}$$

All invisible voids observed in X-μCT measurements exist within the MPL $\varepsilon_{\mathrm{MPL\_ini}}$ can be approximated as:

$$\varepsilon_{\mathrm{MPL\_ini}} = \frac{V_{\mathrm{V\_MPL\_ini}}}{V_{\mathrm{MPL\_ini}}} = \frac{(\varepsilon_{\mathrm{GDL\_ini}} V_{\mathrm{GDL\_ini}} - V_{\mathrm{V\_ini}})}{V_{\mathrm{MPL\_ini}}}, \tag{6.8}$$

where $V_{\mathrm{MPL\_ini}}$, $V_{\mathrm{V\_MPL\_ini}}$, $V_{\mathrm{GDL\_ini}}$, and $V_{\mathrm{V\_ini}}$ represent the initial volume of the MPL, voids within the MPL, GDL, and total voids, respectively. Here, $\varepsilon_{\mathrm{GDL\_ini}}$ was 0.748 from pore-filling experiments. The porosity of compressed MPLs $\varepsilon_{\mathrm{MPL\_comp}}$ can be expressed as

$$\varepsilon_{\mathrm{MPL\_comp}} = \frac{\left\{V_{\mathrm{MPL\_comp}} - (1 - \varepsilon_{\mathrm{MPL\_ini}}) V_{\mathrm{MPL\_ini}}\right\}}{V_{\mathrm{MPL\_comp}}}. \tag{6.9}$$

Here, $V_{\mathrm{MPL\_comp}}$ denotes the volume of compressed MPLs. Thus, the porosity of MPLs can be calculated for each compression condition.

The effective diffusivity of oxygen in compressed GDLs $D_{\mathrm{eff\_GDL}}$ was calculated using the Geodict software based on segmented X-μCT images. For a detailed explanation, refer to Becker et al. [16]. $D_{\mathrm{eff\_GDL}}$ can be converted to the calculated oxygen transport resistance R_{cal} as follows:

$$R_{\mathrm{cal}} = \frac{d_{\mathrm{GDL\_comp}}}{D_{\mathrm{eff\_GDL}}}, \tag{6.10}$$

where $d_{\mathrm{GDL\_comp}}$ represents the thickness of the compressed GDL, which is equal to d_{gasket} in fuel cell testing (Figure 6.1a). The compression corresponding to the fuel cell testing was estimated using linear interpolation (Figure 6.7). Figure 6.8 compares the experimental and calculated values of oxygen transport resistance. The guideline represents cases where the calculated value matches the experimental value, while plots below the guideline indicate underestimation in the calculated values. In all three conditions, the plots are located below the guideline, indicating that the calculated values underestimate

the experimental values. This underestimation is attributed to the inclusion of R_{other}, which represents the Knudsen diffusion resistance at the CL. The modified calculated oxygen transport resistance ($R_{cal}' = R_{cal} + R_{other}$) was plotted in the figure. The agreement between calculated and experimental values indicates that the proposed method is suitable for calculating the oxygen transport resistance in a compressed GDL.

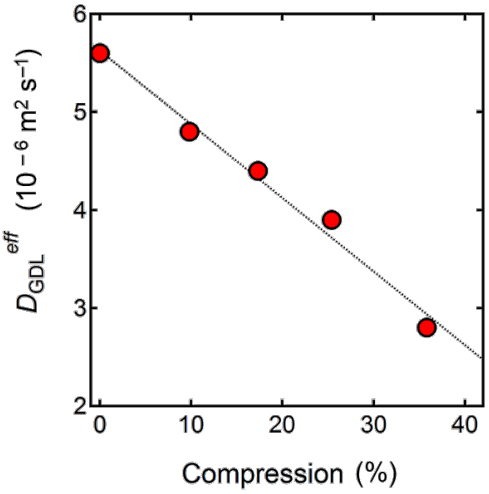

Figure 6.7 D_{eff_GDL} as a function of compression level. Copyright 2020, Elsevier.

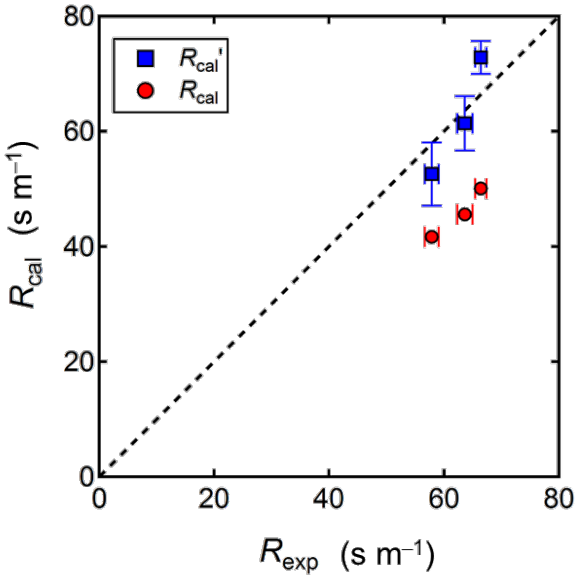

Figure 6.8 Comparison of R_{exp} determined by fuel cell tests and R_{cal} based on the structural properties. R_{cal}' (= R_{cal} + R_{other}) are plotted in this figure. The guideline indicates the calculated value is equal to the experimental value. Copyright 2020, Elsevier.

6.4 Conclusion

This chapter focused on investigating the impact of compression on the pore morphologies of GDLs and its subsequent effects on fuel cell performance. It was observed that high compression levels of GDLs led to increased oxygen transport resistance and reduced cell performance, particularly at high current densities. To examine the changes in pore morphologies, the author employed mercury intrusion porosimetry combined with a compression device and synchrotron X-μCT. Mercury intrusion porosimetry allowed for the observation of the reduction in the average pore diameter of macropores within the fibrous substrate of the GDL upon compression. The micropores (90 nm) within the MPL remained unchanged even under applied pressures up to 38.6%. Furthermore, the author calculated the oxygen transport resistance using structural parameters obtained from the combination of mercury intrusion porosimetry and X-μCT experiments on the compressed GDL. The calculated oxygen transport resistance agreed with the experimental values obtained through fuel cell tests. Results show that the structural parameters of the fibrous substrate and MPL in the compressed GDL provide valuable information for evaluating the oxygen transport resistance.

References

01. M. B. Sassin, Y. Garsany, B. D. Gould, K. Swider-Lyons, Impact of Compressive Stress on MEA Pore Structure and Its Consequence on PEMFC Performance, J. Electrochem. Soc. 163 (2016) F808–F815.
02. C. Simon, F. Hasché, H. A. Gasteiger, Influence of the Gas Diffusion Layer Compression on the Oxygen Transport in PEM Fuel Cells at High Water Saturation Levels, J. Electrochem. Soc. 164 (2017) F591–F599.
03. J. Millichamp, T. J. Mason, T. P. Neville, N. Rajalakshmi, R. Jervis, P. R. Shearing, D. J. L. Brett, Mechanisms and Effects of Mechanical Compression and Dimensional Change in Polymer Electrolyte Fuel Cells – A Review, J. Power Sources 284 (2015) 305–320.
04. S. Prass, S. Hasanpour, P. K. Sow, A. B. Phillion, W. Mérida, Microscale X-Ray Tomographic Investigation of the Interfacial Morphology between the Catalyst and Micro Porous Layers in Proton Exchange Membrane Fuel Cells, J. Power Sources 319 (2016) 82–89.
05. T. J. Mason, J. Millichamp, T. P. Neville, A. El-Kharouf, B. G. Pollet, D. J. L. Brett, Effect of Clamping Pressure on Ohmic Resistance and Compression of Gas Diffusion Layers for Polymer Electrolyte Fuel Cells, J. Power Sources 219 (2012) 52–59.
06. G. Karimi, X. Li, P. Teertstra, Measurement of Through-Plane Effective Thermal Conductivity and Contact Resistance in PEM Fuel Cell Diffusion Media, Electrochim Acta 55 (2010) 1619–1625.
07. R. W. Atkinson III, Y. Garsany, B. D. Gould, K. E. Swider-Lyons, I. V. Zenyuk, The Role of Compressive Stress on Gas Diffusion Media Morphology and Fuel Cell Performance, ACS Appl. Energy Mater. Interfaces 1 (2017) 191–201.
08. E. A. Wargo, T. Kotaka, Y. Tabuchi, E. C. Kumbur, Comparison of Focused Ion Beam Versus Nano-Scale X-Ray Computed Tomography for Resolving 3-D Microstructures of Porous Fuel Cell Materials, J. Power Sources 241 (2013) 608–618.
09. S. Yamaguchi, S. Kato, W. Yoshimune, D. Setoyama, A. Kato, Y. Nagai, T. Suzuki, A. Takeuchi, K. Uesugi, Observation of Water Droplets in Microporous Layers for Polymer Electrolyte Fuel Cells by X-Ray Computed Nano-Tomography, J. Synchrotron Rad. 29 (2022) 1258–1264.
10. K. Uesugi, M. Hoshino, A. Takeuchi, Y. Suzuki, N. Yagi, T. Nakano, Development of Fast (Sub-Minute) Micro-Tomography, AIP Conf. Proc. 1266 (2010) 47–50.
11. Schneider, C. A.; Rasband, W. S.; Eliceiri, K. W. NIH Image to ImageJ: 25 Years of Image Analysis, Nat. Methods 9 (2012) 671–675.
12. GeoDict-The Digital Material Laboratory. https://www.geodict.com/ (accessed 2023-05-31).
13. J.M. Smith, in: Chemical Engineering Kinetics, 3rd ed, McGraw Hill Book Co., New York, 1981, p. 11. Ch.
14. W.G. Pollard, R. D. Present, On Gaseous Self-Diffusion in Long Capillary Tubes, Phys. Rev. 73 (1948) 762–774.

15. D. A. G. Bruggeman, Calculation of Different Physical Constants of Heterogeneous Substances: I. Dielectric Constant and Conductivity of Media of Isotropic Substances, Ann. Phys. 24 (1935) 636–664.
16. J. Becker, C. Wieser, S. Fell, K. Steiner, A Multi-Scale Approach to Material Modeling of Fuel Cell Diffusion Media, Int. J. Heat Mass Transfer 54 (2011) 1360–1368.

Chapter 7

Gas Transport Properties of Partially Saturated GDLs

7.1 Introduction

In order to design the physical properties of wet GDLs, it is crucial to directly evaluate the oxygen transport resistance in PEFCs at wet conditions. Various evaluation methods have been proposed to assess gas transport properties, depending on the specific application [1–14]. An electrochemical approach using limiting currents has been widely employed to measure the gas transport resistance of GDLs, as it must align with other properties of the PEFC component, such as mechanical strength, electrical conductivity, and water removal capacity. However, the obtained gas transport resistance encompasses contributions from the entire PEFC component, requiring experimental separation. Limiting current measurement with gas pressure control has been extensively used to determine the molecular diffusion resistance of GDLs [10]. Additionally, limiting current measurement as a function of GDL thickness (i.e., the number of stacked GDL sheets) has been employed to isolate the gas transport resistance of GDLs [12]. Direct measurements offer an alternative approach to studying the oxygen transport properties of GDLs. Classical Wicke-Kallenbach cells [1–3] or Loschmidt-type cells [4, 5] have been widely used to evaluate the gas diffusivity of GDLs. Utaka et al. proposed a method to measure the through-plane effective diffusion coefficient in GDLs using a galvanic oxygen sensor [6, 7]. Recently, Gostick et al. developed an experimental method to measure the in-plane effective diffusion coefficient in GDLs using an optical oxygen sensor [8, 9]. The authors' work introduced a simple method to evaluate the through-plane effective diffusion coefficient in dry GDLs using an infrared carbon dioxide sensor [13, 14]. Only a few studies have compared the gas diffusivity in dry GDLs obtained by different evaluation methods, and none have been conducted for partially wet GDLs. This is primarily due to concerns regarding potential variations in results due to differences in humidification conditions between different experimental setups or environments. In this chapter, the author introduces an examination of the oxygen transport resistance of GDLs employing three distinct approaches: (i) direct measurements using the Wicke-Kallenbach-type cell, limiting current measurements using a fuel cell setup, focusing on the dependence of (ii) gas pressure and (iii) GDL thickness. An intriguing aspect of this study is that all three evaluation methods shared the same cell and gas line configuration for acquiring gas transport properties. This approach allowed us to carefully analyze and compare the experimental results obtained from the three methods, eliminating the influence of discrepancies arising from the measurement environment.

7.2 Experimental

7.2.1 Materials

A nonwoven carbon paper with a thickness of 215 ± 20 μm and containing 5 wt % PTFE (Sigracet 22BB, SGL) was used as received. This commercial GDL had a MPL on one side. A slurry for CLs was prepared by ultrasonication of a mixture consisting of 7.4 wt % commercial Pt catalyst supported on carbon black (TEC10E50E, Tanaka Kikinzoku Kogyo), 14.1 wt % Nafion ionomer dispersion (D2020, Chemours), and 78.5 wt % ethanol/ultrapure water mixture as a dispersant. The nonvolatile content in the slurry was 10 wt %, and the water/alcohol ratio in the dispersant was 70/30 wt %. The weight ratio of Nafion ionomer to carbon support was 0.76. The viscous slurry was applied to a PTFE decal sheet using an applicator, dried at 25 °C, and then annealed at 80 °C for 1 hour. The CL was subsequently hot-pressed onto both sides of a Nafion membrane (NR211, Chemours) at 120 °C for 10 minutes. The Pt loading in the cathode CL was 0.12 mg_{Pt} cm^{-2}.

7.2.2 Synchrotron X-μCT

Synchrotron X-μCT experiments were conducted at Toyota Beamline (BL33XU) of the SPring-8 facility to study the morphologies of GDL sheets with a diameter of 5 mm. An X-ray energy used was 20 keV, and the pixel size was 1.3 μm. An offset scan was performed using the on-the-fly method with 3600 projections during a 360° continuous rotation. Tomographic reconstruction was carried out using software provided by JASRI [15], and segmentation and analysis were conducted using ImageJ [16] and GeoDict [17].

7.2.3 Mercury Intrusion Porosimetry

The pore size distribution of GDLs was studied using mercury intrusion porosimetry (PoreMaster 60GT, Quantachrome Instruments). In-house equipment was used to study the pore morphologies of GDLs under a 15% compression ratio. Further details about the compression device is described in Chapter 6.

7.2.4 Direct Measurements of Oxygen Transport Properties

The effective diffusion coefficients of oxygen in GDLs were determined by measuring the mutual diffusion resistance of oxygen and nitrogen using the Wicke-Kallenbach type cell. Figure 7.1 provides an illustration of the experimental setup and the cell configuration. The experimental setup involved passing a flow of synthetic air (containing 20.999% O_2) and pure nitrogen at ambient pressure alternately over the diffusion cell. The diffusion cell consisted of GDLs with an effective diffusion area of 1 cm^2, which were sandwiched between parallel flow fields with straight channels. The channel width was 0.4 mm, and the rib width was 0.2 mm.

The diffusion flux of oxygen J_{O2} along the through-plane direction (z-axis) of GDLs was determined by measuring the outlet gas concentrations at both sides ($C_{outlet(air)\_O2}$ and $C_{outlet(N2)\_O2}$) using galvanic oxygen sensors (JKO-25LJD3, JIKCO). Under steady-state conditions, J_{O2} is described by

$$J_{O_2} = -D_{\text{eff}} \frac{dC_{O_2}}{dz}, \tag{7.1}$$

where C_{O2} is the oxygen molar concentration. The diffusion flux can also be expressed as

$$J_{O_2} = -D_{\text{eff}} \frac{C_{\text{outlet}(N_2)_{O_2}} v}{A}, \tag{7.2}$$

where v is the outlet volumetric flow rate at the nitrogen side, and A is the effective area for diffusion. The oxygen molar fraction gradient is given by the logarithmic mean gradient ΔC_{O2} and the GDL thickness L:

$$\frac{dC_{O_2}}{dz} = \frac{\Delta C_{O_2}}{L}. \tag{7.3}$$

The effective oxygen diffusion coefficient is calculated as

$$D_{\text{eff}} = \frac{C_{\text{inlet(air)\_}O_2} v_{\text{air}} \mathrm{L}}{A \Delta C_{O_2}}. \tag{7.4}$$

In order to validate the measurement system, the flow rates and GDL thicknesses were controlled. The standard cell configuration involved using two GDL sheets with a compression ratio of 15 ± 1% based on their initial thickness. The gas line can be switched to humidification using a bubbler installed upstream of the gas lines. The differential pressure in the system was monitored, ensuring that it remained below the limit of the differential pressure indicator (<1 Pa). Fine-tuning of the nitrogen flow rate was performed to control the differential pressure and prevent the permeate gas flow from being driven by the differential pressure.

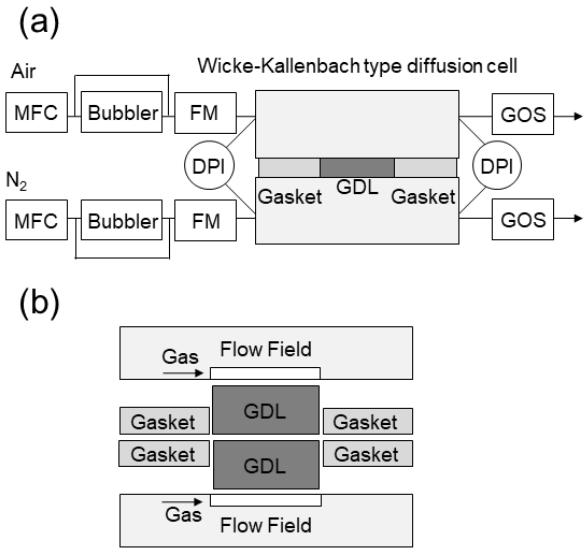

Figure 7.1 (a) Experimental setup for direct measurements of oxygen transport properties: mass flow controller, flow meter, differential pressure indicator, galvanic oxygen sensor, and gas diffusion layer are abbreviated as MFC, FM, DPI, GOS, and GDL, respectively. (b) Configuration of the Wicke-Kallenbach type cocurrent diffusion cell. Copyright 2023, American Chemical Society.

7.2.5 Oxygen Transport Properties Using Limiting Current Approach

Limiting currents were measured using a 1 cm² single cell with straight channels in a crossflow configuration (Figure 7.2). The cell had a CCM stacked between the GDLs. The GDL compression ratio was 15 ± 1%, which was the same as for the direct measurements. For break-in, the cell was set at 60 °C and 100% RH under a constant flow of 2.0 L min^{-1} air and 0.5 L min^{-1} H_2 at 50 kPa gauge pressure for the cathode and anode. The cell voltage was swept 100 times between 0 and 1.0 V at a scan rate of 100 mV s^{-1}. Polarization curves for acquiring limiting currents were collected at different temperature and RHs, with gauge pressures of 0, 50, 100, and 150 kPa, under a gas flow of 2.0 L min^{-1} 1% O_2 and 0.5 L min^{-1} 10% H_2 for the cathode and anode, respectively. The cell voltage was swept three times between 0.08 and 1.0 V at a scan rate of 10 mV s^{-1}. The maximum current in the third scan was determined as the limiting current density I_{lim}. The total oxygen transport resistance R_T is calculated as follows:

$$R_T = \frac{4FP_{O_2}}{I_{lim}RT}, \tag{7.5}$$

where P_{O2} is the oxygen partial pressure, F is Faraday's constant, R is the gas constant, and T is the cell temperature. The total gas transport resistance is further expressed as

$$R_T = P_{abs}R_{mole} + R_{other}, \tag{7.6}$$

where P_{abs} is the absolute pressure, R_{mole} is the pressure-dependent resistance induced by molecular diffusion, and R_{other} is the pressure-independent resistance. The gas transport resistance of GDLs R_{GDL} is primarily attributed to R_{mole}, while the gas transport resistance of CLs R_{CL} is primarily attributed to R_{other}. To investigate the dependence of R_T on the GDL thickness, the number of GDL sheets was varied. The gas transport resistance is separated into two components as

$$R_T = R_{CL} + NR_{GDL}, \tag{7.7}$$

where N is the number of cathode GDL sheets. It should be noted that this separation neglects the influence of molecular diffusion resistance due to the flow field and the gaps between GDLs.

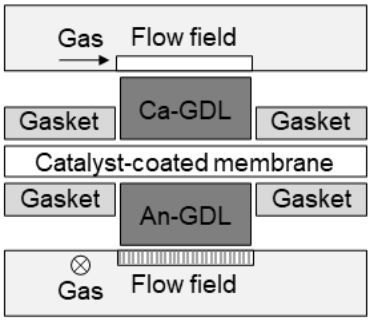

Figure 7.2 Single-cell configuration for limiting current measurements. Copyright 2023, American Chemical Society.

7.3 Results and Discussion

7.3.1 Morphologies of GDLs

Figure 7.3a presents an X-μCT image of a GDL sample, where the fibrous substrate appears as black and the MPL as gray. The transparent areas represent pores within the sample. Although the MPL layer fully covers the substrate, it exhibits cracks. In Figure 7.3b, a cross-sectional X-μCT image shows cracks extending through the MPL and an indistinct interface between the MPL and substrate, which is known as the MPL intrusion layer. Figure 7.3c displays the volume fractions of the MPL, substrate, and pores in the GDL along the through-plane direction. It is important to note that the resolution of the X-μCT measurements (1.3 μm) was insufficient for identifying nanoscale pores in the MPL. Consequently, the volume fraction of the MPL was overestimated as MPL pores were counted as MPL solids [10]. The MPL volume fraction exhibited a broad peak in volume fraction with a maximum value of 0.9, indicating an uneven surface and approximately 10% volume fraction of cracks. The substrate volume fraction showed an inhomogeneous distribution along the through-plane direction, suggesting nonuniformity in carbon fiber and binder distribution within the GDL [10, 13]. Assuming a volume ratio of 0.3–0.7 for the MPL intrusion layer (MPL / (MPL + substrate)), the thickness of MPL intrusion layer was 33 μm. When considering the intersection of MPL and pore volume fractions on the MPL surface as the top of the MPL surface, the total MPL thickness, including the MPL intrusion layer, was approximately 85 μm. Since the MPL intrusion layer accounted for approximately 40% of the total thickness, the presence and impact of the MPL intrusion layer on the concentration overpotential have been extensively debated [18–21]. Figure 7.4a presents the pore size distribution of GDLs, showing three characteristic peaks: substrate pores (>10 μm), MPL-intruded substrate pores (approximately 1 μm), and MPL pores (approximately 0.1 μm). Under a compression ratio of 15%, the diameter of substrate pores and the volume of MPL-intruded substrate pores decreased. Figure 7.4b shows the porosity of GDLs normalized to the cumulative pore volume using the total sample volume. The total GDL porosity was 0.77 in the uncompressed state and decreased to 0.71 at a compression rat io of 15%.

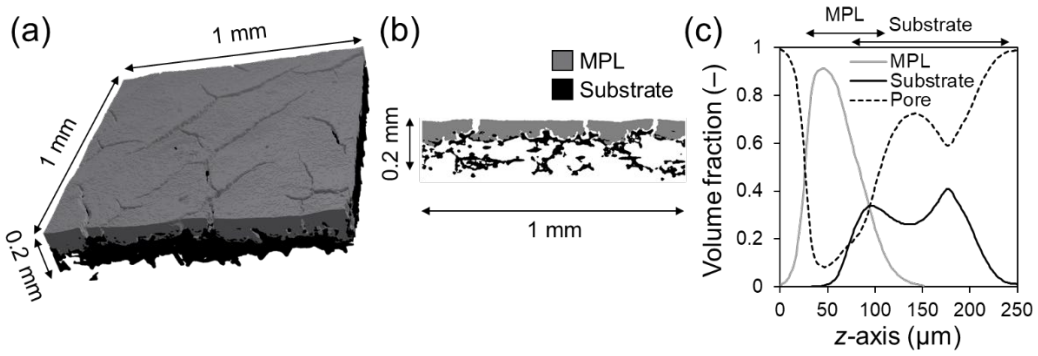

Figure 7.3 (a) Three-dimensional and (b) cross-sectional X-μCT images of a GDL. (c) Through-plane volume fractions of the MPL, substrate, and pore in the GDL. Copyright 2023, American Chemical Society.

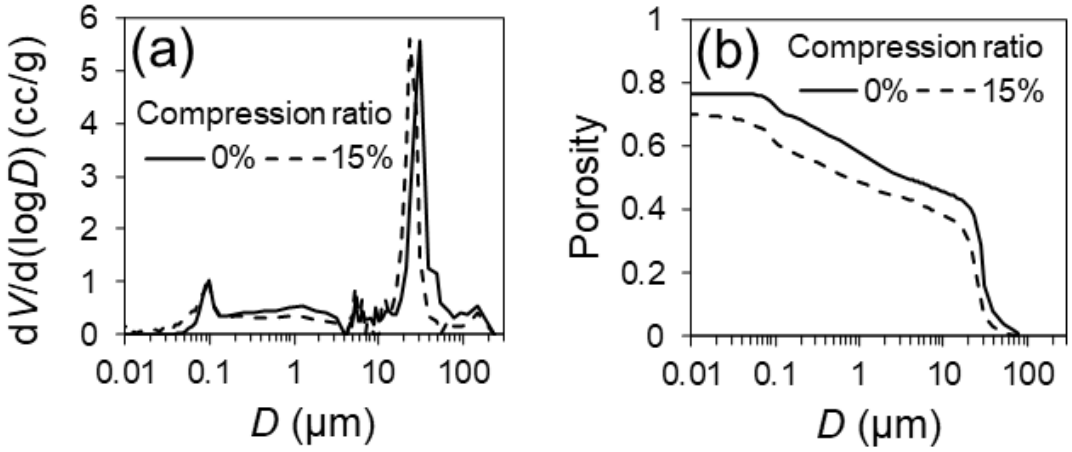

Figure 7.4 (a) Pore size distribution and (b) porosity of GDLs measured by mercury intrusion porosimetry. Pore diameter and volume are denoted as D and V, respectively. Copyright 2023, American Chemical Society.

7.3.2 Direct Measurements of Oxygen Transport Properties

The film resistance on the sample or inadequate gas mixing in the Wicke-Kallenbach type cell hinders the appropriate evaluation of gas diffusivity [22]. In Figure 7.5a, the effective diffusivity D_{eff} is plotted against the volumetric flow rate, with dashed lines representing the bulk diffusion coefficient D_{bulk} at 30 °C (2.11×10^{-5} m^2 s^{-1}) calculated using the Chapman-Enskog equation. The plot of dry D_{eff} shows no dependence on the volumetric flow rates, indicating homogeneous gas mixing and the absence of external transport limitations through a boundary layer above the GDL surface. This suggests that the film resistance on the sample or insufficient gas mixing in the measurement cell did not affect the evaluation of gas diffusivity. The influence of GDL thickness on dry D_{eff} was investigated by stacking multiple GDL sheets (Figure 7.5b). The error bars represent the standard deviation of experimental results for volumetric flow rates between 50 and 100 mL min^{-1}. As the number of GDL sheets increased, dry D_{eff} remained almost constant. This indicates that the GDLs mainly governed the oxygen transport resistance, and even two GDL sheets were sufficient to supply oxygen under the ribs of the flow field. Direct measurements revealed that dry D_{eff} at 30 °C was $(3.8 \pm 0.1)\times10^{-6}$ m^2 s^{-1}, corresponding to a gas diffusivity of 0.18 ± 0.01. The value of γ ($D_{eff} / D_{bulk} = \varepsilon^{\gamma}$), which is a parameter indicating gas diffusion performance related to the porosity (ε), was approximately 5 for the GDL in the through-plane direction, considering the measured porosity (0.71) and gas diffusivity (0.18). This value differs from previous studies, which reported $\gamma = 4$ for carbon paper and stand-alone MPL [3]. The pore structure of the MPL intrusion layer in GDLs likely influences the decrease in gas diffusion performance, which was not considered in the previous work.

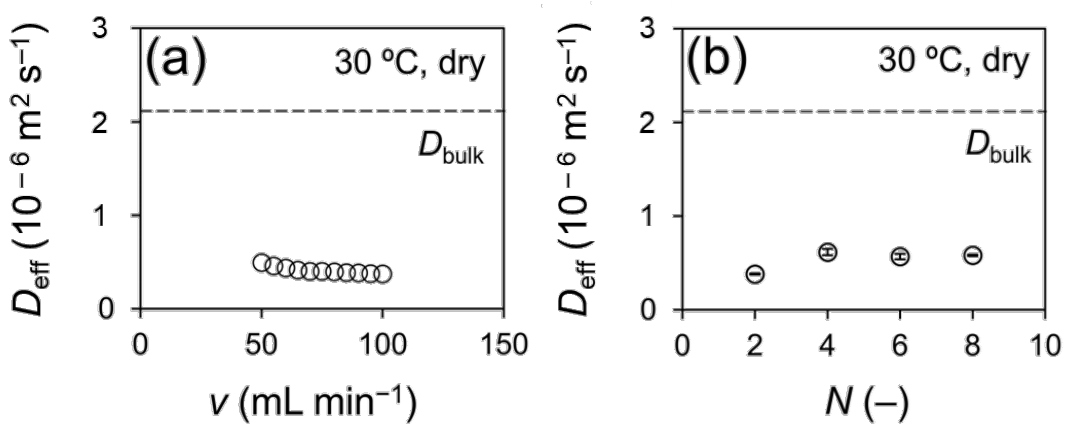

Figure 7.5 Dry D_{eff} as a plot of the (a) flow rate v and (b) number of GDL sheets N. The dashed lines represent D_{bulk} at 30 °C. The error bars in (b) are the standard deviation of measurements in 50–100 mL min^{-1}. Copyright 2023, American Chemical Society.

Figure 7.6a displays dry D_{eff} plotted as a function of cell temperature. As the cell temperature increased, dry D_{eff} also increased. However, the gas diffusivity, calculated from dry D_{eff}, remained almost constant, indicating that the structural parameters in the GDLs did not change with temperature. Figure 7.6b shows the RH dependence of wet D_{eff} at a cell temperature of 60 °C. As the RH increased, wet D_{eff} decreased and reached approximately 31 ± 1% of the dry D_{eff} at 100% RH. According to the Wilke equation, the bulk diffusion coefficient of oxygen in a nitrogen-vapor mixture is higher than that of nitrogen, suggesting that wet D_{eff} should increase in the presence of vapor. However, the experimental results did not align with this estimation. In order to explain this discrepancy, the effect of water condensation was considered based on the following equation [23]:

$$D_{\mathrm{eff(wet)}} = D_{\mathrm{eff(dry)}}(1 - S)^{\lambda}, \tag{7.8}$$

where S represents the water saturation level and λ is the empirical parameter. Assuming that the decrease in wet D_{eff} is solely attributed to water accumulation in the GDL, the water saturation level of approximately 0.45 ± 0.01 was estimated at 100% RH when λ was 2 for the through-plane direction [23]. The reduction in wet D_{eff} was observed even at 40% RH, corresponding to the water saturation level of 8 ± 4%, suggesting the presence of condensate that could not be completely prevented at a locally cooled position in the gas line, as vapor is unlikely to condense below the dew point inside the cell.

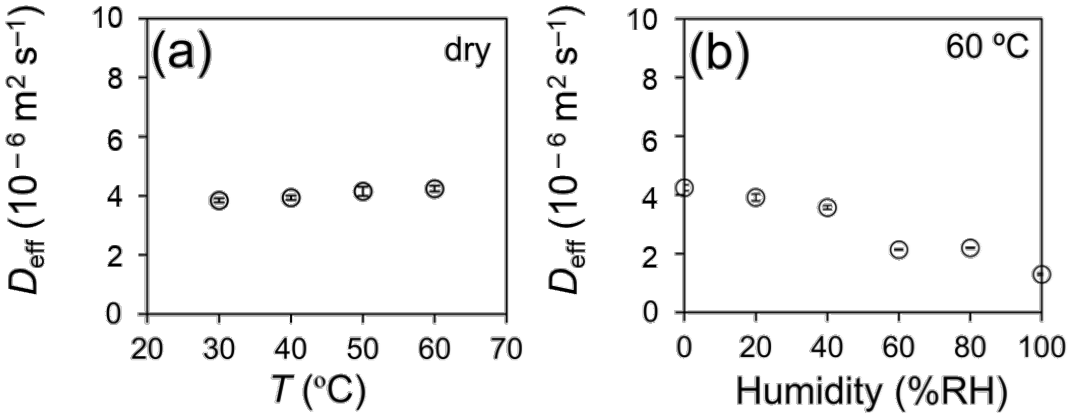

Figure 7.6 D_{eff} as a plot of the (a) cell temperature T and (b) relative humidity RH. Copyright 2023, American Chemical Society.

7.3.3 Limiting Current Measurements

Figure 7.7a presents polarization curves at 1% O_2 under different gas pressures, showing that the limiting currents vary with gas pressure. In Figure 7.7b, polarization curves are displayed for different numbers of GDL sheets. The limiting currents change with the number of GDL sheets, and these can be converted to total resistance R_T. The relationship between R_T and the number of GDL sheets is displayed in Figures 7.7d and 7.7e, where the dashed lines represent linear function fits to the data. The intercept with the vertical axis represents the resistance of the catalyst layer R_{CL}, and the slope of the line represents the resistance of the GDL sheet R_{GDL}. Figure 7.7f demonstrates the relationship between R_T and the RH sensitivity at a cell temperature of 60 °C. It is observed that an increase in R_T occurs below 60% RH. In Figure 7.7c, a significant voltage drop at low RH conditions is revealed, leading to an overestimation of R_T (Figure 7.7f). Two factors contribute to this voltage drop. First, there is an increase in proton transport resistance due to the drying of the electrolyte membrane. Second, there is an increase in the local oxygen transport resistance of the CL at low RH levels [24].

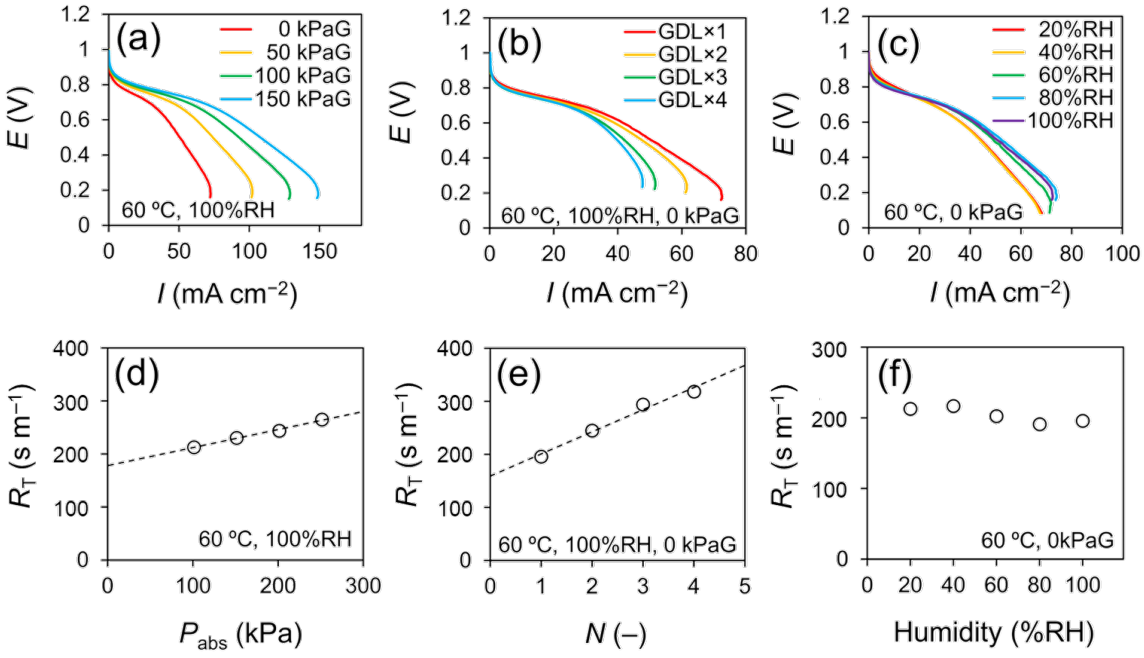

Figure 7.7 Polarization curves at 1% O_2 in N_2 as a function of (a) gauge pressure, (b) N, and (c) RH. Total gas transport resistance R_T as a plot of (d) absolute pressure P_{abs}, (e) N, and (f) RH. Copyright 2023, American Chemical Society.

7.3.4. Comparison of Measurement Methods

Figure 7.8 summarizes the results for R_{GDL} obtained from three different methods. The data presented in Figure 7.8a were obtained by varying the RH. The error bars in Figure 7.8a represent the standard deviation of the experimental results measured at different volumetric flow rates. As RH increases, R_{GDL} also increases at each temperature. This can be attributed to water accumulation in the GDL (Figure 7.9a). Additionally, the higher R_{GDL} at higher cell temperatures suggests the accumulation of vapor in the gas line, as discussed earlier. Figure 7.8b shows the relationship between R_{GDL} and gas pressure, obtained through limiting current measurements. An increase in R_{GDL} was observed at lower RH conditions (<60% RH). This increase was attributed to the insufficient proton conductivity resulting from voltage drops at lower RH levels. It is recommended to obtain limiting currents for a diluted oxygen concentration, such as 0.1% O_2, to avoid voltage drops. However, the measurement of such currents requires careful subtraction of H_2 crossover current, electric double-layer capacitance current, and experimental errors when preparing diluted oxygen gas. Figure 7.8c displays the dependence of R_{GDL} on GDL thickness. Stacking multiple GDL sheets introduces considerable oxygen transport resistance, leading to low limiting currents. The reduction gives the impact of voltage drops and enables accurate determination of R_{GDL} at low RH conditions. Conversely, an increase in R_{GDL} was observed at higher RH conditions, indicating the presence of accumulated water between the GDL sheets (Figure 7.9c). Due to the stacking of GDL sheets, capillary force is unable to drain liquid water effectively, and the lack of penetrating cracks limits drainage through MPL cracks observed in the X-μCT image.

A notable difference between Figure 7.8b and Figure 7.8c at higher RH conditions is the influence of cell temperature on R_{GDL}. In Figure 7.8b, larger R_{GDL} values were observed at lower cell temperatures, likely due to higher water saturation levels under the ribs of the flow field (Figure 7.9b). The GDL under cold ribs exhibited higher liquid water saturation at low temperatures, hindering oxygen diffusion and resulting in increased R_{GDL}. However, when GDLs were stacked in the cell (Figure 7.8c), R_{GDL} was less influenced by cell temperature. The thick GDL layer facilitated uniform gas supply to the CL, even if liquid water accumulated under cold ribs (Figure 7.9c). Moreover, the thermal conductivity of GDLs is significantly lower than that of flow fields, limiting the impact of temperature on water condensation away from ribs.

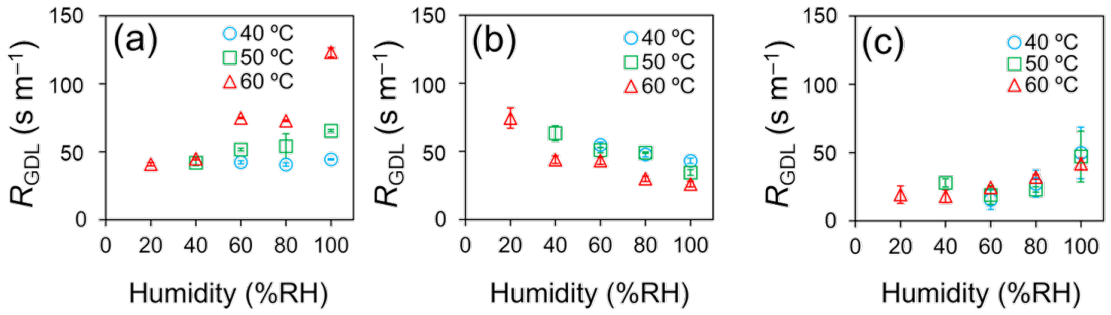

Figure 7.8 R_{GDL} determined by (a) the direct measurement method using the Wicke-Kallenbach type diffusion cell; the limiting current method from the relationship with (b) absolute pressures and (c) GDL thicknesses. Copyright 2023, American Chemical Society.

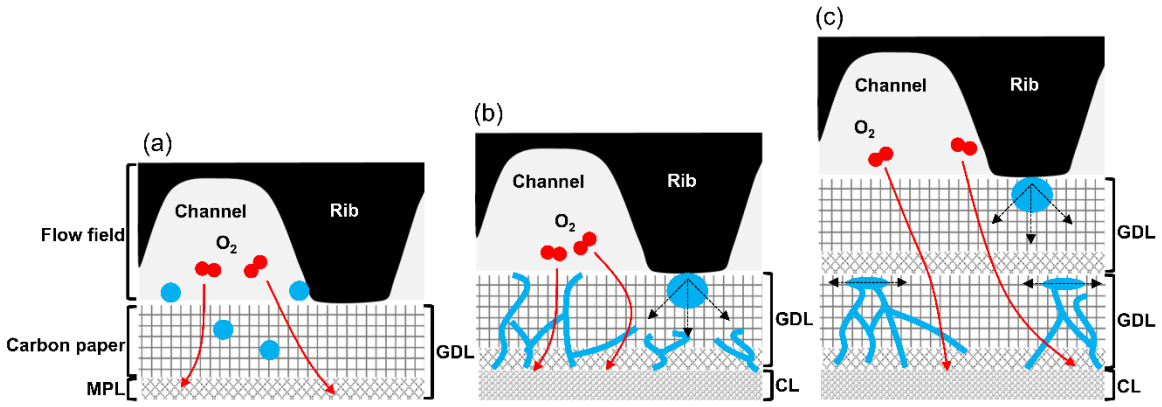

Figure 7.9 Schematic views of the inside of the evaluation cells: (a) the direct measurement approach using the Wicke-Kallenbach type diffusion cell and the electrochemical approach varying the (b) absolute pressures and (c) GDL thicknesses. Copyright 2023, American Chemical Society.

7.4 Conclusion

This chapter demonstrated the impact of evaluation methods on the oxygen transport properties of partially saturated GDLs in PEFCs. Three different approaches were used to measure gas transport properties: direct measurements using a Wicke-Kallenbach type cell, electrochemical measurements using a fuel cell setup to measure limiting currents at various pressures and GDL thicknesses, and pressure control (GDL stack) method. The direct measurements show that the effective diffusion coefficient of oxygen in the dry GDL is constant at cell temperature and decreases with increasing RH. In the electrochemical approaches, the pressure control (GDL stack) method resulted in an overestimated oxygen transport resistance compared to the low (high) RH conditions. This overestimation was attributed to voltage drops caused by dried electrolyte membrane and water accumulation between the GDLs in the respective conditions. It was concluded that the direct measurement method provides an advantage in evaluating the diffusivity of partially wet GDLs without the influence of other components. However, it cannot account for the impact of water produced at the PEFC electrode. Electrochemical measurements allow for the examination of the effect of produced water on gas transport resistance. The pressure control (GDL stack) method offers reasonable gas transport resistance under high (low) RH conditions. The findings from this study contribute to the development of GDL materials for controlling liquid water in PEFCs, which is crucial for improving the performance and durability of fuel cells.

References

01. J. M. LaManna, S. G. Kandlikar, Determination of Effective Water Vapor Diffusion Coefficient in PEMFC Gas Diffusion Layers, Int. J. Hydrog. Energy 36 (2011) 5021–5029.
02. P. Mangal, L. M. Pant, N. Carrigy, M. Dumontier, V. Zingan, S. Mitra, M. Secanell, Experimental Study of Mass Transport in PEMFCs: Through Plane Permeability and Molecular Diffusivity in GDLs, Electrochim. Acta 167 (2015) 160–171.
03. G. Inoue, K. Yokoyama, J. Ooyama, T. Terao, T. Tokunaga, N. Kubo, M. Kawase, Theoretical Examination of Effective Oxygen Diffusion Coefficient and Electrical Conductivity of Polymer Electrolyte Fuel Cell Porous Components, J. Power Sources 327 (2016) 610–621.
04. N. Zamel, N. G. Astrath, X. Li, J. Shen, J. Zhou, F. B. Astrath, H. Wang, Z. S. Liu, Experimental Measurements of Effective Diffusion Coefficient of Oxygen–Nitrogen Mixture in PEM Fuel Cell Diffusion Media, Chem. Eng. Sci. 65 (2010) 931–937.
05. C. Chan, N. Zamel, X. Li, J. Shen, Experimental Measurement of Effective Diffusion Coefficient of Gas Diffusion Layer/Microporous Layer in PEM Fuel Cells, Electrochim. Acta 65 (2012) 13–21.
06. Y. Utaka, Y. Tasaki, S. Wang, T. Ishiji, S. Uchikoshi, Method of Measuring Oxygen Diffusivity in Microporous Media, Int. J. Heat Mass Transfer 52 (2009) 3685–3692.
07. R. Koresawa, Y. Utaka, Precise Measurement of Effective Oxygen Diffusivity for Microporous Media Containing Moisture by Review of Galvanic Cell Oxygen Absorber Configuration, Int. J. Heat Mass Transfer 76 (2014) 549–558.
08. R. Rashapov, F. Imami, J. T. Gostick, A Method for Measuring In-Plane Effective Diffusivity in Thin Porous Media, Int. J. Heat Mass Transfer 85 (2015) 367–374.
09. T. G. Tranter, P. Stogornyuk, J. T. Gostick, A. Burns, W. F. Gale, A Method for Measuring Relative In-Plane Diffusivity of Thin and Partially Saturated Porous Media: An Application to Fuel Cell Gas Diffusion Layers, Int. J. Heat Mass Transfer 110 (2017) 132–141.
10. W. Yoshimune, S. Kato, S. Yamaguchi, Multi-Scale Pore Morphologies of a Compressed Gas Diffusion Layer for Polymer Electrolyte Fuel Cells, Int. J. Heat Mass Transfer 152 (2020) 119537.
11. W. Yoshimune, S. Kato, S. Yamaguchi, Y. Akimoto, A. Koiwai, H. Nakamura, Managing the Pore Morphologies of Microporous Layers for Polymer Electrolyte Fuel Cells with a Solvent-Free Coating Technique, ACS Sustain. Chem. Eng. 9 (2021) 7922–7929.
12. A. Chowdhury, A. Bird, J. Liu, I. V. Zenyuk, A. Kusoglu, C. J. Radke, A. Z. Weber, Linking Perfluorosulfonic Acid Ionomer Chemistry and High-Current Density Performance in Fuel-Cell Electrodes, ACS Appl. Mater. Interfaces 13 (2021) 42579–42589.
13. W. Yoshimune, S. Kato, M. Inagaki, S. Yamaguchi, A Simple Method to Measure Through-Plane Effective Gas Diffusivity of a Gas Diffusion Layer for Polymer Electrolyte Fuel Cells, Int. J. Heat Mass Transfer 191 (2022) 122887.
14. M. Inagaki, W. Yoshimune, S. Kato, Computer-Aided Determination of the Effective Diffusion Coefficient of a Gas Diffusion Layer for Polymer Electrolyte Fuel Cells, J. Chem. Eng. Adv. 14

(2023) 100479.

15. K. Uesugi, M. Hoshino, A. Takeuchi, Y. Suzuki, N. Yagi, T. Nakano, Development of Fast (Sub-Minute) Micro-Tomography, AIP Conf. Proc. 1266 (2010) 47–50.
16. Schneider, C. A.; Rasband, W. S.; Eliceiri, K. W. NIH Image to ImageJ: 25 Years of Image Analysis, Nat. Methods 9 (2012) 671–675.
17. GeoDict-The Digital Material Laboratory. https://www.geodict.com/ (accessed 2023-10-25).
18. K. N. Kim, J. H. Kang, S. G. Lee, J. H. Nam, C.-J. Kim, Lattice Boltzmann Simulation of Liquid Water Transport in Microporous and Gas Diffusion Layers of Polymer Electrolyte Membrane Fuel Cells, J. Power Sources 278 (2015) 703–717.
19. J. Lee, R. Banerjee, M. G. George, D. Muirhead, P. Shrestha, H. Liu, N. Ge, S. Chevalier, A. Bazylak, Multiwall Carbon Nanotube-Based Microporous Layers for Polymer Electrolyte Membrane Fuel Cells, J. Electrochem. Soc. 164 (2017) F1149–F1157.
20. A. K. C. Wong, R. Banerjee, A. Bazylak, Tuning MPL Intrusion to Increase Oxygen Transport in Dry and Partially Saturated Polymer Electrolyte Membrane Fuel Cell Gas Diffusion Layers, J. Electrochem. Soc. 166 (2019) F3009–F3019.
21. J. Lee, H. Liu, M. G. George, R. Banerjee, N. Ge, S. Chevalier, T. Kotaka, Y. Tabuchi, A. Bazylak, Microporous Layer to Carbon Fibre Substrate Interface Impact on Polymer Electrolyte Membrane Fuel Cell Performance, J. Power Sources 422 (2019) 113–121.
22. S. Kato, H. Ozeki, H. Yamada, T. Tagawa, N. Takahashi, H. Shinjoh, Direct Measurements of Gas Diffusivity in a Washcoat Layer under Steady State Conditions at Ambient Temperature. J. Ind. Eng. Chem. 19 (2013) 835–840.
23. H. Xu, M. Bührer, F. Marone, T. J. Schmidt, F. N. Büchi, J. Eller, Effects of Gas Diffusion Layer Substrates on PEFC Water Management: Part I. Operando Liquid Water Saturation and Gas Diffusion Properties. J. Electrochem. Soc. 168 (2021) 074505.
24. K. Kudo, R. Jinnouchi, Y. Morimoto, Humidity and Temperature Dependences of Oxygen Transport Resistance of Nafion Thin Film on Platinum Electrode, Electrochim. Acta 209 (2016) 682–690.

Chapter 8

A New Solvent-Free Coating Process for MPLs

8.1 Introduction

Commercial battery electrodes are manufactured by a wet-coating process using a slurry. The slurry is prepared by blending electrode materials with additives such as the solvent, dispersing, and thickener. These additives must be safely eliminated during drying, requiring additional electrical energy. In order to address these challenges, a direct deposition method using an electrode powder is employed, eliminating expensive and environmentally unfriendly processes. Currently, dry-coating techniques have been explored for the production of lithium-ion batteries [1–6], all-solid-state lithium-ion batteries [7,8], and PEFCs [9–12]. In this chapter, the author has introduced a solvent-free coating approach using an electrostatic screen printer to fabricate MPLs for PEFCs.

8.2 Experimental

8.2.1 Fabrication Process for Dry-Coated MPLs

The fabrication process is divided into four steps (Figure 8.1): (a) particle composition process for MPL powder, (b) powder deposition process using an electrostatic screen printer, (c) consolidation process, and (d) annealing process. In this study, graphite (GP, KS4, TIMCAL), acetylene black (AB, HS−100, DENKA), and polytetrafluoroethylene (PTFE, KTL−500F, KITAMURA) were used to prepare the MPL powder. The primary particle diameters for GP, AB, and PTFE were 2.4 μm, 40 nm, and 500 nm, respectively.

Before the composition process, GP and AB were premixed with PTFE for 3 minutes using a double-blade mill. The standard PTFE content was 20 wt%. The mixtures were then composited using a multipurpose compact mixing grinder (MP5, Nippon Coke & Engineering) with a rotation speed of 10,000 rpm for 30 minutes. The resulting composite powder samples were named CP_{GP} and CP_{AB}. It should be noted that previously reported methods [1–12] were not applicable due to the highly cohesive particle properties. The screen-printing method effectively crushes the agglomerates during the deposition process. The composite powder was directly deposited onto commercial carbon paper treated with PTFE (Sigracet 29BA, SGL Carbon) using an electrostatic screen printer (TS-1, BERG). The deposition was followed by compression at a pressure of 1 MPa and annealing at 350 °C for 30 minutes. It is worth noting that a hot-pressing process was not employed due to the pore-blocking effect of melted PTFE, which reduces porosity. Therefore, the pressing and annealing processes needed to be separated at the dry-coating technique for MPLs. The coating area used for MPL preparation was typically 50 × 50 mm^2 (The maximum coating area: 180 × 300 mm^2). Here, the author prepared four-type MPLs with two different particles (CP_{GP} and CP_{AB}) to control the pore morphologies in MPLs. Table 8.1 summarizes sample specifications.

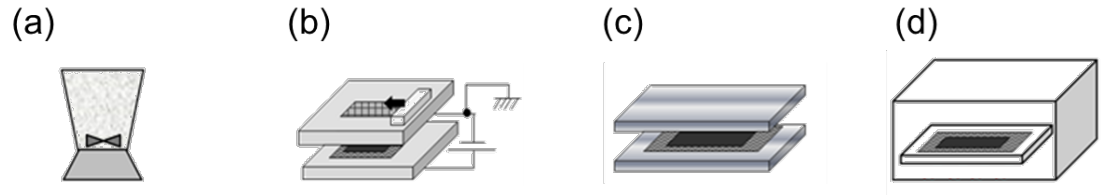

Figure 8.1 Schematic diagram of the dry-coating process for MPLs: (a) composition, (b) screen-printing, (c) consolidation, and (d) annealing. Copyright 2021, American Chemical Society.

Table 8.1 Sample specifications

MPL type	Particle configuration
MPL-**S**	CP_{AB}
MPL-**B**	CP_{GP}
MPL-**M**[a]	(CP_{AB} + CP_{GP})
MPL-**G**[b]	CP_{AB} (2nd layer) / CP_{GP} (1st layer)

[a]A mixture layer of CP_{AB} and CP_{GP} in a 1:1 ratio by volume.

[b]Multiple MPL layers forming a porosity-graded structure.

8.2.2 Preparation of CCMs

Commercial Pt nanoparticle supported on carbon (TEC10E50E, Tanaka Kikinzoku Kogyo), Nafion dispersion (D2020, Chemours), and Nafion electrolyte membrane (NR211, Chemours) were used for CCMs. A catalyst ink of TEC10E50E and D2020 dispersed in a mixture of ethanol and deionized water (v/v:3/7), was applied onto a decal PTFE sheet using an applicator. The weight ratio of the Nafion ionomer to the carbon supports was 0.75. The applicator gap controlled the coating thickness to achieve a platinum loading of 0.3 $mg_{Pt}\,cm^{-2}$. Subsequently, the catalyst layer was subjected to hot-pressing at 125 °C for 10 minutes on both sides of the NR211 membrane.

8.2.3 Characterization Method of Structure and Properties for Dry-Coated MPLs

MPL surfaces were analyzed for their microscopic characteristics using field-emission scanning electron microscopy (FE-SEM, Regulus SU8230, Hitachi High Technologies) in the secondary electron mode at an accelerated voltage of 2 kV. The cross sections of the resin-filled and machine-polished GDL samples were observed using an optical microscopy (Eclipse LV150, Nikon) with bright-field optical modes.

The hydrophobicity of MPLs was assessed by measuring the contact angles using a contact angle meter (DMo-501, KYOWA). Each MPL sample was evaluated at five different locations, and the average values were calculated. Deionized water droplets (7 μL) were used for each measurement.

The pore size distribution of MPLs was investigated using mercury intrusion porosimetry (MIP, PoreMaster 60GT, Quantachrome Instruments). To study the porosity and peak pore diameters of the micropores within GDLs, synchrotron X-μCT was performed at Toyota beamline (BL33XU) in SPring-8 facility [13]. However, due to the limited spatial resolution of synchrotron X-μCT, submicron pore

morphologies within MPLs could not be analyzed. In order to overcome this limitation, a synchrotron X-nCT system with a spatial resolution of 68 nm was recently incorporated at the BL33XU beamline [14]. MPL specimens measuring approximately 50 × 50 × 50 μm³ were prepared for X-nCT measurements. The X-nCT involved capturing 1800 projections using an X-ray energy of 8 keV with a field of view of 71.4 μmφ. Tomographic reconstruction was performed using a software package provided by JASRI [15]. The segmentation of computed tomography images was conducted using Fiji software (ImageJ) [16]. The segmented computed tomography images were analyzed to study the pore morphologies using Geodict software (Math2Market GmbH) [17].

Electrochemical characterization was performed using a 1 cm^2 single cell to investigate the effect of pore morphologies on the fuel cell performance at a wet condition. In this cell, the fabricated CCM and GDLs were compressed. The compression ratio of the GDLs was 20 ± 5% by controlling the gasket thickness, based on their initial thickness. As for the anode GDL, a commercial GDL with MPL (Sigracet 29BC, SGL Carbon) was used. The single cell had straight channels with widths of 0.4 mm for the channels and 0.2 mm for the ribs. The cathode and anode flow fields were configured in a cross-flow manner. The break-in and polarization tests were conducted under specific conditions. A constant flow of air/H_2 (2000/500 sccm) was maintained at a backpressure of 50 kPa for the cathode and anode sides. The break-in test involved sweeping the cell voltage between 0 and 1.0 V for 50 cycles at a scan rate of 10 mV s^{-1}, with the temperature set at 80 °C and the RH at 100%. Potential cycling was performed in the range of 0.05 to 0.95 V at a scan rate of 50 mV s^{-1} for five cycles under a 10% H_2 atmosphere at the anode electrode. During potential cycling, the gas supply on the cathode side was discontinued. The charge associated with the underpotential adsorption of hydrogen was determined from the hydrogen adsorption current observed between 0.05 V (inflection point) and 0.4 V (double layer region) by recording five cycles of the cyclic voltammogram. The electrochemical active surface area (ECSA) was calculated based on the charge assumption of 210 μC cm_{Pt}^{-1} and then converted to the roughness factor (RF) in cm_{Pt}^2 cm_{geo}^{-2} to compare the quality of CCMs. Polarization curves were recorded at 51.2 °C under condensation conditions with 120% RH (i.e., condensing). The cell voltage was swept between 0 and 1.0 V at a scan rate of 10 mV s^{-1}. In order to account for Ohmic overpotential, all polarization curves were corrected by simultaneously measuring high-frequency resistances using an AC resistance meter (356E, TSURUGA) at 10 kHz.

8.3 Results and Discussion

8.3.1 Morphologies and Properties of Dry-Coated MPLs

Figure 8.2 displays SEM images of MPL surfaces. In Figure 8.2a–d, the carbon fiber substrate was covered with a powdery layer, and no cracks were observed on their surfaces. The absence of cracks can be attributed to the elimination of a drying process in the solvent-free coating process, as cracks typically form during drying in wet-coating methods [13]. The lower row of SEM images in Figure 8.2 shows microstructures of MPL surfaces. MPL-**S** and MPL-**G** had CP_{AB} on their surface, while MPL-**B** had CP_{GP}. MPL-**M** exhibited a mixture of CP_{GP} and CP_{AB} on the surface. Figure 8.3 shows cross-sectional optical microscopy images of MPLs, where the fibrous bottom layers (carbon paper) and the powdery upper layers (MPLs) are visible. The MPL thickness ranged from 50 to 75 μm. MPL-**S** and MPL-**B** had uniform MPLs, while MPL-**M** had a nonuniform powdery layer due to the direct deposition of a mixture of CP_{GP} and CP_{AB}. MPL-**G** consisted of separated CP_{GP} and CP_{AB} powdery layers, referred to as the 1st MPL and 2nd MPL, respectively.

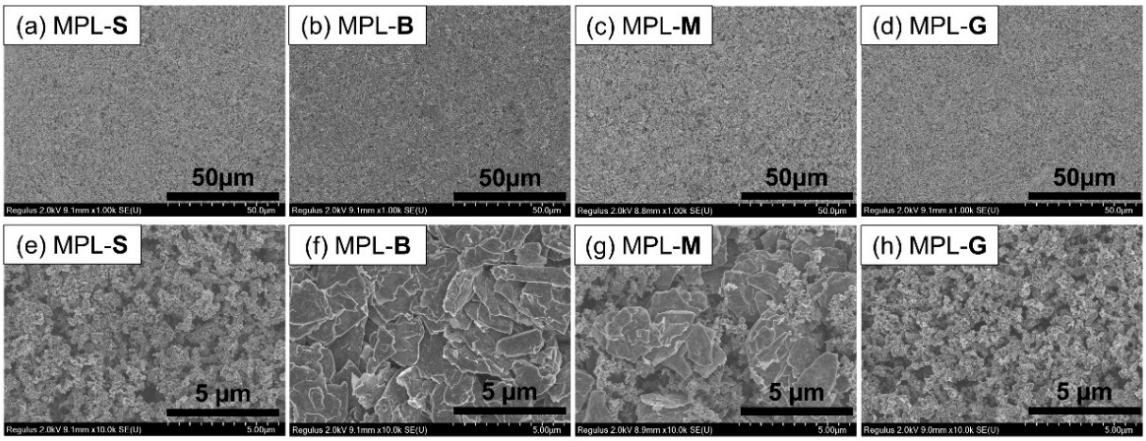

Figure 8.2 Surface SEM images of dry-coated MPLs: (a, e) MPL-**S**, (b, f) MPL-**B**, (c, g) MPL-**M**, and (d, h) MPL-**G**. The images in the upper and lower rows were obtained at 1000× and 10,000× magnification, respectively. Copyright 2021, American Chemical Society.

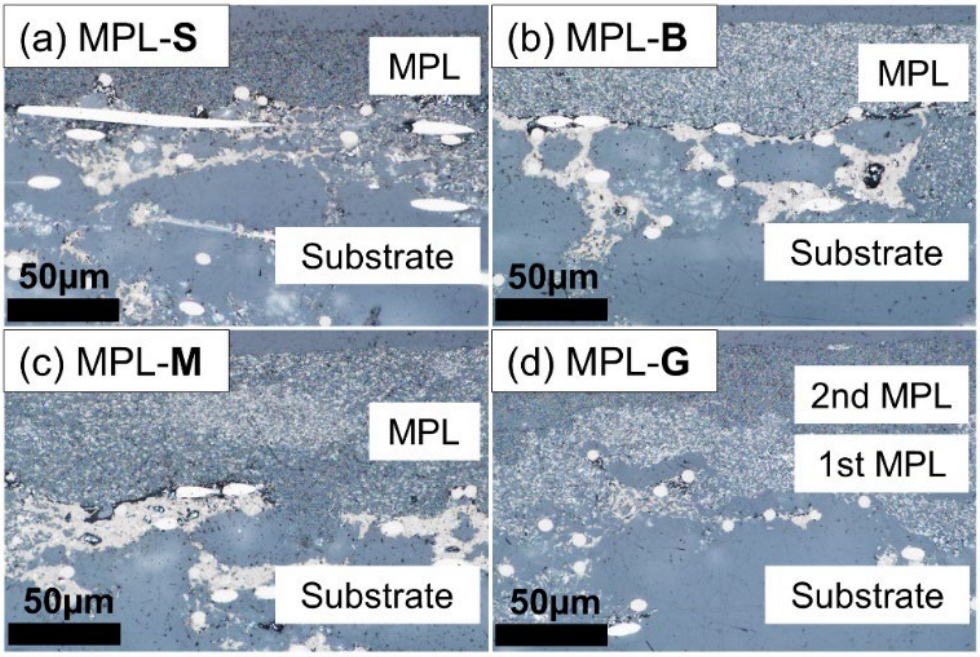

Figure 8.3 Cross-sectional optical microscope images of dry-coated MPLs: (a) MPL-**S**, (b) MPL-**B**, (c) MPL-**M**, and (d) MPL-**G**. Copyright 2021, American Chemical Society.

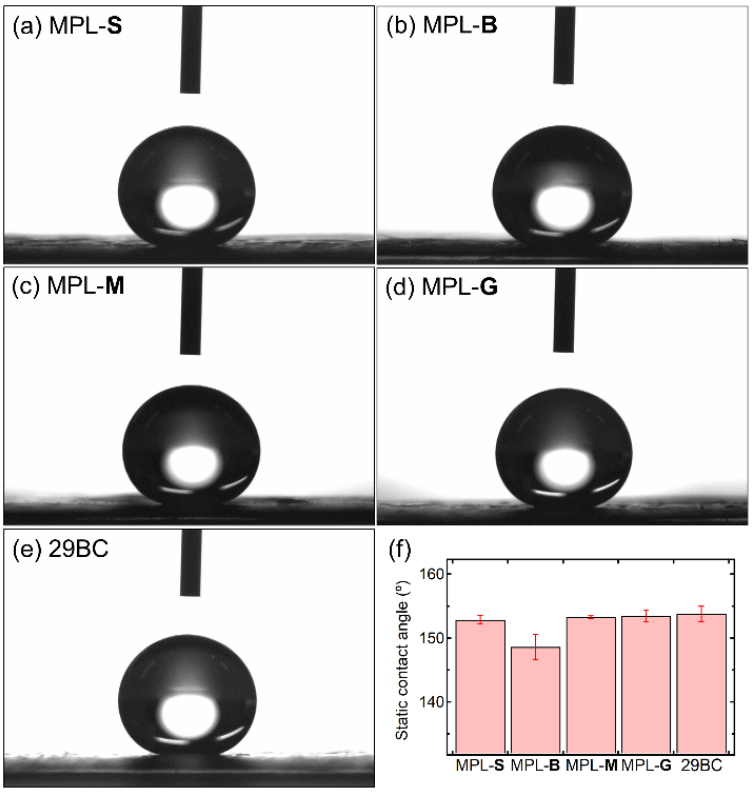

Figure 8.4 Static water contact angles of MPLs: (a) MPL-**S**, (b) MPL-**B**, (c) MPL-**M**, (d) MPL-**G**, and (e) commercial GDL (Sigracet 29BC); (f) graphical comparison of the average contact angles of (a–e). Copyright 2021, American Chemical Society.

The hydrophobicity of MPLs plays a role in mass transport within GDLs and affects flooding during high-current-density operation. Contact angle measurements were performed to evaluate the wettability of MPLs (Figure 8.4). The average contact angles of MPL-**S**, MPL-**B**, MPL-**M**, MPL-**G**, and a commercial GDL (Sigracet 29BC) were 153, 149, 153, 153, and 154°, respectively. All of the prepared MPLs exhibited hydrophobicity comparable to that of the commercial GDL. MPL-**B** exhibited a smaller contact angle compared to the others, likely due to the exposed CP_{GP} layer with a high surface roughness.

The pore size distributions of MPLs are shown in Figure 8.5. MPL-**S** and MPL-**B** exhibited micropores with peak pore diameters of 0.17 and 0.41 μm, respectively. MPL-**M** displayed micropores with a peak pore diameter of 0.26 μm. MPL-**G** exhibited characteristics of both MPL-**S** and MPL-**B**. All of the dry-coated MPLs displayed a broad peak in the range of 0.5 to 4 μm. Figure 8.6 presents reconstructed 3D X-nCT images for MPLs. The images revealed the arrangement and distribution of CP_{GP} and CP_{AB} within each MPL type. In MPL-**S** and MPL-**B**, CP_{GP} and CP_{AB} differed in terms of their sizes and were randomly scattered throughout the MPL. MPL-**M**, on the other hand, exhibited a mixed arrangement of CP_{GP} and CP_{AB}. In MPL-**G**, CP_{GP} and CP_{AB} were regularly arranged to form the 1st and 2nd MPLs. The pore properties for each MPL type are provided in Table 8.2.

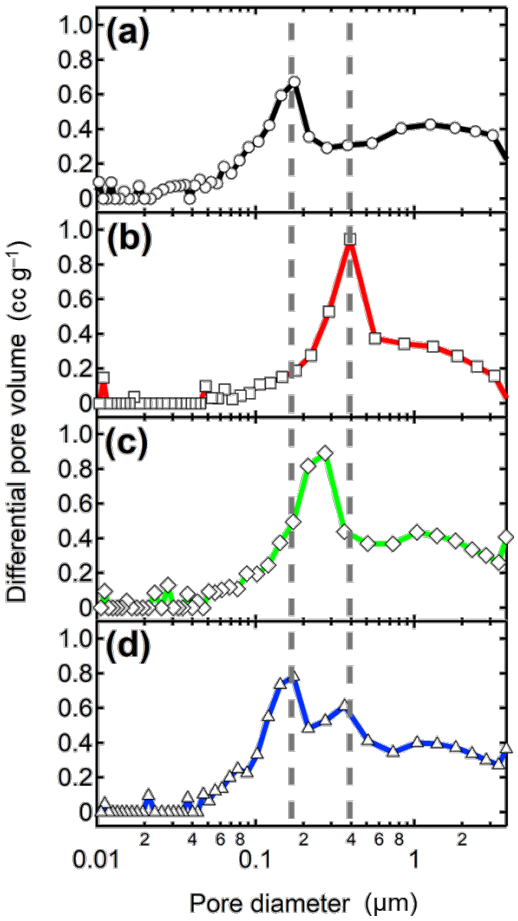

Figure 8.5 Pore size distribution of dry-coated MPLs: (a) MPL-**S**, (b) MPL-**B**, (c) MPL-**M**, and (d) MPL-**G**. Copyright 2021, American Chemical Society.

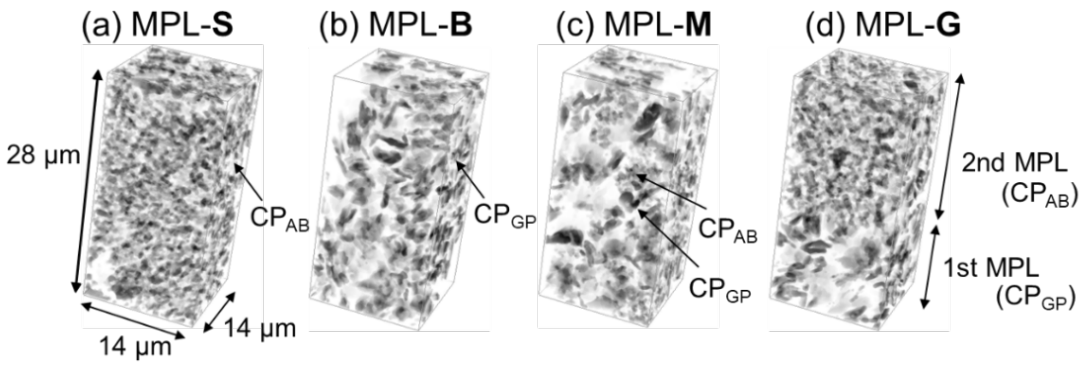

Figure 8.6 Synchrotron X-nCT images of dry-coated MPLs: (a) MPL-**S**, (b) MPL-**B**, (c) MPL-**M**, and (d) MPL-**G**. Black and white areas represent the composite powder (CP_{GP} and CP_{AB}) and pores, respectively. Copyright 2021, American Chemical Society.

Table 8.2 Pore properties of dry-coated MPLs.

MPL type	Pore diameter[a] (μm)	Porosity[b] (–)
MPL-**S**	0.17 ± 0.02	0.66 ± 0.01
MPL-**B**	0.41 ± 0.06	0.71 ± 0.02
MPL-**M**	0.26 ± 0.04	0.73 ± 0.01
MPL-**G** (1st MPL)	0.35 ± 0.06	0.68 ± 0.01
MPL-**G** (2nd MPL)	0.17 ± 0.03	0.67 ± 0.02

[a]Peak pore diameter measured by mercury intrusion porosimetry.

[b]Calculated values for three arbitrary regions (14 × 14 × 28 μm^3) from synchrotron X-nCT.

8.3.2 Electrochemical Characterization of Dry-Coated MPLs

The single-cell performance of MPLs was evaluated to investigate the effect of pore properties on the fuel cell performance. Figure 8.7a shows the cyclic voltammograms of MPLs at 80% RH. All the samples exhibited typical shapes observed for platinum catalysts, with hydrogen adsorption/desorption peaks in the range of 0.05–0.4 V and oxide formation/reduction peaks above 0.5 V. The cyclic voltammograms of the different MPLs overlapped with each other. The RFs were determined to be 140 ± 4 cm_{Pt}^2 cm_{geo}^{-2}, that is, within 5% of platinum loading in the CCMs. Figure 8.7b presents the polarization curves at 51.2 °C and 120% RH (i.e., condensing) to investigate the flooding tolerance. In the low-current region (<0.1 A cm^{-2}), the polarization curves overlapped, indicating comparable performance and activity of the cathode catalyst layers. The trend observed in the higher current region (> 1 A cm^{-2}) was as follows: MPL-**G** > MPL-**S** > MPL-**M** > commercial GDL (Sigracet 29BC) > MPL-**B**. This suggests that dry-coated MPLs exhibited comparable or higher performance than the commercial GDL.

MPL-**B** and MPL-**M**, which had exposed CP_{GP} on their surfaces, showed lower electrochemical performance compared to MPL-**S** and MPL-**G**, which had exposed CP_{AB}. The lower performance of MPL-**B** and MPL-**M** could be attributed to microscale gaps formed at the interface between the MPL

and CCM due to the presence of large particles on the surface. These gaps can lead to the accumulation of liquid water during operation under wet conditions, resulting in a sudden voltage drop. MPL-**S** exhibited higher flooding tolerance than the commercial MPL. The wet-coated commercial MPLs typically have porosities in the range of 0.4–0.6, while MPL-**S** had a porosity of approximately 0.7, despite having the same material content. The higher porosity of MPL-**S** allows for more water accumulation within its pores, contributing to its enhanced flooding tolerance. Another possible reason for the higher flooding tolerance of MPL-**S** is the difference in pore connectivity compared to the commercial MPL. MPL-**G**, which consisted of the 1st and 2nd MPLs with pore-size gradients, experienced internal capillary forces due to the interfaces between the layers, resulting in improved flooding tolerance. This comprehensive study suggests that multilayered MPLs with porosity gradients could be more favorable for enhancing fuel cell performance under wet conditions due to the occurrence of capillary forces at interfaces.

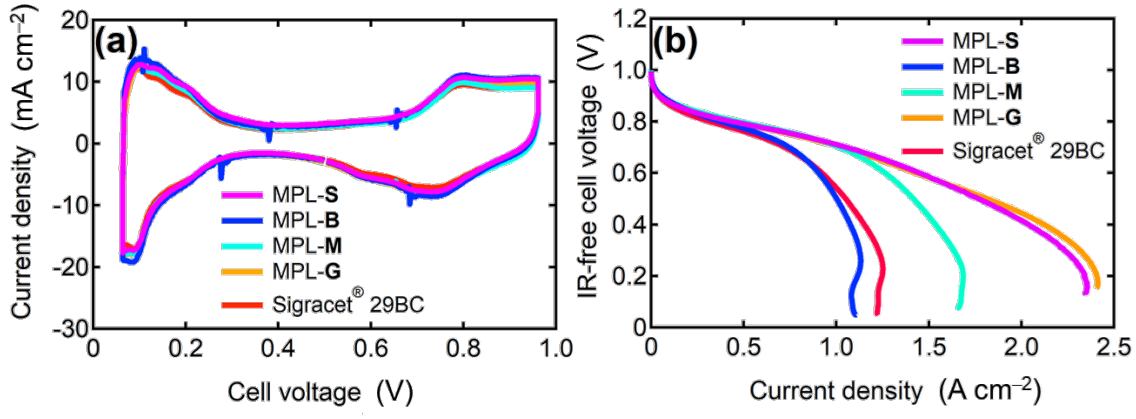

Figure 8.7 (a) Cyclic voltammograms at 80% RH for a single cell with different MPLs, recorded at a scan rate of 50 mV s^{-1}. (b) Polarization curves for MPLs. The fuel cell test was conducted at 51.2 °C and 120% RH (i.e., condensing) under the backpressure of 50 kPa for the cathode and anode sides. Copyright 2021, American Chemical Society.

8.4 Conclusion

In this chapter, the author introduced a novel solvent-free coating method for the production of MPLs in PEFCs using an electrostatic screen printer. The key advantage of this dry-coating process is the elimination of the expensive and environmentally unfavorable drying process. The author demonstrated the ability of the dry-coating process to control the pore morphologies of MPLs through the manipulation of particle arrangement. The particle and pore structures of dry-coated MPLs were comprehensively analyzed using microscopic observation, mercury intrusion porosimetry, and synchrotron X-nCT. Electrochemical characterization revealed that MPLs with a porosity gradient across their structure exhibited excellent resistance to flooding under wet conditions, which can be attributed to the capillary force within the MPLs.

References

01. D.-W. Park, N. A. Cañas, N. Wagner, K. A. Friedrich, Novel Solvent-Free Direct Coating Process for Battery Electrodes and Their Electrochemical Performance, J. Power Sources 306 (2016) 758–763.
02. B. Ludwig, Z. Zheng, W. Shou, Y. Wang, H. Pan, Solvent-Free Manufacturing of Electrodes for Lithium-Ion Batteries, Sci. Rep. 6 (2016) 23150.
03. B. Ludwig, J. Liu, I. M. Chen, Y. Liu, W. Shou, Y. Wang, H. Pan, Understanding Interfacial-Energy-Driven Dry Powder Mixing for Solvent-Free Additive Manufacturing of Li-Ion Battery Electrodes, Adv. Mater. Interfaces 4 (2017) 1700570.
04. M. Al-Shroofy, Q. Zhang, J. Xu, T. Chen, A. P. Kaur, Y.-T. Cheng, Solvent-Free Dry Powder Coating Process for Low-Cost Manufacturing of $LiNi_{1/3}Mn_{1/3}Co_{1/3}O_2$ Cathodes in Lithium-Ion Batteries, J. Power Sources 352 (2017) 187–193.
05. J. Liu, B. Ludwig, Y. Liu, H. Pan, Y. Wang, Strengthening the Electrodes for Li-Ion Batteries with a Porous Adhesive Interlayer through Dry-Spraying Manufacturing, ACS Appl. Mater. Interfaces 11 (2019) 25081–25089.
06. S. El Khakani, N. Verdier, D. Lepage, A. Prébé, D. Aymé-Perrot, D. Rochefort, M. Dollé, Melt-Processed Electrode for Lithium Ion Battery, J. Power Sources 454 (2020) 227884.
07. F. Hippauf, B. Schumm, S. Doerfler, H. Althues, S. Fujiki, T. Shiratsuchi, T. Tsujimura, Y. Aihara, S. Kaskel, Overcoming Binder Limitations of Sheet-Type Solid-State Cathodes using a Solvent-Free Dry-Film Approach, Energy Storage Mater. 21 (2019) 390–398.
08. C. Simon, D. Kartouzian, D. Muller, F. Wilhelm, H. A. Gasteigera, Enhancing the Lithium Ion Conductivity of an All Solid-State Electrolyte via Dry and Solvent-Free Scalable Series Production Processes, J. Electrochem. Soc. 167 (2020) F1697–F1711.
09. E. Gülzow, M. Schulze, N. Wagner, T. Kaz, R. Reissner, G. Steinhilber, A. Schneider, Dry Layer Preparation and Characterisation of Polymer Electrolyte Fuel Cell Components, J. Power Sources 86 (2000) 352–362.
10. K. Talukdar, S. Helmly, M. Schulze, D. G. Sanchez, M. Handl, R. Hiesgen, J. Kraut, K. A. Friedrich, Enveloping of Catalyst Powder by Ionomer for Dry Spray Coating in Polymer Electrolyte Membrane Fuel Cells, J. Power Sources 424 (2019) 82–90.
11. J. Yu, Y. Yoshikawa, T. Matsuura, M. N. Islam, M. Hori, Preparing Gas-Diffusion Layers of PEMFCs with a Dry Deposition Technique, Electrochem. Solid-State Lett. 8 (2005) A152–A323.
12. J. Chen, H. Xu, H. Zhang, B. Yi, Facilitating Mass Transport in Gas Diffusion Layer of PEMFC by Fabricating Micro-Porous Layer with Dry Layer Preparation, J. Power Sources 182 (2008) 531–539.
13. W. Yoshimune, S. Kato, S. Yamaguchi, Multi-Scale Pore Morphologies of a Compressed Gas Diffusion Layer for Polymer Electrolyte Fuel Cells, Int. J. Heat Mass Transfer 152 (2020) 119537.

14. S. Yamaguchi, S. Kato, W. Yoshimune, D. Setoyama, A. Kato, Y. Nagai, T. Suzuki, A. Takeuchi, K. Uesugi, Observation of Water Droplets in Microporous Layers for Polymer Electrolyte Fuel Cells by X-Ray Computed Nano-Tomography, J. Synchrotron Rad. 29 (2022) 1258–1264.
15. K. Uesugi, M. Hoshino, A. Takeuchi, Y. Suzuki, N. Yagi, T. Nakano, Development of Fast (Sub-Minute) Micro-Tomography, AIP Conf. Proc. 1266 (2010) 47–50.
16. Schneider, C. A.; Rasband, W. S.; Eliceiri, K. W. NIH Image to ImageJ: 25 Years of Image Analysis, Nat. Methods 9 (2012) 671–675.
17. GeoDict-The Digital Material Laboratory. https://www.geodict.com/ (accessed 2023-10-25).

Chapter 9

Summary and Perspective

The transition from internal combustion engine vehicles to electric vehicles is proceeding rapidly toward the realization of a carbon-neutral society. This thesis handled the structure and related transport phenomena within the polymer electrolyte fuel cells (PEFCs). The author used quantum beam analysis (small-angle neutron scattering, neutron reflectometry, and X-ray computed tomography) to investigate the multiscale structures of fuel cell components. In Part 1 (Chapters 2–5), the ionomer adsorption behavior onto the platinum and carbon surfaces was investigated using small-angle neutron scattering and neutron reflectometry. In Part 2 (Chapters 6–8), the pore morphologies of porous media in PEFCs was investigated using X-ray computed tomography (CT). The details of the respective Parts are summarized below:

In Chapters 2–4 of Part 1, the adsorption behavior of ionomers on platinum and carbon surfaces in catalyst inks was studied using small-angle neutron scattering. It is well known that the catalyst layer fabricated by coating the catalyst ink has segregated ionomers and some of dense ionomer layer on the platinum surface. The adsorption layer limits oxygen transport to the platinum surface, resulting in lower PEFC performance. Small-angle neutron scattering experiments revealed that the ionomer adsorption layer is formed at the stage of catalyst inks. The author reported that the ionomer adsorption behavior in catalyst inks depends on the platinum loading (Chapter 2), ionomer content (Chapter 3), and temperature (Chapter 4). The author discussed the ionomer adsorption mechanism in the catalyst ink from the viewpoint of the interaction between ionomers and platinum supported on carbon particles. In Chapter 5 of Part 1, the ionomer adsorption behavior of ionomer thin films prepared on carbon surfaces with different surface properties was investigated by neutron reflectometry. Carbon thin films used as model samples for the catalyst layer were deposited on silicon substrates. Carbon samples with different surface properties were used: one immediately after sputter deposition, one after HNO_3 treatment for hydrophilization, and one after NH_3 treatment. Neutron reflectivity experiments revealed that a highly dense and thick ionomer layer was formed on the carbon surface after HNO_3 treatment, indicating the possibility of surface modification of carbon materials as a method to suppress ionomer adsorption on the platinum surface.

In Part 2, the pore structure in the gas diffusion layer was investigated using X-ray computed tomography (CT). The gas diffusion layer consists of a substrate (carbon fiber layer) and a microporous layer with nanoscale pores (carbon black layer). The complex pore morphologies within the gas diffusion layer limits the oxygen transport properties. In Chapter 6, the pore structure of the compressed gas diffusion layer was evaluated by X-ray micro-CT to clarify the correlation between the gas diffusivity predicted from the pore structure and that evaluated from the fuel cell evaluation. In Chapter

7, the author studied the gas diffusivity of the wet gas diffusion layer. The results showed that the gas diffusivity differs in the presence of liquid water produced by condensation and that produced by power generation. In Chapter 8, a new powder deposition process was proposed as a method to control the pore morphologies within microporous layers. In this thesis, the author showcased a multilayer microporous layer with a gradient pore size in the stacking direction to enhance the ability of capillary force to drain liquid water from the PEFC. The gradient pore morphologies of the powder-deposited microporous layer was revealed by X-ray nano-CT. The fuel cell performance evaluation demonstrated that the microporous layers with a pore gradient had the effect of liquid water drainage driven by capillary forces.

In conclusion, this thesis presents the structural evaluation of PEFC components by quantum beam analysis and its correlation with mass (oxygen and water) transport properties. The author believes that the obtained knowledge contributes to the guideline for the material development of PEFCs focusing on the mass transport properties. It is worth noting that the produced water and heat may have a significant impact on the oxygen transport properties under harsh conditions. The limitation of this study is that some of the effects has been neglected. To address these issues, it is necessary to establish *operando* measurement techniques. In addition, the structural analysis presented in this thesis can be applied to other electrochemical devices such as water electrolyzers and carbon dioxide electrolyzers. At present, there is an urgent need to improve their electrochemical efficiency. However, electrochemical activity alone is not enough to build a practical system as well as PEFCs. We need to consider how to maximize the mass transport properties with structural analysis using quantum beam analysis techniques. The field of electrochemistry, including fuel cells and other electrochemical devices, will contribute to the realization of a carbon-neutral society. The authors conclude this thesis with the expectation that the use of quantum beam analysis in the field of electrochemistry will continue to expand further in the future.

Appendix

List of Publications

01. Wataru Yoshimune*, Masashi Harada, Effect of Pt Loading on the Adsorption of Perfluoro-Sulfonic Acid Ionomer in Catalyst Ink for Polymer Electrolyte Fuel Cells, Chem. Lett. 48 (2019) 487–490. Editor's Choice

    Part 1: Chapter 2

02. Wataru Yoshimune*, Masashi Harada, Impact of Nonadsorbed Ionomer on Viscosity of Catalyst Inks for Polymer Electrolyte Fuel Cells, Bull. Chem. Soc. Jpn. 93 (2020) 302–307. Editor's Choice

    Part 1: Chapter 3

03. Wataru Yoshimune*, Masashi Harada, Temperature-Induced Shear-Thinning Catalyst Inks, Electrochem. Commun. 130 (2021) 107099.

    Part 1: Chapter 4

04. Wataru Yoshimune*, Nobuaki Kikkawa*, Hiroaki Yoneyama, Naoko Takahashi, Saori Minami, Yusuke Akimoto, Takuya Mitsuoka, Hiroyuki Kawaura, Masashi Harada, Norifumi L. Yamada, Hiroyuki Aoki, Interfacial Distribution of Nafion Ionomer Thin Films on Nitrogen-Modified Carbon Surfaces, ACS Appl. Mater. Interfaces 14 (2022) 53744–53754.

    Part 1: Chapter 5

05. Wataru Yoshimune*, Satoru Kato*, Satoshi Yamaguchi, Multi-Scale Pore Morphologies of a Compressed Gas Diffusion Layer for Polymer Electrolyte Fuel Cells, Int. J. Heat Mass Transfer 152 (2020) 119537.

    Part 2: Chapter 6

06. Wataru Yoshimune*, Satoshi Yamaguchi, Satoru Kato, Insights into Oxygen Transport Properties of Partially Wet Gas Diffusion Layers for Polymer Electrolyte Fuel Cells, Energy Fuels 37 (2023) 7424–7432.

    Part 2: Chapter 7

07. Wataru Yoshimune*, Satoru Kato, Satoshi Yamaguchi, Yusuke Akimoto, Akihiko Koiwai, Hiroshi Nakamura, Managing the Pore Morphologies of Micro-Porous Layers for Polymer Electrolyte Fuel Cells, ACS Sustain. Chem. Eng. 9 (2021) 7922–7929.

    Part 2: Chapter 8

Other Publications

01. Hongcheng Lu, Takafumi Yamamoto, Wataru Yoshimune, Naoaki Hayashi, Yoji Kobayashi, Yoshitami Ajiro, Hiroshi Kageyama*, A Nearly Ideal One-Dimensional S=5/2 Antiferromagnet FeF_3(4,4'–bpy)(4,4'–bpy=4,4'–bipyridyl) with Strong Intrachain Interactions, J. Am. Chem. Soc. 137 (2015) 9804–9807.
02. Guillaume Bouilly, Takeshi Yajima, Takahito Terashima, Wataru Yoshimune, Kousuke Nakano, Cédric Tassel, Yoshiro Kususe, Koji Fujita, Katsuhisa Tanaka, Takafumi Yamamoto, Yoji Kobayashi, Hiroshi Kageyama*, Electrical Properties of Epitaxial Thin Films of Oxyhydrides $ATiO_{3-x}H_x$ (A = Ba and Sr), Chem. Mater. 27 (2015) 6354–6359.
03. Takeshi Yajima, Fumitaka Takeiri, Kohei Aidzu, Hirofumi Akamatsu, Koji Fujita, Wataru Yoshimune, Masatoshi Ohkura, Shiming Lei, Venkatraman Gopalan, Katsuhisa Tanaka, Craig M. Brown, Mark A. Green, Takafumi Yamamoto, Yoji Kobayashi, Hiroshi Kageyama*, A Labile Hydride Strategy for the Synthesis of Heavily Nitridized $BaTiO_3$, Nat. Chem. 7 (2015) 1017–1023.
04. Riho Mikita, Tomoko Aharen, Takafumi Yamamoto, Fumitaka Takeiri, Tang Ya, Wataru Yoshimune, Koji Fujita, Suguru Yoshida, Katsuhisa Tanaka, Dmitry Batuk, Artem M. Abakumov, Craig M. Brown, Yoji Kobayashi, Hiroshi Kageyama*, Topochemical Nitridation with Anion Vacancy-Assisted N^{3-}/O^{2-} Exchange, J. Am. Chem. Soc. 138 (2016) 3211–3217.
05. Hiroshi Takatsu, Olivier Hernandez, Wataru Yoshimune, Carmelo Prestipino, Takafumi Yamamoto, Cédric Tassel, Yoji Kobayashi, Dmitry Batuk, Yuki Shibata, Artem M. Abakumov, Craig M. Brown, Hiroshi Kageyama*, Cubic Lead Perovskite $PbMoO_3$ with Anomalous Metallic Behavior, Phys. Rev. B 95 (2017) 155105.
06. Satoru Kato*, Satoshi Yamaguchi, Wataru Yoshimune, Yoriko Matsuoka, Akihiko Kato, Yasutaka Nagai, Takahisa Suzuki, Ex-Situ Visualization of the Wet Domain in the Microporous Layer in a Polymer Electrolyte Fuel Cell by X-Ray Computed Tomography under Water Vapor Supply, Electrochem. Commun. 111 (2020) 106644.
07. Morito Namba, Hiroshi Takatsu*, Wataru Yoshimune, Aurélien Daniel, Shoichi Itoh, Takahito Terashima, Hiroshi Kageyama*, A Partial Anion Disorder in $SrVO_2H$ Induced by Biaxial Tensile Strain, Inorganics 26 (2020) 8. 2020 Best Paper Award
08. Cédric Tassel, Wataru Yoshimune, Masaichiro Mizumaki, Yoji Kobayashi, Hiroshi Kageyama*, Co–$L_{2,3}$ Edge Soft X-Ray Absorption Spectroscopy of Topochemically Oxidized $CaCoO_3$ Thin Films, SPring-8 Research Report 8 (2020) 242–246.
09. Wataru Yoshimune*, Masashi Harada, Yusuke Akimoto, Small-Angle Neutron Scattering Studies on the Distribution of Polytetrafluoroethylene within Microporous Layers for Polymer Electrolyte Fuel Cells, Compos. C: Open Access 2 (2020) 100015.
10. Wataru Yoshimune*, Masashi Harada, Nanostructure of a Catalyst Ink Investigated by Contrast-Variation Small-Angle Neutron Scattering, ECS Trans. 98 (2020) 447. Conference Paper
11. Yoriko Matsuoka*, Satoru Kato, Wataru Yoshimune, Observation and Structural Analysis of the

Microporous Layer in Polymer Electrolyte Fuel Cells Using Electron Staining", Kagaku Kougaku Ronbunshu 47 (2021) 76–84. Written in Japanese

12. Wataru Yoshimune*, Akira Kuwaki*, Takumi Kusano, Takuro Matsunaga, Hiroshi Nakamura, In Situ Small-Angle X-ray Scattering Studies on the Growth Mechanism of Anisotropic Platinum Nanoparticles, ACS Omega 6 (2021) 10866–10874.
13. Takumi Kusano*, Naomi Kumano, Wataru Yoshimune, Toshihisa Munekata, Takuro Matsunaga, Masashi Harada*, Interplay between Interparticle Potential and Adsorption Structure in Nanoparticle Dispersions with Polymer Addition as Displayed by Small-Angle Scattering, Langmuir 37 (2021) 7503–7512.
14. Wataru Yoshimune, Satoru Kato, Harada Masashi*, In Situ Small-Angle Neutron Scattering Investigation of Water Evaporation in the Porous Supports for Exhaust Gas Catalysts, ACS Appl. Mater. Interfaces 14 (2022) 179396–179404.
15. Wataru Yoshimune*, Satoru Kato, Masahide Inagaki, Satoshi Yamaguchi, A Simple Method to Measure Through-Plane Effective Gas Diffusivity of a Gas Diffusion Layer for Polymer Electrolyte Fuel Cells, Int. J. Heat Mass Transfer 191 (2022) 122887.
16. Satoshi Yamaguchi*, Satoru Kato, Wataru Yoshimune, Daigo Setoyama, Akihiko Kato, Yasutaka Nagai, Takahisa Suzuki, Akihisa Takeuchi, Kentaro Uesugi, Observation of Water Droplets in Microporous Layers for Polymer Electrolyte Fuel Cells by X-Ray Computed Nano-Tomography, J. Synchrotron Radiat. 29 (2022) 1258–1264.
17. Wataru Yoshimune*, Dependence of Oxygen Transport Properties of Catalyst Layers for Polymer Electrolyte Fuel Cells on the Fabrication Process, Results Chem. 5 (2023) 100738.
18. Masahide Inagaki*, Wataru Yoshimune, Satoru Kato, Computer-Aided Determination of the Effective Diffusion Coefficient of a Gas Diffusion Layer for Polymer Electrolyte Fuel Cells, Chem. Eng. J. Adv. 14 (2023) 100479.
19. Wataru Yoshimune*, Yuki Higuchi, Akihiko Kato, Shogo Hibi, Satoshi Yamaguchi, Yoshihiro Matsumoto, Hirotoshi Hayashida, Hiroshi Nozaki, Takenao Shinohara, Satoru Kato, 3D Water Management in Polymer Electrolyte Fuel Cells toward Fuel Cell Electric Vehicles, ACS Energy Lett. 8 (2023) 3485–3487.
20. Wataru Yoshimune, Juliana B. Falqueto, Adam H. Clark, Nur Sena Yüzbasi, Thomas Graule, Dominika Baster, Mario El Kazzi, Thomas J. Schmidt, Emiliana Fabbri*, The Role of Phosphate Functionalization on the Oxygen Evolution Reaction Activity of Cobalt-Based Oxides at Different pH Values, Small Structures 8 (2023) 2300106.

List of Presentations

International (Oral)

01. ○Wataru Yoshimune, Takeshi Yajima, Fumitaka Takeiri, Kohei Aidzu, Masatoshi Ohkura, Craig M. Brown, Mark A. Green, Takafumi Yamamoto, Yoji Kobayashi, Hiroshi Kageyama, Low Temperature Synthesis of Titanium Perovskite Oxynitride, The 53th Symposium on Basic Science of Ceramics, Kyoto, Japan, January 9, 2015.

02. ○Taito Murakami, Takafumi Yamamoto, Wataru Yoshimune, Kousuke Nakano, Hiroshi Kageyama, Searching for New Bismuthide Superconductors, The 53th Symposium on Basic Science of Ceramics, Kyoto, Japan, January 9, 2015.

03. ○Fumitaka Takeiri, Takeshi Yajima, Kohei Aidzu, Hirofumi Akamatsu, Koji Fujita, Wataru Yoshimune, Venkatraman Gopalan, Katsuhisa Tanaka, A Labile Hydride Strategy for the Synthesis of Novel Oxynitrides, The 96th CSJ Annual Meeting, Kyoto, Japan, March 25, 2016.

04. ○Satoru Kato, Satoshi Yamaguchi, Wataru Yoshimune, Yoriko Matsuoka, Yasutaka Nagai, Akihiko Kato, Takahisa Suzuki, Visualizing of Liquid Water in Micro Porous Layer Formed by Water Vaper Diffusion into Gas Diffusion Layer for PEFC Using X-Ray Computed Tomography, 18th Asian Pacific Confederation of Chemical Engineering Congress, September 25, 2019.

05. ○Satoru Kato, Satoshi Yamaguchi, Wataru Yoshimune, Yoriko Matsuoka, Yasutaka Nagai, Akihiko Kato, Takahisa Suzuki, Visualizing 3D Distribution of Wet Domain in Microporous Layer in Polymer Electrolyte Fuel Cell by X-Ray Computed Tomography Under Water Vapor Supply, InterPore2020, Online, September 3, 2020.

06. ○Wataru Yoshimune, My Research Activities at Toyota Central R&D Labs., Inc., LEC Seminar, PSI, Switzerland, February 16, 2022. Invited Lecture

07. ○Satoru Kato, Yuki Higuchi, Akihiko Kato, Yoshihiro Matsumoto, Hirotoshi Hayashida, Wataru Yoshimune, Takahisa Suzuki, Shogo Hibi, Yoriko Matsuoka, Satoshi Yamaguchi, Daigo Setoyama, Kazuhisa Isegawa, Hiroshi Nozaki, Masashi Harada, Norihiro Fukaya, Takenao Shinohara, Yasutaka Nagai, Pulsed Neutron and Synchrotron X-Ray Imaging of Liquid Water Formation and Transport in Polymer Electrolyte Fuel Cells, 244th ECS Meeting, Gothenburg, Sweden, October 12, 2023.

International (Poster)

01. ○Fumitaka Takeiri, Takeshi Yajima, Kohei Aidzu, Hirofumi Akamatsu, Koji Fujita, Wataru Yoshimune, Masatoshi Okura, Shiming Lei, Venkatraman Gopalan, Katsuhisa Tanaka, Craig M. Brown, Mark A. Green, Takafumi Yamamoto, Yoji Kobayashi, Hiroshi Kageyama, "A Labile Hydride Strategy to Synthesize Oxynitrides" E-MRS, Advances and Enhanced Functionalities of Anion-controlled New Inorganic Materials, Lille, France, May 11, 2015.

02. ○Riho Mikita, Fumitaka Takeiri, Tomoko Aharen, Takafumi Yamamoto, Wataru Yoshimune, Hiroshi Kageyama, Europium Titanium Oxynitride, E-MRS, Advances and Enhanced Functionalities of Anion-controlled New Inorganic Materials, Lille, France, May 11, 2015.

03. ○Wataru Yoshimune, Masashi Harada, Effect of Pt Loading on the Adsorption of Perfluoro-Sulfonic Acid Ionomer in Catalyst Ink for Polymer Electrolyte Fuel Cells, OKINAWA COLLOIDS 2019, Okinawa, Japan, November 6, 2019.

04. ○Wataru Yoshimune, Masashi Harada, Impact of Nonadsorbed Ionomer on Viscosity of Catalyst Inks for Polymer Electrolyte Fuel Cells, Grand Views of Soft and Liquid Matter Physics, Tokyo, Japan, March 10, 2020.

05. ○Wataru Yoshimune, Masashi Harada, Nanostructure of a Catalyst Ink Investigated by Contrast-Variation Small-Angle Neutron Scattering, PRiME2020, Online, October 4, 2020.

06. ○Yuki Higuchi, Wataru Yoshimune, Satoru Kato, Shogo Hibi, Daigo Setoyama, Kazuhisa Isegawa, Yoshihiro Matsumoto, Hirotoshi Hayashida, Hiroshi Nozaki, Masashi Harada, Norihiro Fukaya, Takahisa Suzuki, Takenao Shinohara, Yasutaka Nagai, Visualizing the freezing behavior of water in an automotive polymer electrolyte fuel cell in operation by using neutron imaging, 11th Workshop on Neutron Wavelength Dependent Imaging, Tokyo, Japan, October 24, 2023.

Domestic (Oral)

01. 野崎 保将, 矢島 健, 吉宗 航, 後藤 能宏, Cédric Tassel, 山本 隆文, 小林 洋治, 陰山 洋, 新規層状ニクタイド水素化物の合成, 日本セラミックス協会 第 27 回秋季シンポジウム, 鹿児島大学, 2014 年 9 月 8 日.

02. ○吉宗 航, Cédric Tassel, Guillaume Bouilly, 寺嶋 孝仁, 山本 隆文, 小林 洋治, 陰山 洋, トポケミカル酸化反応による新規ペロブスカイト薄膜の合成, 日本セラミックス協会第 27 回秋季シンポジウム, 鹿児島大学, 2014 年 9 月 8 日.

03. ○村上 泰斗, 山本 隆文, 吉宗 航, 中野 晃佑, 陰山 洋, ビスマス化物新規超伝導物質の探索, 日本セラミックス協会第 27 回秋季シンポジウム, 鹿児島大学, 2014 年 9 月 8 日.

04. ○竹入 史隆, 矢島 健, 吉宗 航, 山本 隆文, 小林 洋治, 陰山 洋, ヒドリドを活用した新規酸窒化物合成, 第 13 回低温物質科学研究センター講演会・研究交流会, 京都大学, 2015 年 2 月 10 日.

05. ○竹入 史隆, 會津 康平, 吉宗 航, 山本 隆文, 小林 洋治, 陰山 洋, 矢島 健, 新規チタン酸窒化物(1): $BaTiO_{3-x}N_{2x/3}$ の合成, 日本セラミックス協会 2015 年年会, 岡山大学, 2015 年 3 月 19 日.

06. ○竹入 史隆, 會津 康平, 吉宗 航, 藤田 晃司, 田中 勝久, 山本 隆文, 小林 洋治, 陰山 洋, 矢島 健, 赤松 寛文, Lei Shiming, Venkatraman Gopalan, 新規チタン酸窒化物(2): $BaTiO_{3-x}N_{2x/3}$ の物性, 日本セラミックス協会 2015 年年会, 岡山大学, 2015 年 3 月 19 日.

07. ○三木田 梨歩, 阿波連 知子, 山本 隆文, 竹入 史隆, 吉宗 航, 藤田 晃司, 田中 勝久, 陰山 洋, 高温トポケミカル反応による新規酸窒化物の合成, 日本セラミックス協会第 28 回秋季シンポジウム, 富山大学, 2015 年 9 月 18 日.

08. ○三木田 梨歩, 阿波連 知子, 山本 隆文, 竹入 史隆, 吉宗 航, 藤田 晃司, 吉田 傑, 田中 勝久, Dmitry Batuk, Artem M. Abakumov, Craig M. Brown, 小林 洋治, 陰山 洋, 高温トポケミカル反応による新規酸窒化物の合成, 日本化学会第 96 春季年会, 同志社大学, 2016 年 3 月 25 日.

09. ○高津 浩, 吉宗 航, 山本 隆文, Cédric Tassel, 小林 洋治, Olivier Hernandez, Dmitry Batuk, Artem M. Abakumov, Craig M. Brown, 陰山 洋, 新規ペロブスカイト型酸化物 $PbMoO_3$ の低温物性, 日本物理学会 2016 年秋季大会, 金沢大学, 2016 年 9 月 13 日.

10. ○中山 亮, 前里 光彦, 吉宗 航, 山本 隆文, 陰山 洋, 寺嶋 孝仁, 北川 宏, In-situ 抵抗測定による $SrTiO_3$ への水素イオンビーム照射効果の研究, 第 15 回物性科学センター講演会・研究交流会, 京都大学, 2017 年 2 月 20 日.

11. ○中山 亮, 前里 光彦, 吉宗 航, 山本 隆文, 陰山 洋, 寺嶋 孝仁, 北川 宏, 水素イオンビーム照射によるチタン酸ストロンチウムの物性制御, 第 97 回日本化学会春季年会, 慶応大学, 2017 年 3 月 17 日.

12. ○高津 浩, Daniel Aurelien, 三木田 梨歩, 吉宗 航, 寺嶋 孝仁, 陰山 洋, La ドープした $SrVO_2H$ 薄膜の合成と低温物性, 2018 年度日本物理学会秋季大会, 信州大学, 2018 年 9 月 9 日.

13. ○原田 雅史, 吉宗 航, 工藤 憲治, 山田 悟史, 固体高分子形燃料電池で活躍するアイオノマの中性子利用構造解析, 第 169 回東海高分子研究会講演会, 三重, 2019 年 8 月 31 日.

14. ○山口 聡, 加藤 悟, 吉宗 航, 加藤 晃彦, 長井 康貴, 鈴木 孝尚, 固体高分子形燃料電池ガス拡散層の撥水層における液水の観察, 第 17 回産業利用報告会, オンライン, 2020 年 9 月 3 日.

15. ○吉宗 航, 加藤 悟, 山口 聡, 固体高分子形燃料電池の多孔質部材の構造・輸送解析(4) 圧縮した状態におけるガス拡散層の細孔形態測定, 化学工学会第 51 回秋季大会, オンライン, 2020 年 9 月 25 日.

16. ○山口 聡, 加藤 悟, 吉宗 航, 加藤 晃彦, 長井 康貴, 鈴木 孝尚, 固体高分子形燃料電池の多孔質部材の構造・輸送解析(5) X 線ナノ CT による撥水性材料中の液水の可視化, 化学工学会第 51 回秋季大会, オンライン, 2020 年 9 月 25 日.

17. ○原田 雅史, 吉宗 航, 固体高分子形燃料電池の電極作製に用いる触媒インクの構造解析に対するコントラスト変調小角中性子散乱法の応用, MRM フォーラム 2020, オンライン, 2020 年 12 月 8 日.

18. ○吉宗 航, 中性子や X 線を利用した燃料電池触媒インクの液構造解析, 第 30 回東海ミニシンポジウム, オンライン, 2020 年 12 月 18 日. Invited

19. ○吉宗 航, 桑木 聴, 草野 巧巳, 松永 拓郎, 小角 X 線散乱を用いた白金ナノ粒子形成過程のその場観察, 第 9 回あいちシンクロトロン光センター事業成果発表会, オンライン, 2021 年 5 月 28 日.

20. ○加藤 悟, 山口 聡, 吉宗 航, 松岡 世里子, 鈴木 孝尚, 長井 康貴, 加藤 晃彦, 固体高分子形燃料電池の多孔質部材の構造・輸送解析技術, 化学工学会第 87 年会, オンライン, 2022 年 3 月 18 日.

21. ○吉宗 航, 原田 雅史, 固体高分子形燃料電池における量子ビーム利用 –小角中性子散乱法を用いた触媒インクの液分散構造解析–, 第 71 回高分子討論会, 北海道大学, 2022 年 9 月 5 日.

22. ○吉宗 航, 加藤 悟, 稲垣 昌英, 山口 聡, 固体高分子形燃料電池の多孔質部材の構造･輸送解析(8) 光学式 CO_2 センサを用いた拡散性評価手法の提案, 化学工学会第 53 回秋季大会, 信州大学, 2022 年 9 月 14 日.

23. ○吉宗 航, 加藤 悟, 原田 雅史, 小角中性子散乱法を用いた多孔質材料の乾燥過程における水挙動解析, 化学工学会第 53 回秋季大会, 信州大学, 2022 年 9 月 14 日.

24. ○吉川 信明, 吉宗 航, 米山 弘亮, 南 沙央理, 実験･計算の両面から迫る窒素ドープ炭素担体上のアイオノマ界面構造, 第 63 回電池討論会, 九州大学, 2022 年 11 月 8 日.

25. ○吉宗 航, 加藤 悟, 山口 聡, 秋元 裕介, 小岩井 明彦, 中村 浩, 乾式塗工法を用いた固体高分子形燃料電池用マイクロポーラス層の作製, 2022 年度秋期研究発表会, 東京ビッグサイト, 2022 年 12 月 6 日.

26. ○加藤 悟, 山口 聡, 吉宗 航, 松岡 世里子, 鈴木 孝尚, 固体高分子形燃料電池のガス拡散層の構造・輸送解析技術, 化学工学会第 88 年会, 東京農工大学, 2023 年 3 月 16 日.

27. ○吉宗 航, 固体高分子形燃料電池多孔質部材の開発を加速する量子ビーム解析技術の構築, 東海化学工業会受賞記念特別講演会, 2023 年 5 月 25 日. Award Lecture

28. ○樋口 雄紀, 加藤 悟, 吉宗 航, 日比 章五, 瀬戸山 大吾, 伊勢川 和久, 野崎 洋, 原田 雅史, 鈴木 孝尚, 深谷 徳宏, 松本 吉弘, 林田 洋寿, 篠原 武尚, 長井 康貴, 中性子による車載用燃料電池内凍結挙動の可視化, 令和 5 年度 中性子イメージング研究会, エッサム神田ホール, 2023 年 8 月 31 日.

29. ○樋口 雄紀, 加藤 悟, 吉宗 航, 日比 章五, 瀬戸山 大吾, 伊勢川 和久, 野崎 洋, 原田 雅史, 鈴木 孝尚, 深谷 徳宏, 松本 吉弘, 林田 洋寿, 篠原 武尚, 長井 康貴, 固体高分子形燃料電池の operando 液水解析(3) 中性子による車載用燃料電池内凍結挙動の可視化, 化学工学会第 54 回秋季大会, 福岡大学, 2023 年 9 月 12 日.

30. ○吉宗 航, 樋口 雄紀, 加藤 晃彦, 日比 章五, 山口 聡, 野崎 洋, 加藤 悟, 松本 吉弘, 林田 洋寿, 篠原 武尚,固体高分子形燃料電池の operando 液水解析(4) 中性子と放射光を併用した燃料電池内部の液水可視化, 化学工学会第 54 回秋季大会, 福岡大学, 2023 年 9 月 12 日.

31. ○吉宗 航, 中性子を用いた排ガス浄化触媒材料の水蒸発過程解析, 第 13 回 CSJ 化学フェスタ 2023, タワーホール船堀, 2023 年 10 月 18 日. Invited

Domestic (Poster)

01. 竹入 史隆, 矢島 健, 會津 康平, 赤松 寛文, 藤田 晃司, 吉宗 航, Shiming Lei, Venkatraman Gopalan, 田中 勝久, 山本 隆文, 小林 洋治, 陰山 洋, 格子中ヒドリドの高活性を利用した新規酸窒化物 $BaTiO_{3-x}N_{2x/3}$ の合成とその物性, 第 5 回 CSJ 化学フェスタ, タワーホール船堀, 2015 年 10 月 15 日.

02. ○高津 浩, Daniel Aurelien, 三波 杜人, 三木田 梨歩, 吉宗 航, 寺嶋 孝仁, 陰山 洋, 秩序型アニオン構造を持った $SrVO_2H$ のキャリア制御と低温物性, 第 12 回物性科学領域横断研究会, 奈良先端大学, 2018 年 11 月 30 日.

03. ○吉宗 航, 原田 雅史, 固体高分子形燃料電池触媒インクにおけるアイオノマ吸着量の Pt 担持量依存性, 第 28 回ポリマー材料フォーラム, 名古屋, 2019 年 11 月 22 日.

04. ○吉宗 航, 放射光・中性子を利用した燃料電池多孔質構造解析技術の構築, 第 13 回新電極触媒シンポジウム, 静岡, 2022 年 11 月 25 日.

05. ○南 沙央理, 吉川 信明, 吉宗 航, 米山 弘亮, 実験･計算の両面から迫る窒素ドープ炭素担体上のアイオノマ界面構造, 第 36 回分子シミュレーション討論会, 東京工業大学, 2022 年 12 月 6 日.

06. ○樋口 雄紀, 加藤 悟, 吉宗 航, 日比 章五, 瀬戸山 大吾, 伊勢川 和久, 野崎 洋, 原田 雅史, 鈴木 孝尚, 深谷 徳宏, 松本 吉弘, 林田 洋寿, 篠原 武尚, 長井 康貴, 中性子による車載用燃料電池内凍結挙動の可視化, 令和 5 年度 中性子産業利用報告会, 秋葉原コンベンションホール, 2023 年 7 月 14 日.

07. ○吉宗 航, 樋口 雄紀, 加藤 晃彦, 日比 章五, 山口 聡, 野崎 洋, 加藤 悟, 松本 吉弘, 林田 洋寿, 篠原 武尚, 中性子と放射光を併用した燃料電池内部の液水可視化, 第 20 回 SPring-8 産業利用報告会, 神戸国際会議場, 2023 年 9 月 8 日.

List of Patents

01. 陰山 洋, 小林 洋治, 會津 康平, 吉宗 航, 細野 秀雄, ペロブスカイト型金属酸窒化物の製造方法, 特許第 6509194 号.

02. Hiroshi Kageyama, Yoji Kobayashi, Aidzu Kohei, Wataru Yoshimune, Hideo Hosono, Method for Producing Perovskite Metal Oxynitride, US 9, 776, 866 B2.

03. 吉宗 航, 工藤 憲治, 小岩井 明彦, 燃料電池用ガス拡散層及びその製造方法, 特許第 6958347 号.

04. 工藤 憲治, 後藤 尚美, 吉宗 航, 長谷川 直樹, 神谷 厚志, 竹平 祐一, 岡 憲俊, アイオノマコート触媒及びその製造方法、並びに触媒インク, 特許第 7128634 号.

05. 吉宗 航, 石井 昌彦, マイクロポーラス層用ペースト及びその製造方法, 特許第 7207025 号.

06. 吉宗 航, 加藤 悟, 山口 聡, 自立型マイクロポーラス層, 特許第 7234902 号.

07. 吉宗 航, 加藤 悟, 山口 聡, ガス拡散層及びその製造方法, 特許第 7276369 号.

List of Awards

01. 加藤 悟, 山口 聡, 吉宗 航, 松岡 世里子, 鈴木 孝尚, 長井 康貴, 加藤 晃彦, 固体高分子形燃料電池の多孔質部材の構造・輸送解析技術, 2021 年度化学工学会反応工学部会 技術賞.

02. 加藤 悟, 山口 聡, 吉宗 航, 松岡 世里子, 鈴木 孝尚, 固体高分子形燃料電池のガス拡散層の構造・輸送解析技術, 2022 年度化学工学会 技術賞.

03. 吉宗 航, 固体高分子形燃料電池多孔質部材の開発を加速する量子ビーム解析技術の構築, 2023 年度東海化学工業会 技術賞.

Facilities and Proposal No.

Results presented in this thesis were obtained at 10mSANS of NIST (*n*Soft consortium), at BL17 of J-PARC (proposal no. 2019L0402), and at BL33XU of SPring-8 (proposal no. 2017A7032, 2017B7032, 2018A7032, 2018B7032, 2019A7032, 2019B7032, 2020A7032, 2021B7032, 2022A7032).

Acknowledgements

This thesis is based on the work carried out at Toyota Central R&D Labs., Inc. from 2016 to 2023. First of all, I would like to thank the company for providing me with the opportunity to summarize the work as a doctoral thesis.

I would like to express my sincere gratitude to **Professor Hiroyuki Aoki** for his support of the neutron reflectometry experiment and advice on the thesis.

I would also like to thank **Associate Professor Norifumi L. Yamada** for useful comments on the neutron reflectometry analysis.

I would like to thank all the co-researchers at Toyota Central R&D Labs., Inc., especially, **Dr. Satoru Kato**, **Dr. Masashi Harada**, **Dr. Satoshi Yamaguchi**, **Dr. Hiroshi Nakamura**, **Dr. Nobuaki Kikkawa**, **Mr. Hiroaki Yoneyama**, **Dr. Naoko Takahashi**, **Dr. Saori Minami**, **Mr. Yusuke Akimoto**, **Dr. Akihiko Koiwai**, **Dr. Hiroyuki Kawaura**, and **Mr. Takuya Mitsuoka** for their technical support.

Last but not least, I am deeply grateful to my lovely dog **Minto** and my wife **Ayano Nakamura** for threir continuous support, encouragement, and understanding.

October 2023

Wataru Yoshimune